THERMAL COOLING OF HOT SURFACES WITH FIN HEAT SINK, VAPOUR CHAMBER AND THERMOELECTRIC

TAN CHOON FOONG

MASTER OF ENGINEERING SCIENCE

FACULTY OF ENGINEERING AND GREEN TECHNOLOGY
UNIVERSITI TUNKU ABDUL RAHMAN
JULY 2016

THERMAL COOLING OF HOT SURFACES WITH FIN HEAT SINK, VAPOUR CHAMBER AND THERMOELECTRIC

By

TAN CHOON FOONG

A dissertation submitted to the Department of Industrial Engineering,
Faculty of Engineering and Green Technology,
Universiti Tunku Abdul Rahman,
In partial fulfilment of the requirements for the degree of
Master of Engineering Science
July 2016

THERMAL COOLING OF HOT SURFACES WITH FIN HEAT SINK, VAPOUR CHAMBER AND THERMOELECTRIC

ABSTRACT

This study investigated the performance of fin heat sink, vapour chamber and thermoelectric for the thermal management of semiconductors. Here, thermal management involves cooling performance that depends upon device heat dissipating power and aspect ratio of heat source/heat sink area. The investigation first considered cooling with the traditional fin heat sink under natural and force air convection. It then moved on to cover the combined fin heat sink – vapour chamber assembly and finally to the fin heat sink – thermoelectric unit. High power LEDs and power electronics require a high degree of cooling with small heat sinks. In order to simulate the heat output of LEDs, an electrically heated flat plate heater is employed. The performance of conventional fin heat sinks depend upon air circulation rate which dictates the heat transfer dissipated to the ambient. This is determined by the convection heat transfer coefficient over the heat transfer surface. Heat transfer coefficients are determined under natural and forced convection air flows which are then utilized in the subsequent theoretical performance simulation. A vapour chamber is a flat heat pipe. Heat pipes are efficient heat transfer devices. They are capable of transporting large amounts of heat over considerable distances with only a small temperature difference between the heat source and the heat sink. They are small, silent and passive during operation. Hence they provide an ideal heat dissipating device for electronic packages. They also act as thermal heat spreaders to reduce the thermal heat spreading resistance associated with high power heat flux sources and especially where there is a large difference in the footprints between heat source and heat sink. They are also useful in cases where there are a large number of heat sources placed over

one large single heat sink. The performance of a vapour chamber is investigated in the study. Thermoelectric is a solid-state device. A temperature difference applied across the two junctions of a pair of dissimilar materials (thermocouple) would create a voltage across it. This is known as the Seebeck effect. The converse by Peltier is also true. A voltage applied across the terminals of a thermocouple would produce hot and cold junctions which could be employed to cool hot surfaces. The thermoelectric cooling effect is investigated in this study.

Experimental investigations involving three different methods of thermal cooling of hot surfaces are presented. They include cooling with a fin heat sink alone; a fin heat sink – vapour chamber assembly; and a fin heat sink – thermoelectric assembly. Theoretical simulations of the fin heat sink are made using a CFD program. Theoretical models are proposed for the vapour chamber and thermoelectric devices. Experimental and theoretical results are compared in the thesis. The comparisons obtained are very encouraging. Recommendations for future studies are also made.

PUBLICATIONS

Based on the work of this thesis, a conference paper has been presented while another has been accepted. A book chapter was also published. Details are shown below:

No	Category	Title	Publisher	Status
1	Conference	Thermal field simulation of multi package LED module	2015 International Symposium on Next Generation Electronics (ISNE)	Presented
2	Conference	Thermal management of LED with vapor chamber and thermoelectric cooling	International Electronics Manufacturing Technology (IEMT2016)	Presented
3	Book chapter	Thermal field study of multichip LED module	The River Publishers	Published
4	Journal paper	Heat spreading and heat transfer coefficient with fin heat sink	Applied Thermal Engineering (ISSN: 1359-4311; CODEN: ATE NFT)	Published

5	Journal paper	Methodological considerations of using thermoelectrics with fin heat sink for cooling applications	Applied Sciences (ISSN 2076-3417; CODEN: ASPCC7)	Published

ACKNOWLEDGEMENTS

I would like to thank everyone who had contributed to the successful completion of this project. I would like to express my gratitude to my research supervisor, Prof. Ir. Dr. Ong Kok Seng for his invaluable advice, guidance and his enormous patience throughout the development of the research. His passion shows the interest in this research has motivated me to complete this project.

I am highly indebted and thoroughly grateful to Dr. Lai Koon Chun and Assoc. Prof. Dr. Tan Kia Hock for their generous guidance, encouragement and support throughout the research. I would also like to thank the laboratory assistants, Mr Thong Marn Foo, En. Mohd Syahrul Husni Bin Hassan and En. Khairul Hafiz Bin Mohamad for assisting me in this project.

In addition, I would also like to thank CREST and Osram Opto semiconductor Sdn. Bhd. for supporting and sponsoring in this research.

APPROVAL SHEET

I certify that this project report entitled **"THERMAL COOLING OF HOT SURFACES WITH FIN HEAT SINK, VAPOUR CHAMBER AND THERMOELECTRIC"** prepared by **TAN CHOON FOONG** has met the required standard for submission in partial fulfilment of the requirements for the award of Master of Engineering Science at Universiti Tunku Abdul Rahman.

Approved by,

____

(Prof. Dr. Ir. Ong Kok Seng)
Date:…………………..
Supervisor
Department of Industrial Engineering
Faculty of Engineering and Green Technology
Universiti Tunku Abdul Rahman

____

(Dr. Lai Koon Chun)
Date: ___________________
Co-supervisor
Department of PetroChemical Engineering
Faculty of Engineering and Green Technology
Universiti Tunku Abdul Rahman

FACULTY OF ENGINEERING AND GREEN TECHNOLOGY
UNIVERSITI TUNKU ABDUL RAHMAN

Date:

SUBMISSION OF THESIS

It is hereby certified that **TAN CHOON FOONG** (ID No: **14AGM06222**) has completed this thesis entitled "THERMAL COOLING OF HOT SURFACES WITH FIN HEAT SINK, VAPOUR CHAMBER AND THERMOELETRIC." under the supervision of Prof. Dr. Ir. Ong Kok Seng (Supervisor) from the Department of Industrial Engineering, Faculty of Engineering and Green Technology, and Dr. Lai Koon Chun (Co-Supervisor) from the Department of PetroChemical Engineering, Faculty of Engineering and Green Technology.

I understand that the University will upload softcopy of my thesis in pdf format into UTAR Institutional Repository, which may be made accessible to UTAR community and public

Yours Truly

____

(Tan Choon Foong)

DECLARATION

I, Tan Choon Foong, hereby declare that the thesis/dissertation is based on my original work except for quotations and citations which have been duly acknowledged. I also declare that it has not been previously or concurrently submitted for any other degree at UTAR or other institutions.

____

(Tan Choon Foong)

Date: ____________________

TABLE OF CONTENTS

LIST OF TABLES

LIST OF FIGURES

LIST OF SYMBOLS / ABBREVIATIONS

α_{te}	Seebeck coefficient of thermoelectric module (V/K)
ε	Aspect ratio (dimensionless)
η_o	Overall surface fin efficiency (dimensionless)
ΣR_{f2D}	Total two-dimensional thermal resistance of FHS (K/W)
ΣR_{fvc}	Total thermal resistance of FHS-VC assembly (K/W)
ΔA_{tim}	Area of contact surface between two surfaces (mm^2)
ΔT_{te}	Temperature difference across thermoelectric module (°C)
Δx_{tim}	Thickness of thermal interface material (= 0.1 mm)
Δx_{vc}	Wall thickness of vapour chamber (= 0.8 mm)
Δx_{wick}	Wick structure of vapour chamber (= 0.4 mm)
$\dot{q}_c$	Heat transfer rate at cold side of thermoelectric module (W)
$\dot{q}_h$	Heat transfer rate at hot side of thermoelectric module (W)
A_{fin}	Surface area of each fin (mm^2)
$A_{fin,b}$	Surface area of non-finned portion of FHS (mm^2)
A_t	Total heat transfer surface area of fin heat sink (mm^2)
A_{vc}	Surface area of vapour chamber (mm^2)
COP_c	Coefficient of cooling performance (dimensionless)
h_a	Heat transfer coefficient of air cooling (W/m^2 K)
h_{evap}	Evaporator heat transfer coefficient (W/m^2 K)
h_{cond}	Condensing heat transfer coefficient (W/m^2 K)

I_{EH} Current across heating element (A)

I_{te} Current across thermoelectric module (A)

k_{FHS} Thermal conductivity of fin heat sink (W/m K)

k_{fin} Thermal conductivity of fin's material (W/m K)

k_{tim} Thermal conductivity of thermal interface material (= 1.22W/m K)

k_{wall} Thermal conductivity of vapour chamber wall (= 385 W/m K)

K_{te} Thermal conductance of thermoelectric module (W/K)

L_{fin} Fin length (mm)

$L_{fin,c}$ Corrected fin length (mm)

N_{fin} Number of fin (dimensionless)

P_{EH} Power input into heating element (W)

P_{loss} Heat loss to the sides of system (W)

P_{te} Power supplied to thermoelectric module (W)

R_{al} Thermal resistance of aluminium block (K/W)

R_{base} Base wall thickness resistance of fin heat sink (K/W)

R_{cr} Thermal contact resistance (K/W)

R_{cond} Thermal resistance of vapour chamber at condenser (K/W)

R_{evap} Thermal resistance of vapour chamber at evaporator (K/W)

R_{fin} Thermal resistance of surface of fin heat sink (K/W)

R_{f1D} One dimensional thermal resistance of fin heat sink (K/W)

R_{srf} Thermal heat spreading resistance of fin heat sink (K/W)

R_{srvc} Thermal heat spreading resistance of vapour chamber (K/W)

R_{tim} Thermal resistance of thermal interface material (K/W)

R_{te} Internal electrical resistance of thermoelectric module (Ω)

R_{vc} Thermal resistance of vapour chamber (K/W)

R_{wall}	Thermal resistance of wall of vapour chamber (K/W)
R_{wick}	Thermal resistance of wick of vapour chamber (K/W)
t_{fin}	Thickness of fin (mm)
T_a	Ambient temperature (°C)
T_{alm}	Mean surface temperature of aluminium block (°C)
T_c	Cold side temperature of thermoelectric module (°C)
T_{fm}	Mean surface temperature of base of fin heat sink (°C)
T_{fmax}	Maximum temperature of base of fin heat sink (°C)
T_h	Hot side temperature of thermoelectric module (°C)
$T_{h,theory}$	Theoretical hot side temperature of thermoelectric module (°C)
T_{ins}	Insulation temperature (°C)
T_{mte}	Mean operating temperature of thermoelectric module (°C)
T_s	Mean surface temperature of heat source (°C)
T_{vcmax}	Maximum temperature at bottom surface of vapour chamber (°C)
T_{vctop}	Mean top surface temperature of vapour chamber (°C)
T_{vcbot}	Mean bottom surface temperature of vapour chamber (°C)
V_{te}	Voltage supplied to thermoelectric module (V)
V_{EH}	Voltage supplied to heating element (V)
W_{fin}	Fin width (mm)

LIST OF APPENDICES

CHAPTER 1

INTRODUCTION

1.1 Thermal management of electronic devices

Thermal management of electronic devices play an important role in the power and electronic sectors. It controls and maintains the operating temperature during operation. Thermal management also acts to prevent temperatures exceeding design values for safe operation. Most electronic devices are low power and produce small amounts of heat. However, some devices such as power transistors, CPUs, power diodes and LEDs produce significant amounts of heat. For example, heat is produced within the LED device itself, due to the inefficiency of the semiconductor processes that generate light. A typical LED might produce 20% visible light and 80% heat from the electric power input.

Temperature control and maintenance of operating temperatures of electronic devices are of utmost importance in order to avoid catastrophic failure of the system. For instance, high temperature creates high mechanical stress in LED device. Stress will cause wire bonding loss connection between the die and lead frame. This will cause the LED to permanently breakdown. Electronic devices at high temperatures might cause degradation of system performance, loss of noise margin and reduction of device lifetime. Compact and more highly integrated devices with smaller feature sizes and higher current device are current electronic devices development trends. Therefore, thermal management plays a vital role to ensure proper performance and reliable operation.

Heat generated from the electronic device must be transferred out of the system. The three basic heat transfer processes of transferring heat away from a package or device involves conduction, convection and radiation. Conduction refers to the transfer of heat through a solid medium. In convection, heat is transferred from the surface of a solid to a surrounding gas or fluid. Thermal radiation is via electromagnetic radiation. There are several basic techniques for cooling. These include water or air cooled heat sinks under natural or force circulation, heat pipes and thermoelectric.

1.2 Fin heat sink, vapour chamber and thermoelectric

A heat sink is a passive heat exchanger that transfers heat generated by an electronic device to a cooling fluid. It is used to dissipate heat from a high temperature heat source to a low temperature medium such as air or water. Passive heat exchangers have a major advantage over active ones as there is no extra power needed to make it function. A heat sink can be provided with an external fan to increase the heat transfer area to increase its cooling performance. Heat sinks are commonly used to cool high power semiconductors such as power transistors and LED devices. For example, heat sinks with external fans are widely used to cool CPU and graphics processors.

A heat sink is designed to have large surface area in contact with the surrounding medium like air as shown in Figure 1.1. The performance of the heat sink depends on several factors like material of construction, whether provided with fins, fin design, surface treatment and air velocity. A heat sink provided with fins is called a fin heat sink (FHS). Heat transfer follows the basic Fourier's law of heat conduction, Newton's law of cooling and Stefan-Boltzmann law of thermal radiation. Fourier's law of heat conduction states that when there is a temperature gradient in a body, heat will be transferred from the higher temperature region to the lower temperature region. Convection occurs between a solid surface and a moving fluid when they are at different temperatures. Radiation refers to heat transfer through electromagnetic waves between different objects with finite temperature.

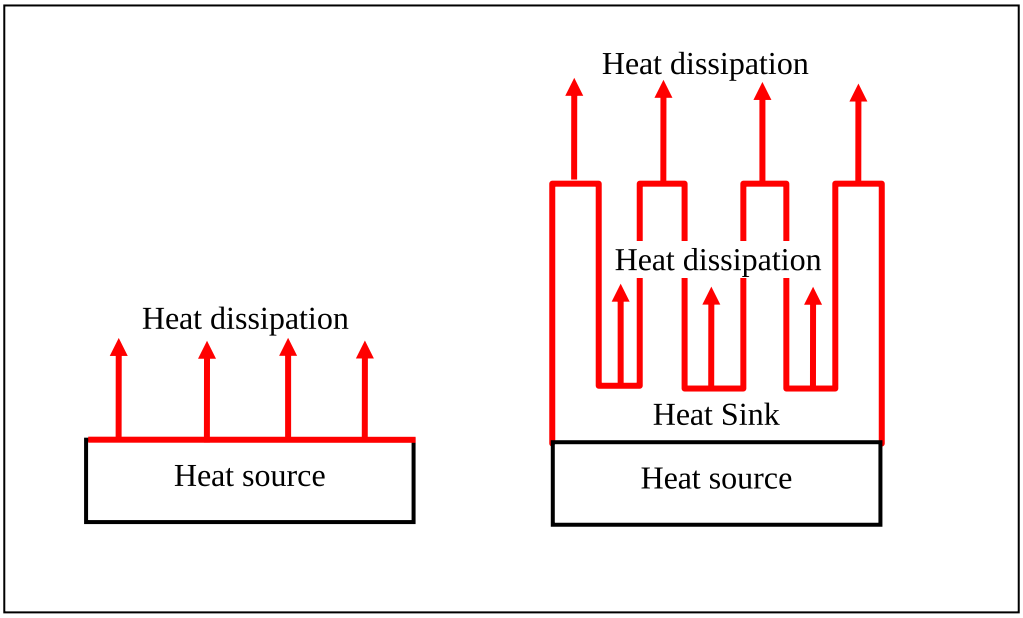

Figure 1.1 Heat transfer from a heat source with and without fin heat sink.

Heat sinks are classified into different categories based on various criteria. They are broadly classified as active or passive heat sinks. An active air-cooled heat sink consists of a FHS and a fan for air circulation. The performance of active heat sinks are better to natural convection ones but they require external power source for the air circulation. They would be more expensive as well. A passive heat sink does not possess any mechanical components. Normally, it consists of a base heat spreader and fin radiators. The fins are designed to dissipate heat via convection. There are various types of FHSs as illustrated in Figure 1.2.

- A plate fin heat sink is normally manufactured by machining process. Frequently, a gang saw is used for removing a block of material to make inter fins with precise spacing.
- A pin fin heat sink is a heat sink that has pins that extend from its base. The pins can be cylindrical, elliptical or square. Normally, it is manufactured by electric welding to combine the fins and the extruded base of heat sink.
- A flared fin heat sink has fins designed to be not parallel to each other. The purpose of the design is to reduce flow resistance and allow lower temperature air circulate in between the fin channels.
- A folded fin heat sink is fabricated from a large metal sheet. The sheet metal is folded into a serpentine fin array and attached to the base of the heat sink by soldering or brazing.

a) Plate fin heat sink

b) Pin fin heat sink

c) Flared fin heat sink

d) Folded fin heat sink

Figure 1.2 Four types of fin heat sinks (FHS).

A vapour chamber (VC) is also known as a flat plate heat pipe. It is a heat exchanger device that is derived from the heat pipe concept. Heat pipes and VCs are popular in the market due to their capability to transfer large quantities of heat, light weight, reliable and operate passively. A heat pipe (HP) is a heat transfer device that combines both the principles of thermal conductivity and phase transition. A heat pipe is made of a cylindrical metal pipe with a wick structure lining the internal wall. It is initially filled with a small quantity of working fluid and vacuumed. The pipe consists of three sections - evaporator, adiabatic and condenser section as shown in Figure 1.3. Heat transfer is via a phase-change phenomena. Heat supplied at the evaporator section evaporates the liquid in the liquid pool. The liquid vaporizes and travels to the condenser section at the top of the pipe. This process is a phase change phenomena and conveys a large amount of heat via latent heat of vaporization. At the condenser section, vapour condenses and rejects the latent heat of condensation to the cold ambient surrounding the condenser section. The condensed liquid is then transported back to evaporator section by gravity or by capillary action caused by wick structure. A VC works on a similar concept as a heat pipe. The major difference is the shape being flat and thin instead of cylindrical as shown in Figure 1.4.

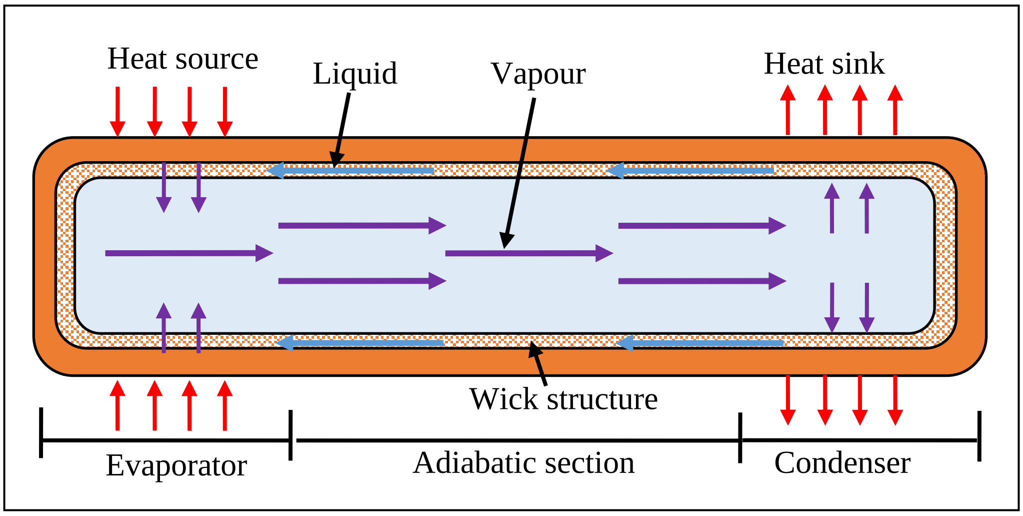

Figure 1.3 Cross sectional view of a heat pipe.

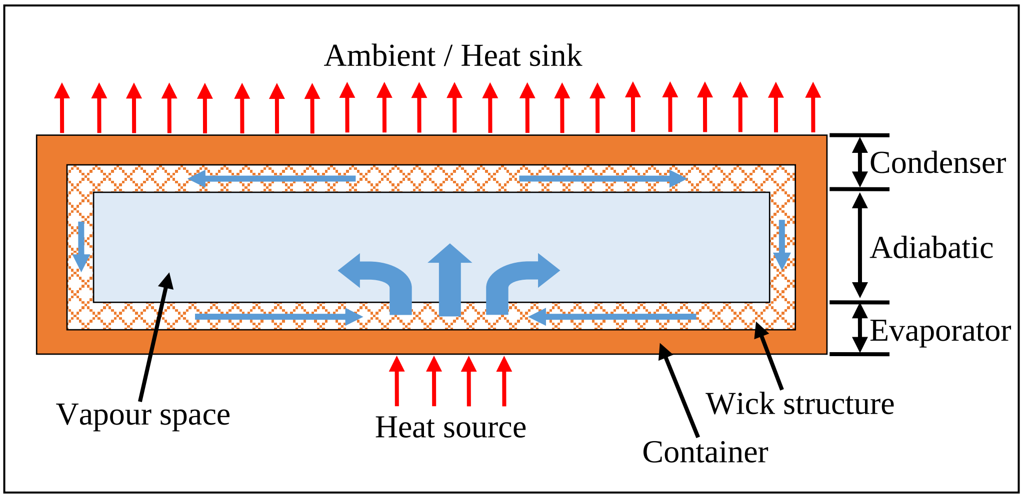

Figure 1.4 Cross sectional view of a vapour chamber.

Thermoelectric (TE) is a solid-state device that can perform thermal and electrical energy conversion. TE is recognized as an excellent cooling system due to its compactness and simple structure, no moving parts in the device, environmental friendly as no contain chlorofluorocarbon (CFC) compound, long life span capability at steady state operations and precisely temperature control. It is getting more and more popular and widely developed in thermal application such as thermal management on LED module and automotive industry. Cost of TE is relatively high and it operates with low efficiency. As a result, not much attention has been given to TE in the early days. However, as technology advances, cost of manufacturing has significantly reduced and performance improved. A TE module consists of many thermocouples connected electrically in series and thermally in parallel as shown in Figure 1.5. It is made of N-type and P-type semiconductor. Doped Bismuth Telluride is commonly used as the semiconductor pellets. The array of thermocouples is sandwiched by two thin layers of ceramic plate. Alumina (Al2O3) and Aluminium Nitride (AlN) are commonly used as the ceramic plate. TE exhibits Seebeck and Peltier effect. Seebeck effect was discovered by Thomas Seebeck. He stated that an electric potential can be generated when a temperature gradient is imposed across the junction of two dissimilar electrical conductors. This TE effect can be applied to generate voltage potential when one side of the ceramic plate is kept cold and the other side hot. Seebeck effect can be utilized for power generation. The Peltier effect is the reverse of Seebeck effect. A DC current flowing through a TE device creates a temperature difference across the ceramic surfaces, causing one side of the TE to be cold, while the other side is hot. This effect can be utilized as a heat pump for thermal cooling.

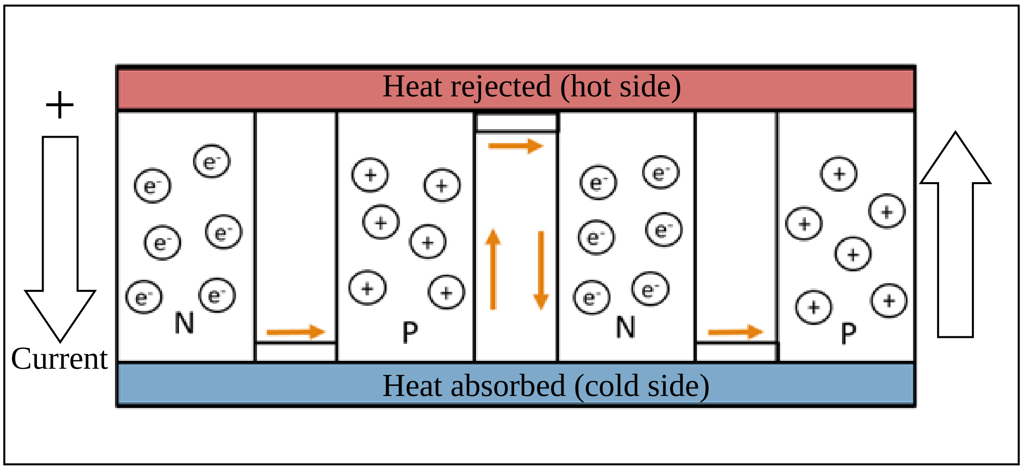

Figure 1.5 Internal structure of thermoelectric module.

1.3 Objectives of research

The overall objective of this research is to investigate the thermal cooling of semi-conductors like LEDs with three devices, viz., a FHS, a FHS-VC assembly and a FHS-TE assembly. More specifically, the following would be investigated:

- Determine the natural and force convection heat transfer coefficients in a FHS.
- Visualise the thermal heat spreading effect in a FHS under two-dimensional heat flow.
- Evaluate the performance of a VC attached to a FHS.
- Evaluate the performance of a TE attached to a FHS.

In this investigation, the power output of a LED is simulated using an ac-powered flat plate electric heating element in order to be able to determine the exact heat dissipated from the device.

1.4 Outline of dissertation

Chapter 1 describes the background of thermal management of electronic devices. The FHS, VC and TE are introduced together with the objectives of this research. Investigations with the two types of FHSs are described in Chapter 2. A thermal model and thermal resistance network for two-dimensional heat flow are proposed. CFD simulation is introduced in Chapter 3. Results of obtained from experiments and CFD simulations are compared. The thermal performance of a FHS incorporated with a VC (FHS-VC) is investigated in Chapter 4. A thermal model and thermal resistance network for the FHS-VC assembly is presented. Experimental results are presented. A comparison of the performance of the FHS with and without the VC is made. A FHS incorporated with a TE module (FHS-TE) is investigated in Chapter 5. A thermal model and thermal resistance network for the FHS-TE assembly is presented. A method to determine the hot side TE temperature is proposed. Experimental results and comparison with theory is made. Suggestions for future work are made in Chapter 6. Chapter 7 concludes the study.

CHAPTER 2

FIN HEAT SINK

2.1 Literature survey

Yang et al. (2014) investigated the effect of thermal conductivity and substrate thickness on thermal heat spreading resistance of a high power LED module. Their results showed that the thermal resistance increased as substrate thickness decreased. They also showed that the thermal resistance of graphite composite with anisotropic substrate is 12 – 14% smaller than aluminium substrate with the same thickness. They concluded that the effect of thermal conductivity of substrate material for high power LEDs is important to reduce thermal spreading effect.

Rahmani et al. (2016) numerically calculated the thermal spreading resistance of a curved edge heat spreader. They also investigated the effect of boundary conditions, heat source length and Biot number on spreading resistance. Their results showed that thermal resistance of a rectangular-edge heat spreader was smaller than for a curved edge. This is because the rectangular-edge heat spreader has bigger conductive area.

Ellison (2003) presented a dimensionless solutions for maximum and source-averaged thermal spreading resistance. He solved the 3-D heat conduction equation for rectangle heat source centred on a rectangular plate. Razavi et al. (2016) presented a review on the thermal heat spreading resistance problem. They stated that the important factors for modelling the thermal spreading resistance are sink, source and edge boundary conditions. Generally, thermal heat spreading resistance using a modelling approach involves geometry, properties and boundary conditions.

Li et al. (2016) numerically investigated natural heat transfer cooling around a radial heat sink with perforated ring. The overall diameter and height of the heat sink were 30 mm and 38 mm, respectively. The heat sink~~s~~ is made of 6061 T6 aluminium alloy. Ambient temperature was set at 20 °C in the simulation. Their results showed that thermal resistance of the radial heat sink with six perforated rings was lower than heat sink without perforated ring.

Rao and Waghmare (2015) presented a design optimization of plate fin heat sink equipped with through flow and impingement flow air cooling system. They suggested to use a teaching-learning-based optimization (TLBO) algorithm for the plate fin heat sink optimization. They showed that the TLBO algorithm was better when optimizing the heat sink with flow through air inlet system. Their results also showed the heat sink with flow through air cooling system ~~was~~ performed better compared to impingement flow cooling system.

Kim (2012) carried out a thermal optimization of plate-fin heat sinks with various fin thickness under natural convection cooling condition. Their design allowed the fin thickness to vary in a direction normal to the fluid flow.

The model was based on the volume averaging theory (VAT). Their results showed that thermal resistance decreased by up to 10% when thickness of fin increased in a direction normal to fluid flow. The results also showed that the effectiveness of fins decreased with fin height and heat flux.

Chen et al. (2012) investigated heat transfer characteristics of plate-fin heat sinks with various fin spacing. The heat sinks were placed in a wind tunnel with an AC rotary fan to control the air flow velocity. They concluded that commercial software in conjunction with inverse method and experimental data can be used to determine heat transfer coefficient and fin efficiency.

Shaeri and Yaghoubi (2009) presented a numerical investigation on thermal enhancement for heat sink by using perforated fins. They modelled an array of rectangular fins with 1 to 8 perforations on each fin. The results showed that the thermal performance increased with increase in number of perforations. Perforated fins also reduced its weight.

Kim et al. (2012) explored the effect of orientation angles on an aluminium pin fin heat sink with hollow fins. The base of the heat sink measured 75 mm × 75 mm x 15 mm thick. Their results showed that the thermal resistance of the heat sink was about 15% lower than traditional solid pins fin heat sink under natural convection.

2.2 Theoretical model and thermal resistance network

A conventional FHS dissipating heat from a heat source to the ambient is shown in Figure 2.1(a). An aluminium block is placed between the FHS and the heat source to distribute the heat evenly. Insulation is provided all around the heat source and the aluminium block. Heat is assumed to be dissipated to the ambient only via both the finned and unfinned portions of the FHS by either natural or by forced air convection. The heat source is assumed to be smaller than the FHS.

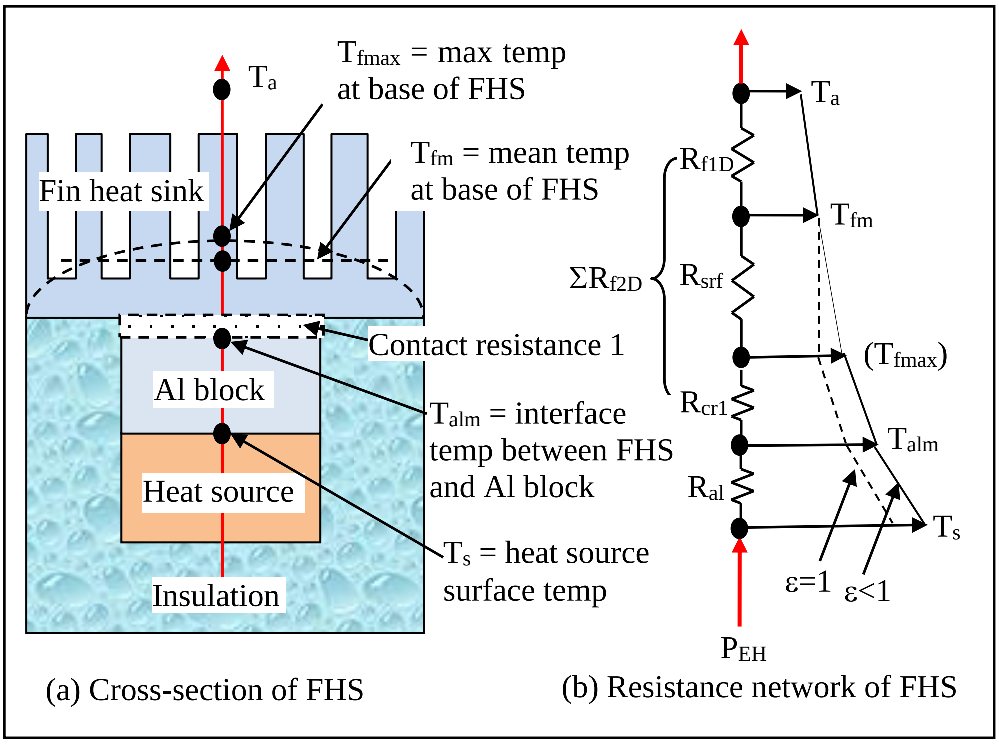

Figure 2.1 Thermal and resistance network for fin heat sink.

Aspect ratio (ε) is defined as the ratio of heat source-to-FHS contact surface area

$$\varepsilon = \frac{A_{heat\ source}}{A_{heat\ sink}} \tag{2.1}$$

Thermal heat spreading occurs when the heat source is smaller than the heat sink or when $\varepsilon < 1$. As a result of thermal heat spreading, the temperature distribution on the base of the FHS would not be uniform. A thermal resistance network model for the system is shown in Figure 2.1(b). As a result of thermal heat spreading, there would be a maximum temperature (T_{fmax}) at the centre and a mean temperature over the surface (T_{fm}). The dashed line ($\varepsilon = 1$) shows the temperature profile in the absence of heat spreading. Thermal contact resistance between the FHS and aluminium block results in mean aluminium block surface temperature (T_{alm}) being higher than T_{fm}. The heat source surface temperature (T_s) is assumed uniform. In this study, we assume that 1-dimensional heat flow occurs when $\varepsilon = 1$ and 2-dimensional when $\varepsilon < 1$. The fin resistance of the FHS under 1-dimensional heat flow is given by R_{f1D}. In the presence of thermal heat spreading, the total 2-dimensional thermal fin resistance of the FHS is given by ΣR_{f2D}.

The thermal resistance of the aluminium block may be determined experimentally from

$$R_{al} = \frac{(T_s - T_{alm})}{P_{EH}} \tag{2.2}$$

The thermal contact resistance at the interface between the aluminium block and base of the FHS is determined from

$$R_{cr1} = \frac{(T_{alm} - T_{fmax})}{P_{EH}} \tag{2.3}$$

The thermal heat spreading resistance is calculated from

$$R_{srf} = \frac{(T_{fmax} - T_{fm})}{P_{EH}} \tag{2.4}$$

and the one-dimensional thermal resistance of the FHS from

$$R_{f1D} = \frac{(T_{fm} - T_a)}{P_{EH}} \tag{2.5}$$

Total two-dimension thermal resistance of the FHS is assumed as

$$\Sigma R_{f2D} = R_{cr1} + R_{srf} + R_{f1D} \tag{2.6}$$

or it may be experimentally derived from

$$\Sigma R_{f2D} = \frac{(T_{alm} - T_a)}{P_{EH}} \tag{2.7}$$

Thermal interface material (TIM) is commonly applied between the base of the FHS and the heat source underneath it. The contact resistance (R_{cr1}) could be estimated from

$$R_{tim} = \frac{\Delta x_{tim}}{k_{tim}\ A_{tim}} \tag{2.8}$$

Theoretical calculations of thermal resistance (R_{f1D}) of a FHS under 1-dimensional heat transfer condition are given by Incropera. An isometric view of a heat sink with conventional rectangular straight fin and wall combination is shown in Figure 2.2(a) and the temperature distribution along the fin in Figure 2.2(b).

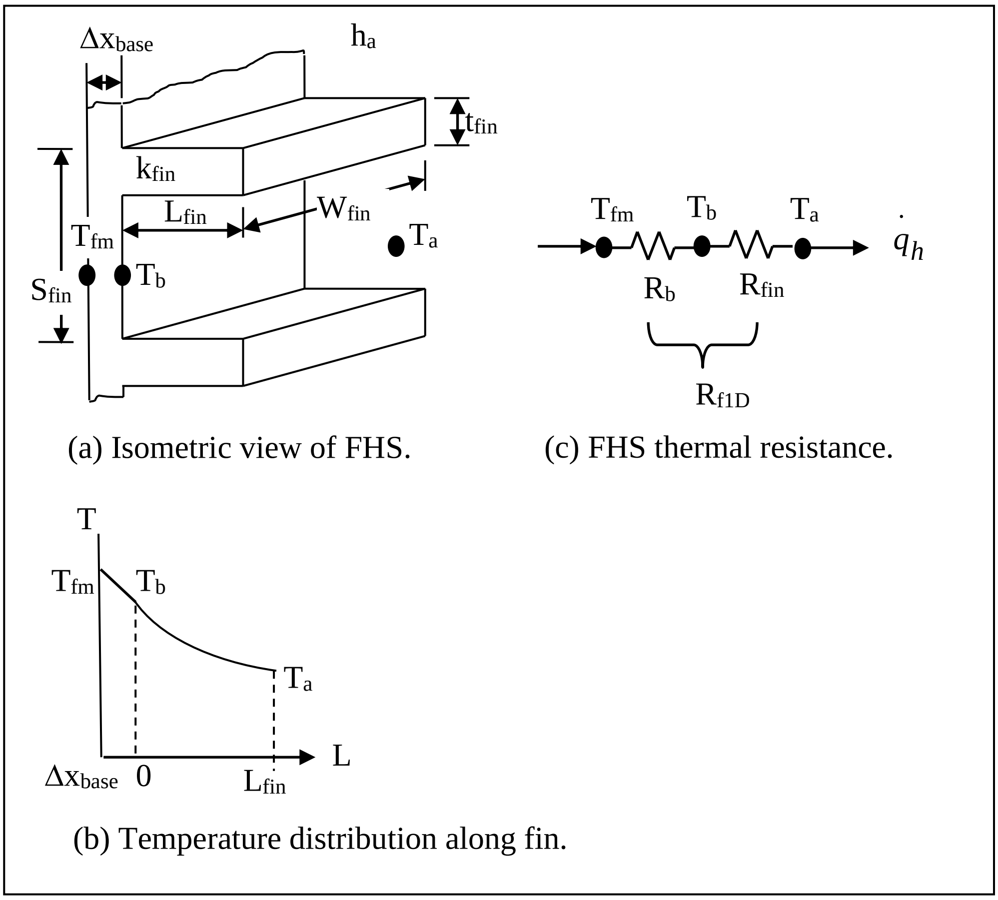

Figure 2.2 Thermal resistance of rectangular profile FHS for 1-D heat flow.

Fin efficiency is defined as

$$\eta_{fin} = \frac{\tanh(m_{fin} \; L_{fin,c})}{(m_{fin} \; L_{fin,c})} \qquad (2.9)$$

where

$$m_{fin} = \sqrt{\frac{2\,(W_{fin} + t_{fin})\, h_a}{W_{fin}\, t_{fin}\, k_{fin}}} \qquad (2.10)$$

and corrected fin length

$$L_{fin,c} = L_{fin} + \frac{t_{fin}}{2} \qquad (2.11)$$

The total heat transfer surface area of a FHS with a number of fins (N_{fin}) is given by

$$A_t = N_{fin}\, A_{fin} + A_{fin,b} \qquad (2.12)$$

where heat transfer surface area of each fin is

$$A_{fin} = (2L_{fin} + t_{fin})\, W_{fin} \qquad (2.13)$$

and total heat transfer surface area of non-finned or bare portion of the FHS array is

$$A_{fin,b} = (S_{fin} - t_{fin})\, W_{fin}\, (N_{fin} - 1) \qquad (2.14)$$

The overall surface fin efficiency of a multi fin array and the base surface to which they are attached to is given by

$$\eta_o = 1 - \frac{N_{fin}\, A_{fin}}{A_t}(1 - \eta_{fin}) \qquad (2.15)$$

The total heat transfer rate from the FHS is shown in Figure 2.2(c) and is given by

$$\dot{q}_h = \eta_o \; h_a \; A_t \; (T_b - T_a) \qquad (2.16)$$

The thermal resistance of the surface of the FHS is calculated from

$$R_{fin} = \frac{1}{\eta_o \; h_a \; A_t} \qquad (2.17)$$

For a plane wall of thickness Δx_{base}, wall thickness resistance is given by

$$R_{base} = \frac{\Delta x_{base}}{k_{fin} \; W_{fin} \; [S_{fin}(N_{fin} - 1) + t_{fin}]} \qquad (2.18)$$

The total thermal resistance of the FHS under 1-D heat flow from Figure 2.2(c) may be theoretically calculated from

$$R_{f1D} = R_{fin} + R_{base} \qquad (2.19)$$

2.3 Experimental investigation

Experiments to investigate the performance of a FHS were performed in two stages. The first stage (Series A) was conducted to determine the heat transfer coefficient (h_a) with a conventional FHS under NC and FC air cooling and 1-dimensional heat flow. In this series the aspect ratio ε was equal to 0.79. Heat spreading effect was assumed negligible and the heat transfer was assumed to be 1-dimensional. The second stage (Series B) was conducted to evaluate the performance of the FHS under NC air cooling and 2-dimensional heat flow. Here, a larger FHS was employed and the aspect ratio (ε) was equal to 0.053 and the effects of thermal heat spreading was determined.

2.3.1 Experimental apparatus

The apparatus set up for the first Series A tests is shown in Figure 2.3. The aluminium FHS, denoted here as FHS#1 measured 45 mm × 45 mm with a 10 mm thick base. It has five fins 30 mm long fins. An electric ac-powered heating element measuring 40 mm × 40 mm × 4 mm was employed to supply the heat input (P_{EH}). The aspect ratio ε was equal to 0.79. A 5 mm thick aluminium block with similar base dimensions was located between the FHS#1 and the heating element to spread out the heat evenly. Type T copper-constantan thermocouples were employed to measure temperatures. Four holes were drilled from the top of FHS#1 and thermocouples inserted through these holes to measure the surface temperatures (T_{f1} – T_{f4}) of the top of the aluminium block. The locations of these thermocouples are shown in Figure 2.4. The mean surface temperature of the aluminium block (T_{alm}) is calculated based on the arithmetic average of these four thermocouples. The relatively large aspect ratio ε = 0.79 was expected not to significantly affect the one-dimensional heat transfer flow (no heat spreading) that is assumed in this case. Ambient (T_a) and insulation (T_{ins}) surface temperatures were measured with three other thermocouples. All thermocouples were connected to a data logger and readings logged on every 1 minute. Air circulation was supplied using a desk top electric fan.

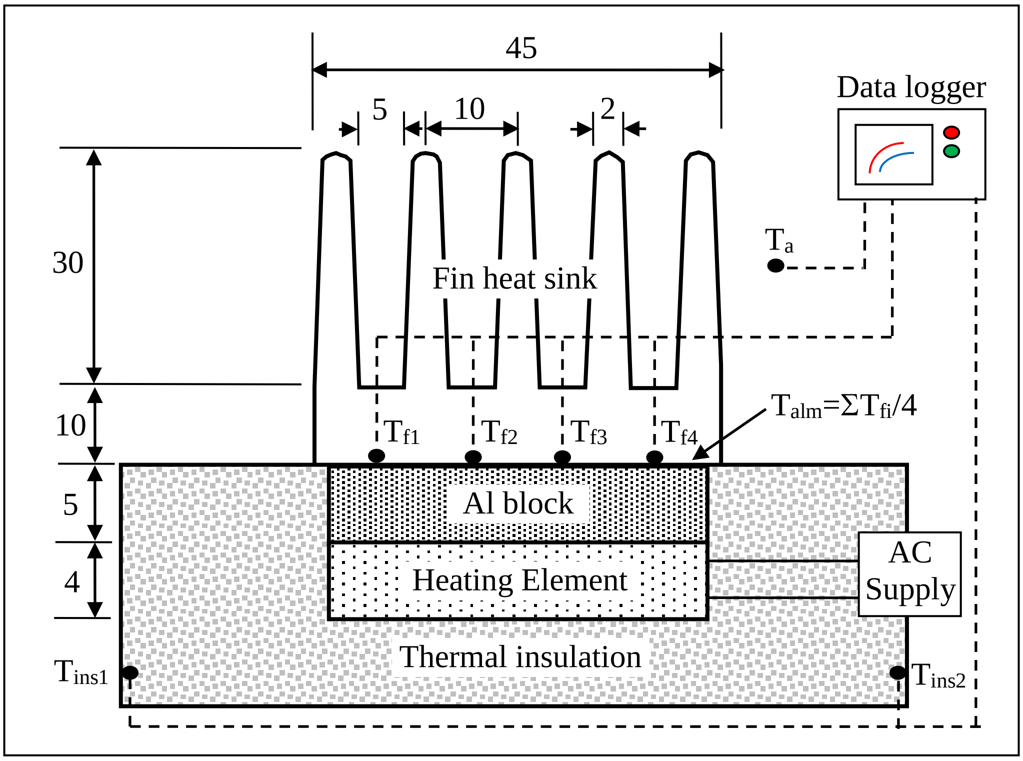

Figure 2.3 Experimental set-up to determine heat transfer coefficient of FHS#1 for ε = 0.79.

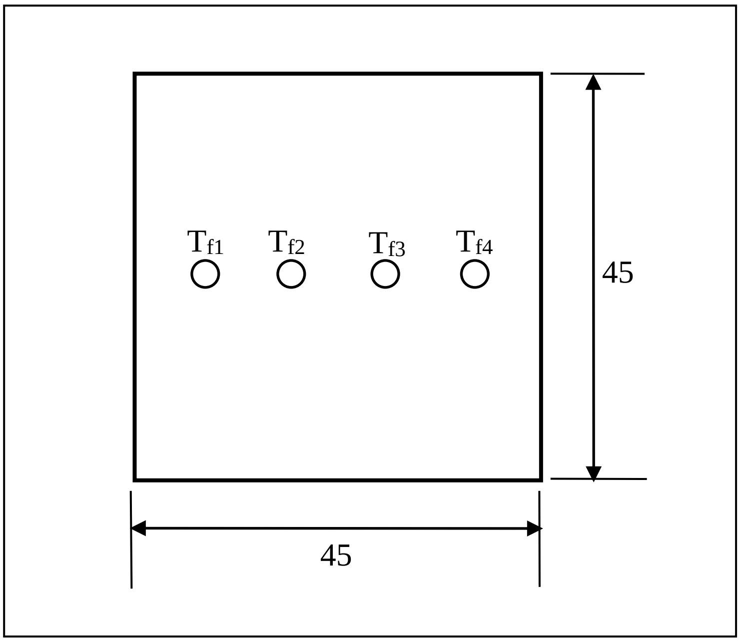

Figure 2.4 Location of thermocouples in FHS#1.

The apparatus set up for the second Series B is shown in Figure 2.5. The larger heat sink measuring 135 mm × 123 mm with 10 mm thick base and with fourteen fins each 30 mm long is denoted as FHS#2. The small aspect ratio $\varepsilon = 0.053$ is expected to produce some heat spreading effect here. An electric ac-powered heating element measuring 30 mm × 30 mm × 5 mm was employed as heat source. A 22 mm thick aluminium block with similar dimensions with heating element was located between the FHS#1 and the heating element. Type T copper-constantan thermocouples were employed to measure temperatures. Twenty one holes were drilled from the top of FHS#2 through to its base to allow thermocouples to be inserted. The locations of these thermocouples are shown in Figure 2.6. The mean temperature (T_{fm}) at the bottom surface of FHS#2 is calculated from the arithmetic average of the twenty one thermocouples (T_{f1}-T_{f21}). The mean surface temperature (T_{alm}) at the top of the aluminium block is calculated from the arithmetic average of the five thermocouples (T_{f7}, T_{f10}, T_{f11}, T_{f12} and T_{f15}). The maximum temperature at the bottom of the FHS (T_{fmax}) is assumed equal to the mean surface temperature of Al block (T_{alm}). Other thermocouples measured the insulation surface temperature ($T_{ins1,}$ T_{ins2}) and the ambient temperature (T_a). An ac power supply provided electrical power (P_{EH}) to the heating element. Power input was controlled using a variable ac voltage regulator.

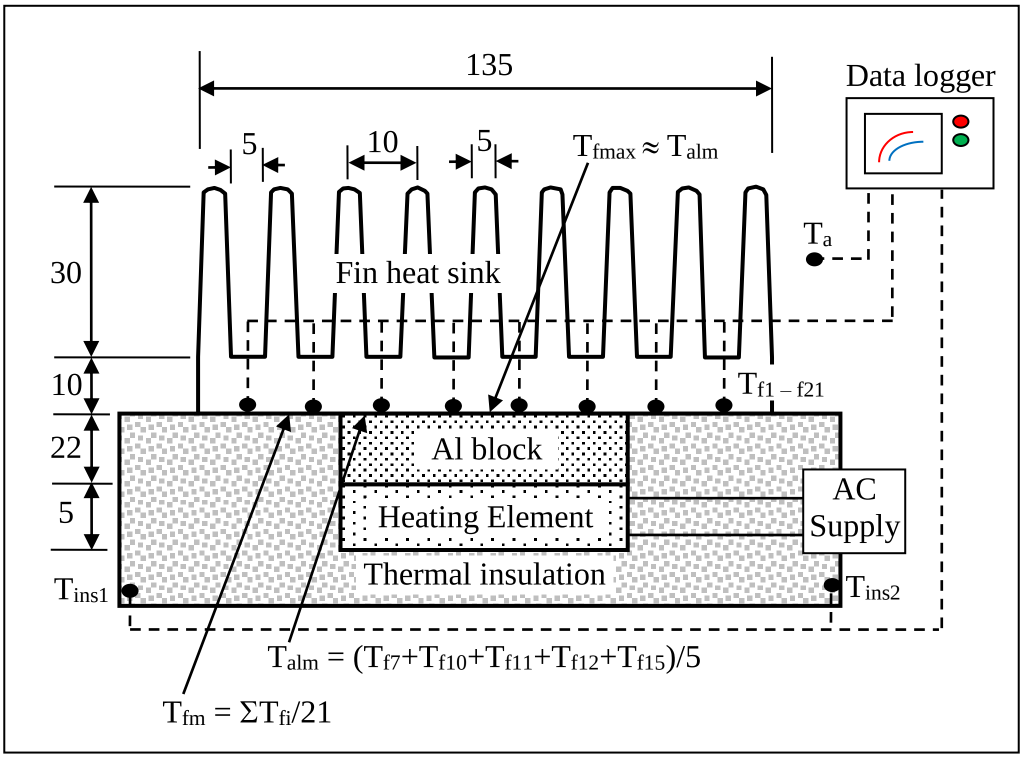

Figure 2.5 Experimental set-up to determine thermal resistance of FHS#2 for $\varepsilon = 0.053$.

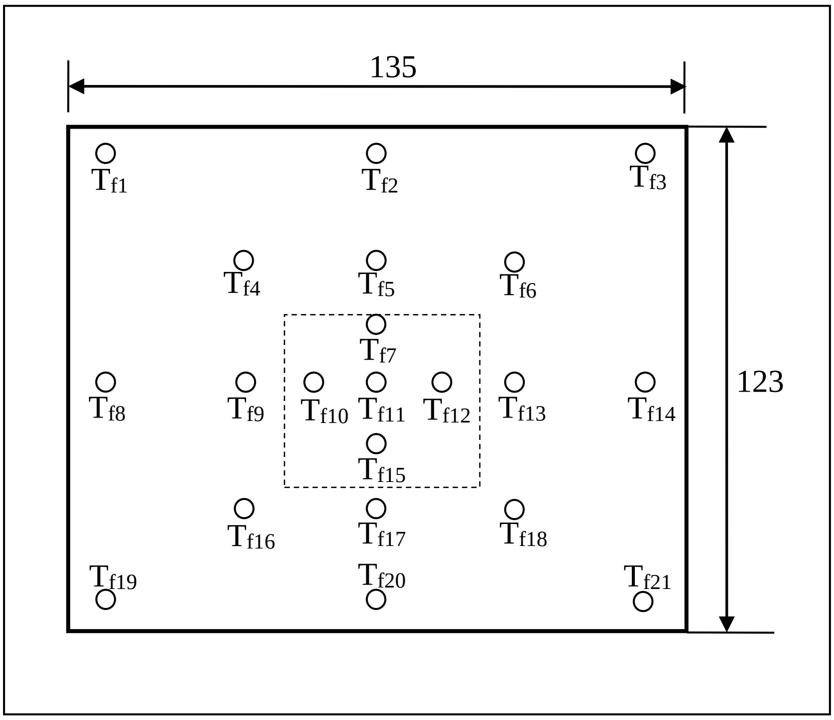

Figure 2.6 Location of thermocouples in FHS#2.

2.3.2 Experimental procedure

Experiments for Series A were conducted under FC and NC air cooling conditions with various power inputs. The power input was adjusted before the start of each experimental run and switched on. Initial power input was at 10 W. The cooling fan was then switched on or kept off, depending upon whether FC or NC conditions were required. Temperatures were then logged using the data logger. Power input was increased after 30 minutes. Experiments were performed at 10 W, 15 W and 20 W power input for NC condition and at 10 W, 20 W and 30 W for FC condition. The experimental runs were conducted three times at each setting to determine the repeatability. The time taken to reach steady state was longer for the NC condition compared to the FC condition. The duration between each power input setting was 30 minutes for FC and 120 minutes for NC. Results for Runs A1 to A6 are tabulated in Table 1.

Experiments for Series B were conducted under NC air cooling condition only at various power inputs (P_{EH}) at 10 W, 30 W and 50 W. Three separate runs were conducted to determine experimental repeatability. Steady state was assumed after 120 minutes at each setting. Results for Runs B1 to B3 are tabulated in Table 2.

2.3.3 Experimental results

Figure 2.7, 2.8 and 2.9 show the transient temperature response for Run A1 – A3, A4 – A6 and Run B1 – B3.

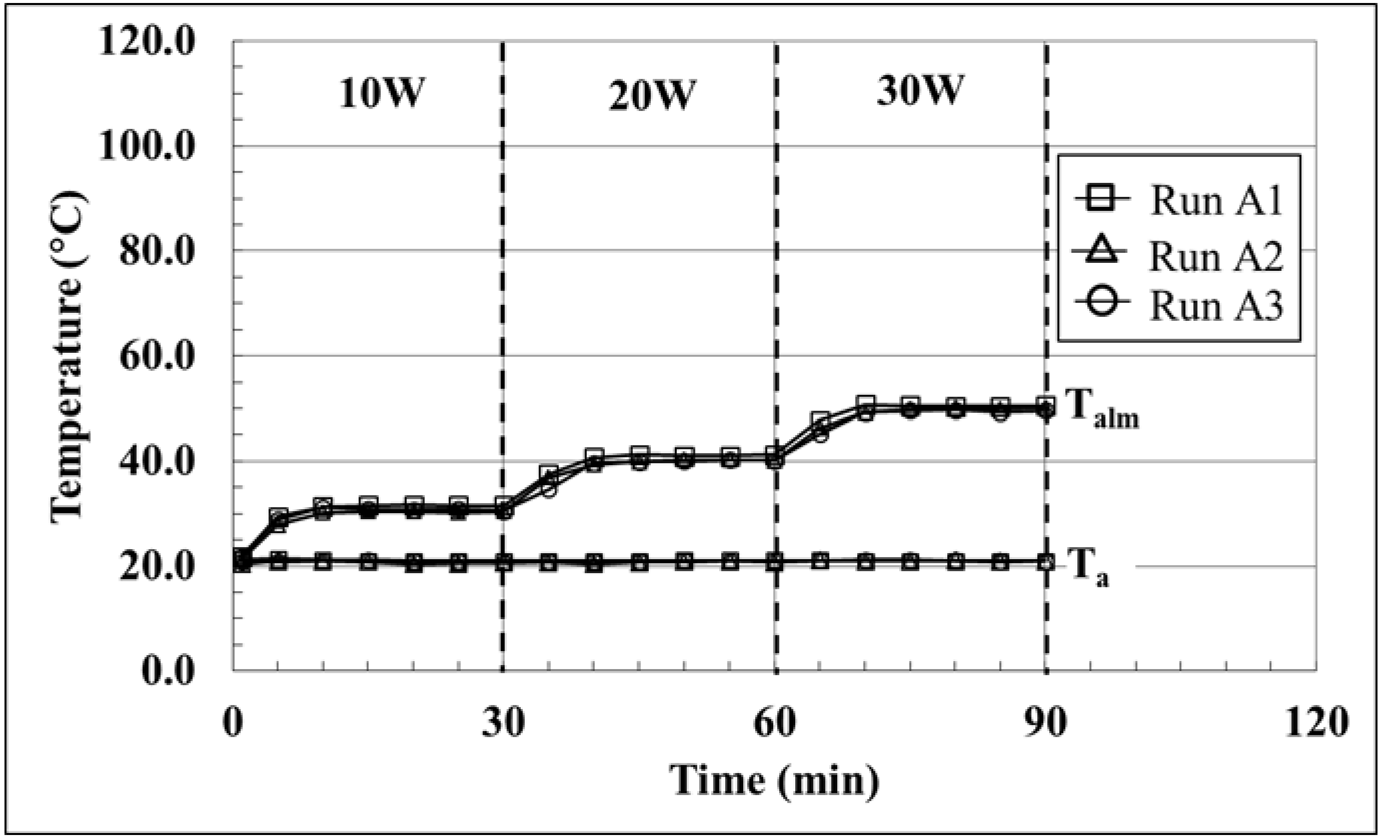

Figure 2.7 Transient temperatures for FHS#1 (FC, ε = 0.79 - Runs A1 – A3).

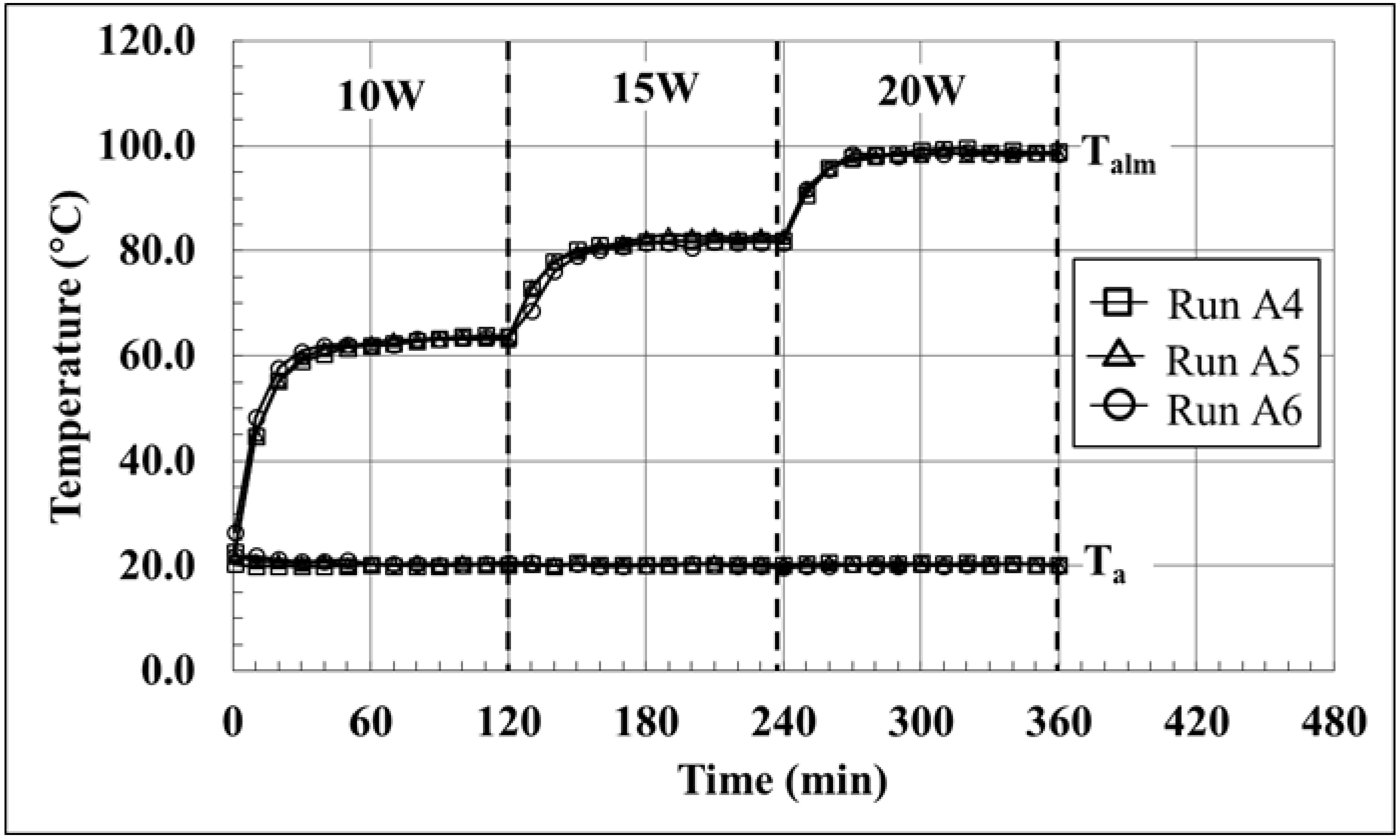

Figure 2.8 Transient temperatures for FHS#1 (NC, ε = 0.79 - Runs A4 – A6).

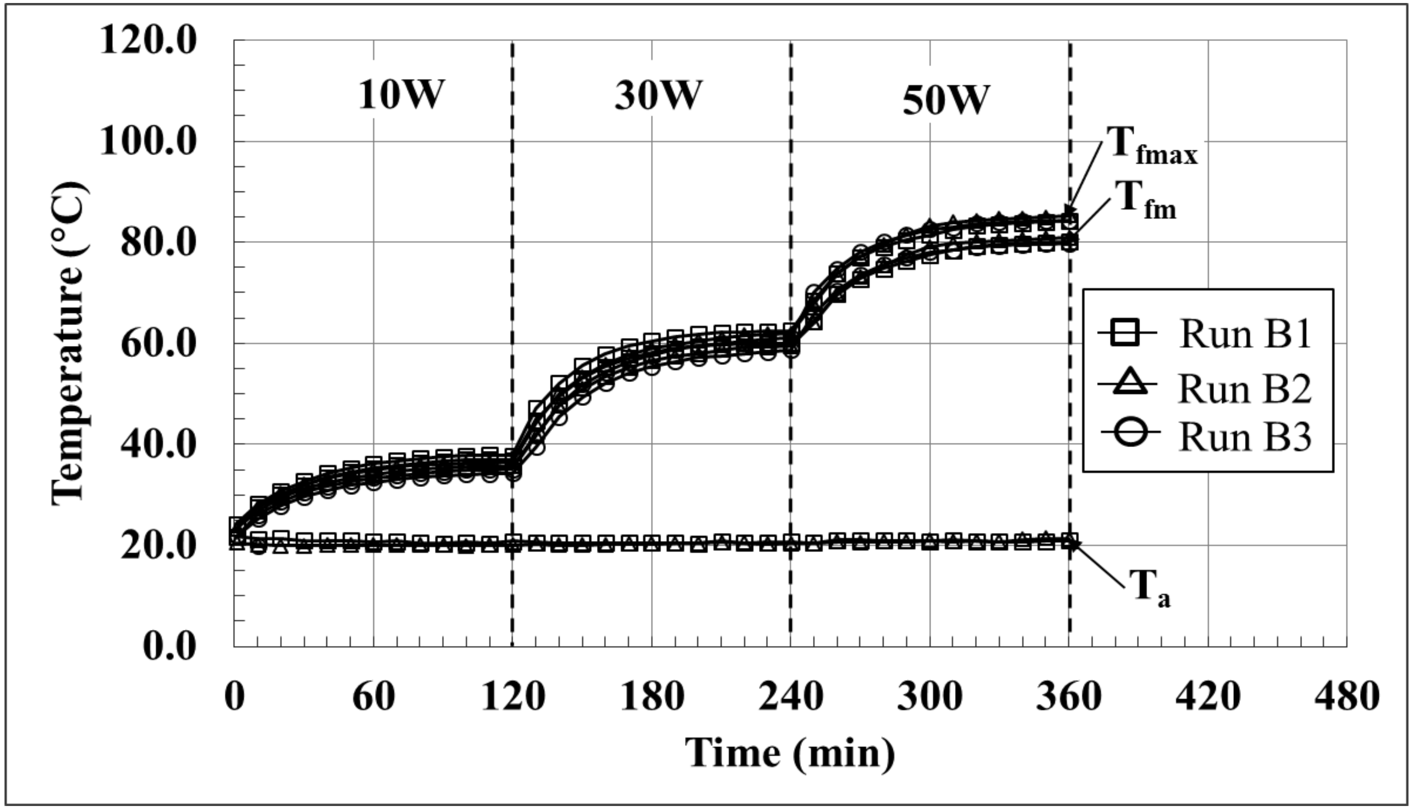

Figure 2.9 Transient temperatures for FHS#2 (NC, ε = 0.053 - Runs B1 – B3).

Temperature distribution along centreline for A1 – A3, A4 – A6 and Run B1 – B3 are shown in Figure 2.10, 2.11 and 2.12.

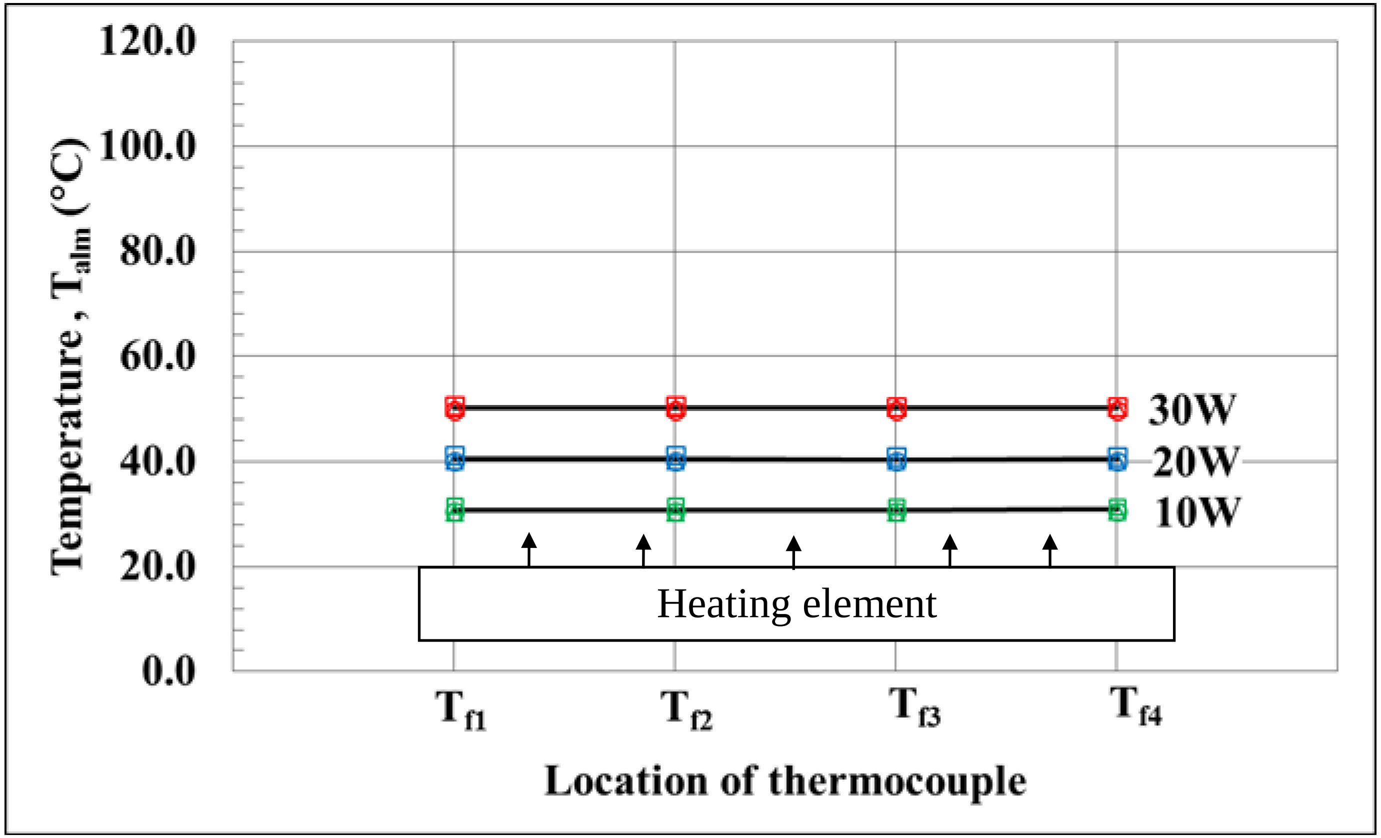

Figure 2.10 Temperature distribution along centerline of FHS#1 (FC, ε = 0.79 - Runs A1 – A3).

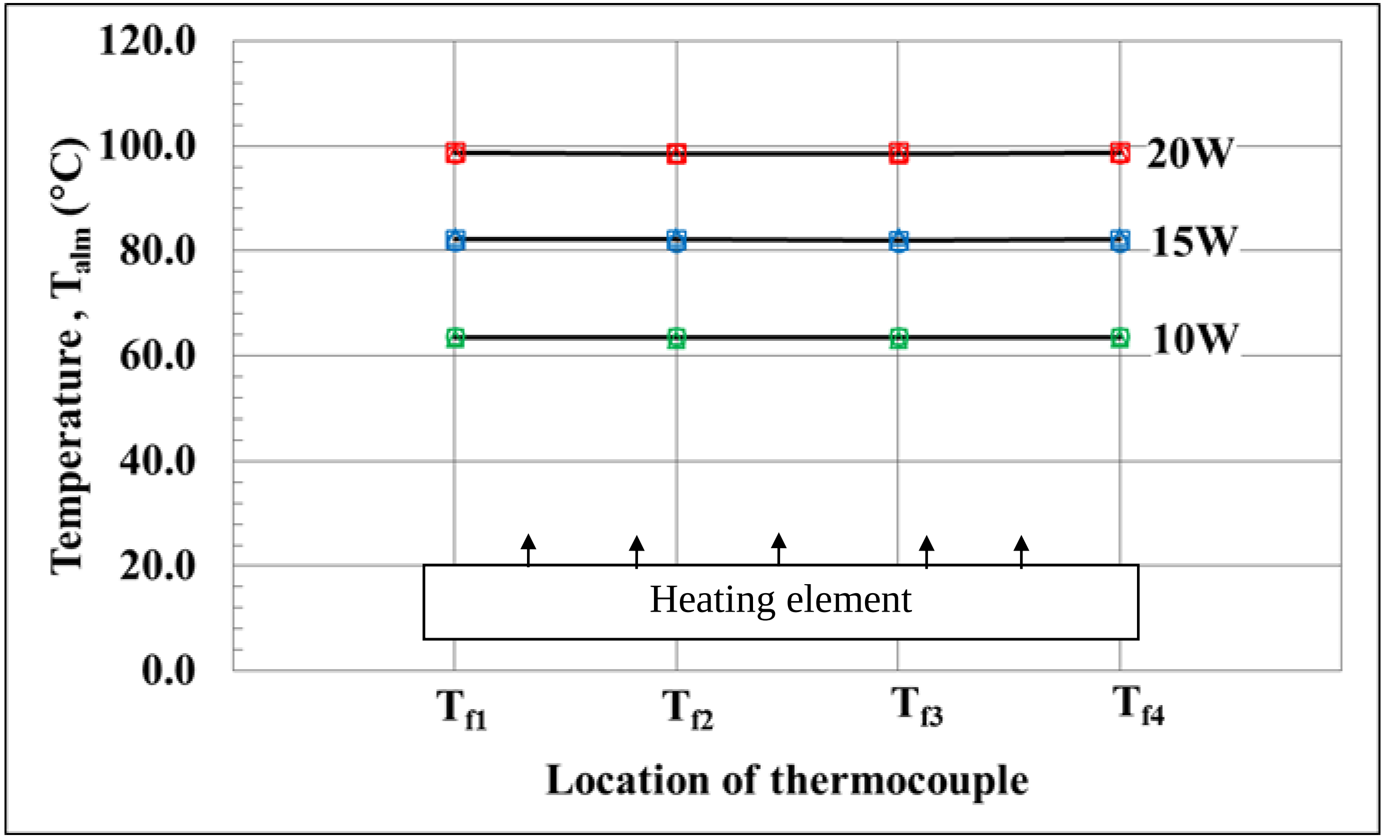

Figure 2.11 Temperature distribution along centerline of FHS#1 (NC, ε = 0.79 - Runs A4 – A6).

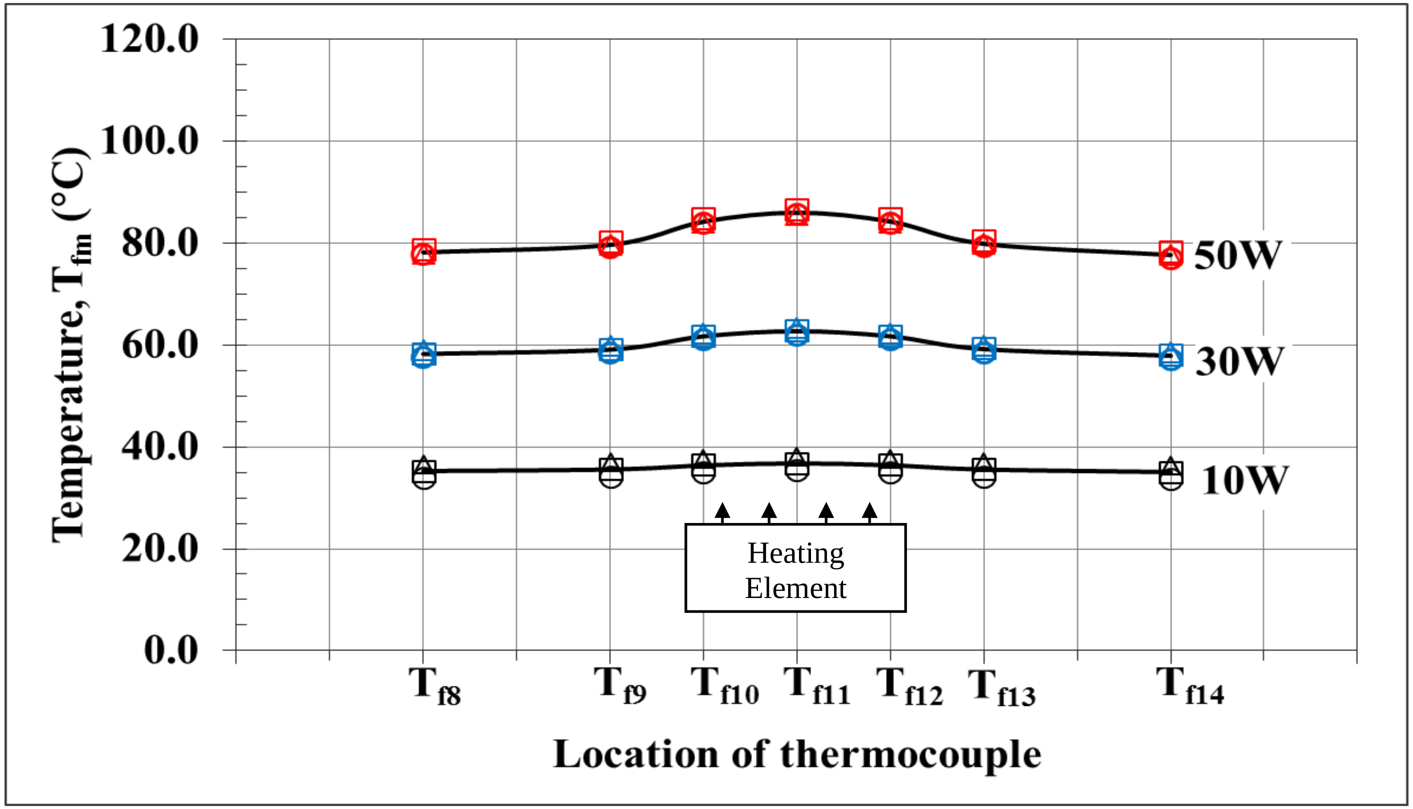

Figure 2.12 Temperature distribution along centerline of FHS#2 (NC, ε = 0.053 - Runs B1 – B3).

Figure 2.13 shows the heat transfer coefficient h_a for FHS#1 (Runs A1 – A6).

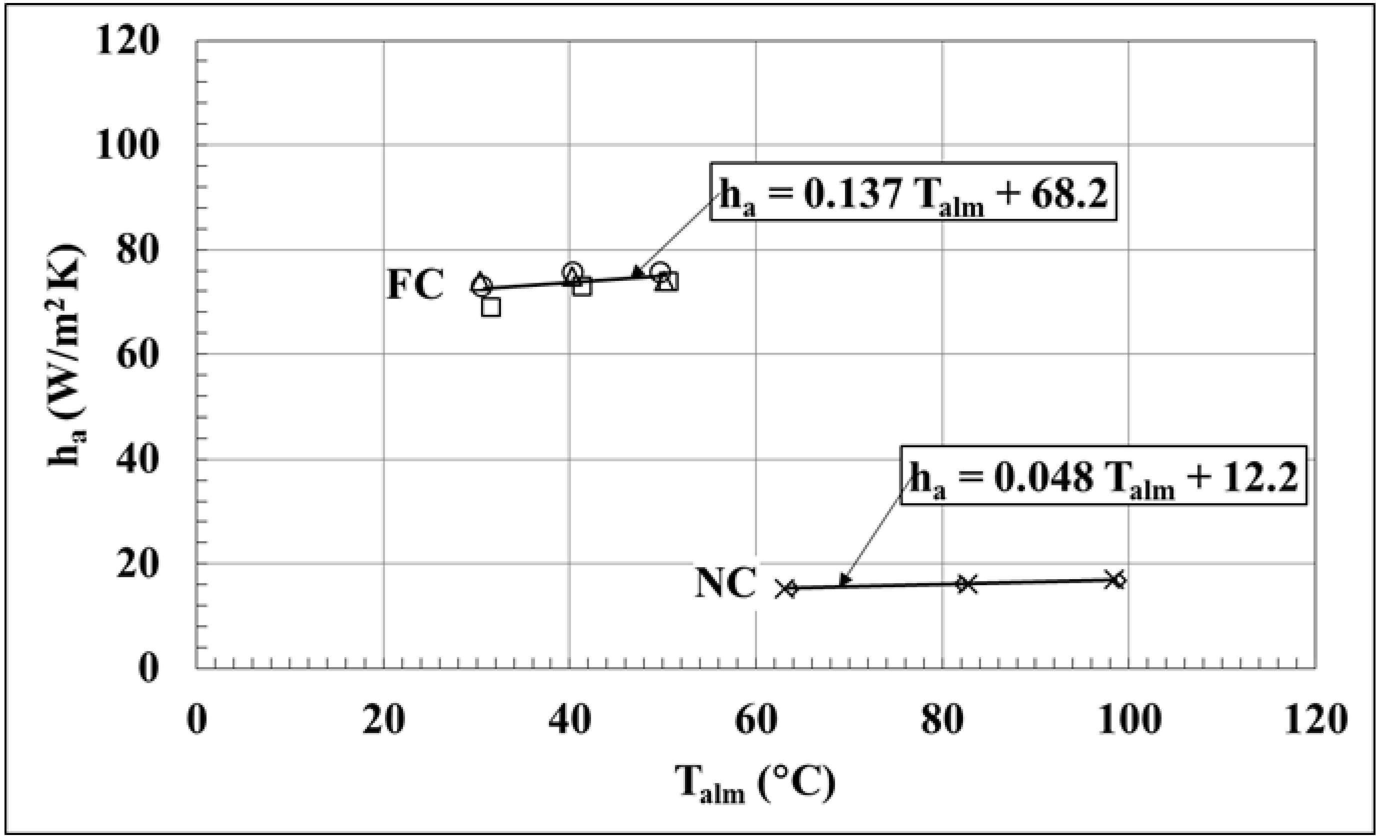

Figure 2.13 Heat transfer coefficient h_a for FHS#1 (Runs A1-A6).

2.4 Discussion of results

Figure 2.7, 2.8 and 2.9 show the experimental transient temperatures obtained for Runs A1 to A3, Runs A4 to A6 and Runs B1 to B3, respectively. The transient temperature results for FHS#1 under FC in Figure 2.7 show that steady state was achieved after 30 min for the FC condition. In general, results were repeatable to within 1°C. The ambient temperature was not kept constant and varied from about 20.7°C to 21.1°C. Figure 2.8 shows that steady state could be achieved after 120 min for NC. All results were generally repeatable to within 1°C. The ambient temperature (T_a) varied from 19.7°C to 20.7°C. Figure 2.9 shows that steady state was achieved after 120 min for FHS#2. The results also show that the experiment was repeatable to within 2°C. The ambient temperature (T_a) varied from 19.8°C to 21.3°C. From the insulation temperature results, heat loss from the sides of the system was estimated to be less than 1% of the power input.

2.4.1 Effect of power input

Figure 2.7 shows that the mean temperature on the base of FHS#1 (T_{fm}) at steady state increased about 10°C with every 10 W increment of P_{EH} under FC. Figure 2.8 shows that it increased about 18.3°C from 10 W to 15 W and about 17°C from 15 W to 20 W. The results show that the increase in temperature is greater at NC condition compared to FC. Figure 2.9 for FHS#2 shows that all temperatures increased about 24°C from 10 W to 30 W and about 21°C from 30W to 50W. In general it was observed that the base temperature of the FHS increased with power input.

2.4.2 Heat spreading effect

The temperature distribution at the base of the FHS#1 are measured by thermocouples (T_{f1} – T_{f4}) along the centreline under FC and NC as shown in Figures 2.10 and 2.11, respectively. It could be seen that the temperature distributions are quite uniform, varying by about only 0.1°C for all three different power inputs. Hence it can be concluded that one dimensional heat transfer is occurring and there is no heat spreading. The temperature distribution at the base of FHS#2 with three power inputs (10 W, 30W and 50 W) are shown in Figure 2.12. Probes T_{f10}, T_{f11} and T_{f12} show the temperatures measured at the top of the aluminium block while probes T_{f8}, T_{f9}, T_{f13} and T_{f14} show the temperatures measured from thermocouples pushed through from the top of the FHS#2 to the bottom surface along the centreline. It could be seen that the temperature distribution at the base of the FHS#2 is not uniform, varying by up to 4.6°C at high power input due to thermal heat spreading.

2.4.3 Heat transfer coefficient h_a

In Table 1, total fin resistance (ΣR_{f2D}) was first determined from Equation (2.7). One-dimensional fin thermal resistance (R_{f1D}) was then determined from Equation (2.6) by assuming contact resistance R_{cr1} = R_{tim} =

0.05 K/W. The heat transfer coefficient (h_a) was then evaluated using Equation (2.9 – 2.19) and plotted against base temperature (T_{fm}) in Figure 2.13. The results show that for 1-dimensional heat flow at temperature range of 30°C to 100°C, the heat transfer coefficients for FC vary from about 69.0 to 75.8 W/m^2 K and for NC from 15.2 to 17.0 W/m^2 K. They could be represented by the following linear equations:

for NC $$h_a = 0.048 T_{alm} + 12.2 \tag{2.20}$$

and for FC $$h_a = 0.137 T_{alm} + 68.2 \tag{2.21}$$

2.5 Chapter conclusions

Thermal performances of two FHSs were evaluated. FC cooling resulted in lower temperature than NC air cooling. Thermal heat spreading occurred when the heat source was very much smaller than the FHS. Heat transfer coefficient under FC cooling was higher than NC. Average values of 74 W/m^2 K for FC and 16 W/m^2 K for NC were obtained.

CHAPTER 3

CFD simulation

3.1 CFD simulation software

Computational fluid dynamics (CFD) is a software employed to simulate the flow of fluid and its effect on a targeted object in the flow field. CFD software makes use of applied mathematics, physics and computational software to solve the Navier-Stokes equations used to model the fluid flow together with the associated boundary conditions. It involves the relationship between fluid velocity and pressure together with fluid properties like density and viscosity.

In the early 20th century, CFD was used as a tool for analysing air flow around vehicles such as cars and aircraft. With thermal cooling of electronic devices getting more complicated and demanding, CFD simulation have become useful to analyse the thermal performance of a cooling device for system modelling. CFD simulation reduces the cost and increase the speed of development of the cooling system. It is employed to create a 3D mathematical model on a grid which allows users to rotate and view the simulated temperature and velocity fields from different angles. CFD modelling can help users to identify heat sources and to have a general view of the system. Also, users can easily change the variables and visualize the effect under different circumstances.

3.2 Star-CCM+®

Star-CCM+® developed by CD-adapco™ is a CFD simulation software used in this study. The software provides a user-friendly interface device to model a cooling system. A general workflow sequence of operations must be followed in order to achieve the simulation results. The general sequence of operations is shown in Figure 3.1. The following steps are followed:

1. Star-CCM+® requires a geometry to represent the actual object or scenario. The geometry of the object is first set up according to the actual dimensions and sizes.
2. Parts from the geometrical model are then assigned to regions, boundaries and interfaces of the computational model to construct a simulation topology. These parts represent the discretized portions of the geometry to be analysed while physical models are applied.
3. A mesh for the geometry is then generated. Meshing is a process to discretize the geometry into smaller subdomains commonly in the shape of hexahedra in 3D and quadrilaterals in 2D. Physics solvers or governing equations provide numerical solution and solve for each of these subdomains.
4. Next, the physics on every surface and volume of the object/s are defined. The physics consist of fluid flow, heat transfer, dynamic fluid

body interaction, material properties and other related phenomena. Total heat generated from the heating element/s and material properties such as thermal conductivity of the heat sink are prescribed.

5. Subsequent reports, monitors and plots for analysis are then prepared. Reports are computed numerical data extracted from simulation. Monitors use reports to record the reported data while the simulation is in progress. Plots use the monitored data to show the trends of solution.
6. The simulation process is started after all the preliminary preparations are made. The solution is then initialized and the solver is launched.
7. The simulated results can be visualized through 3D CAD models or plots.

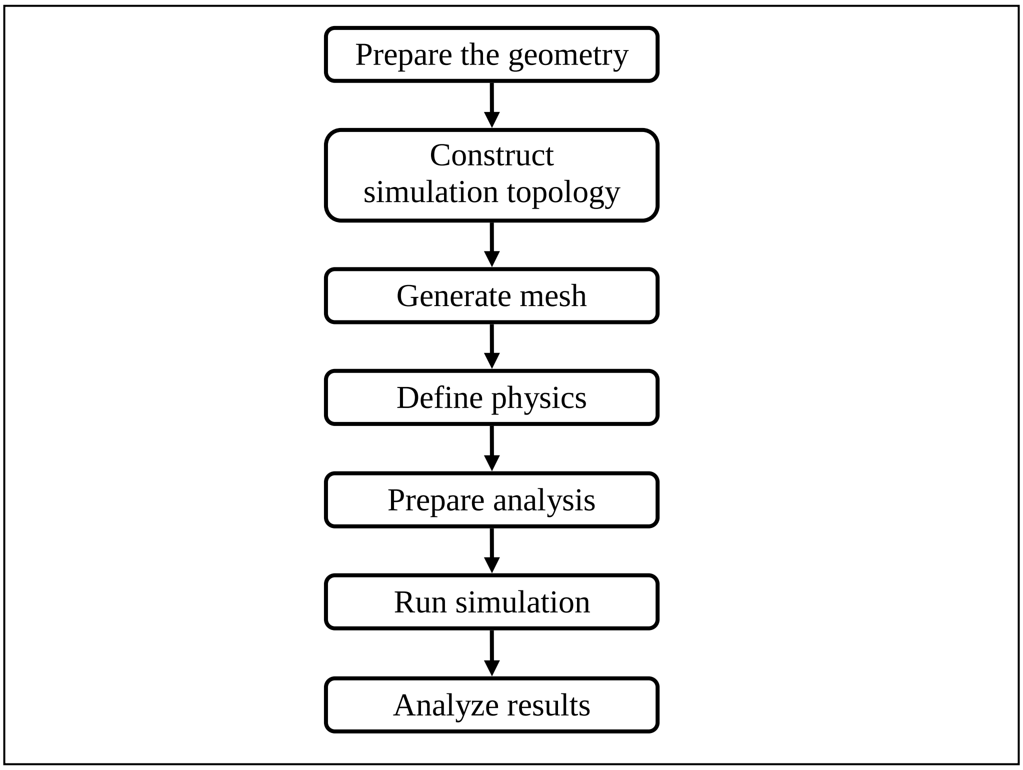

Figure 3.1 General sequence of operations for CFD simulation.

3.3 Typical simulation of FHS with CFD

3.3.1 Temperature distribution

An example of a simulation performed to obtain the temperature distribution in a conventional FHS placed over and heated by a flat plate electrical heater is described here. The model set up is shown in Figure 3.2. Parameters that could affect the performance of the FHS are power input to the heating element (P_{EH}), thermal contact resistance at the interface between the FHS and the heating element (R_{cr}), thermal conductivity (k_{FHS}), dimensions and fin arrangement and whether cooling is performed under NC or FC air flow. A very important parameter is the aspect ratio (ε) that causes thermal heat spreading effect which occurs when there is a large difference between the sizes of the heater and base of the FHS. In this simulation, the FHS was assumed to measure 137 mm wide × 125 mm long with a base thickness of 10 mm. There are fourteen fins each 5 mm thick and 30 mm long. The mesh set up for the study is shown in Figure 3.3. Ambient temperature was assumed constant at 20°C. The heating element and base of the FHS were assumed to be perfectly thermally insulated. The heat transfer coefficient at the boundaries here were set to be equal to 0 W/m^2K. Besides, the heat transfer coefficient at the boundaries of fin were input from 5 $W/m^2 \cdot K$ to 20 $W/m^2 \cdot K$ to simulate the effect of convectional. The following values are input into the program; P_{EH} = 100 W, h_a = 10 $W/m^2 \cdot K$, ε = 0.09, k_{FHS} = 220 W/m K and R_{cr} = 0.5 K/W.

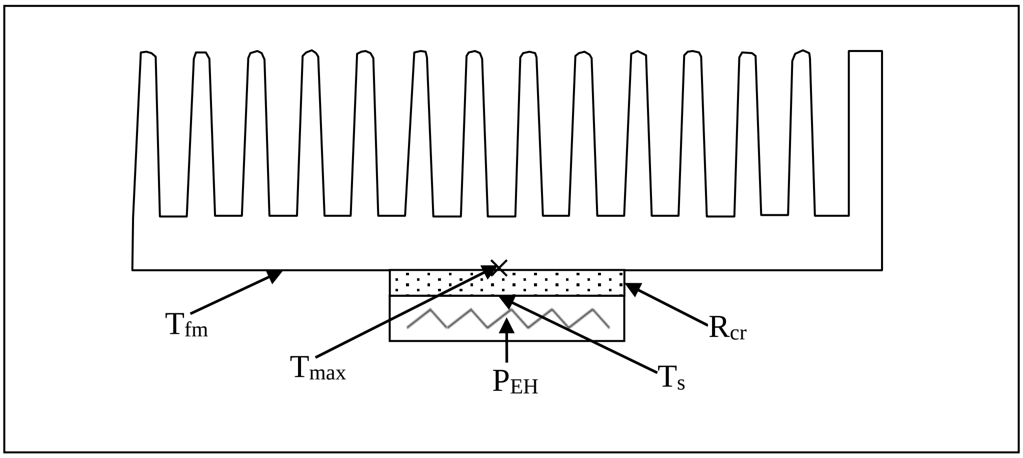

Figure 3.2 Cross-sectional view of model set up for simulation.

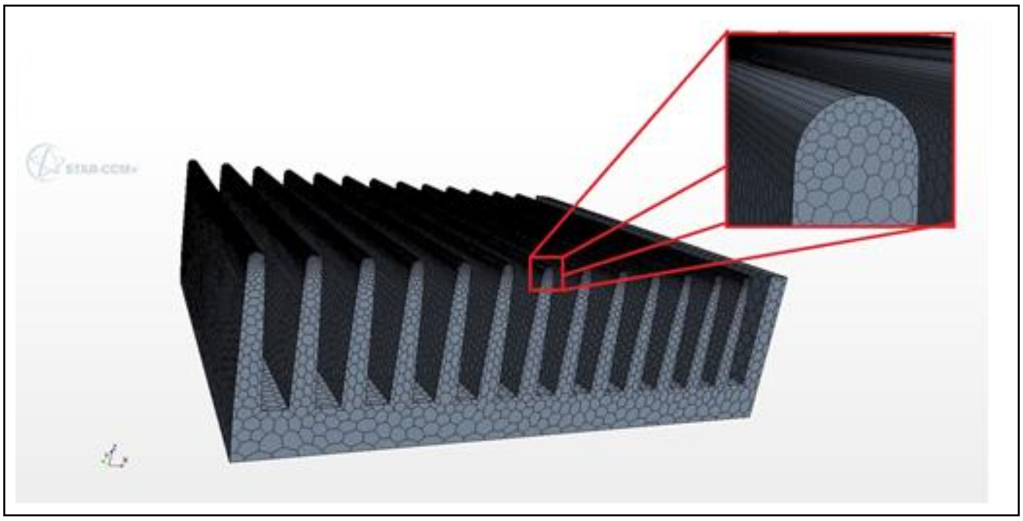

Figure 3.3 Setup of mesh for FHS.

Figure 3.4 shows the output obtained from the simulation. The effect of non-uniform temperature distribution along the base of the FHS as a result of thermal heat spreading is shown. Heat is observed to spread out radially from the heating element to the FHS. The effect of varying input heat (P_{EH}) is shown in Figure 3.5. The simulated results show that heat source surface temperature (T_s), maximum temperature at base of the FHS (T_{fmax}) and mean temperature of the base of the FHS (T_{fm}) all increase with power input. Simulation results showing the effect of heat transfer coefficient (h_a) is shown in Figure 3.6. The simulated results show that all these temperatures decrease with increase of h_a. Further simulation results showing the effect of aspect ratio (ε) is shown in Figure 3.7. The simulated results show that all these temperatures decrease with increase of aspect ratio. The results showing the effect of thermal conductivity of material (k_{FHS}) in Figure 3.8 show that temperatures decrease with increase of material thermal conductivity. Simulation results showing the effect of contact resistance (R_{cr}) is shown in Figure 3.9. The simulated temperature results show that the heating surface temperature increases with increase in contact resistance, as expected. Contact resistance creates a barrier to effective heat transfer.

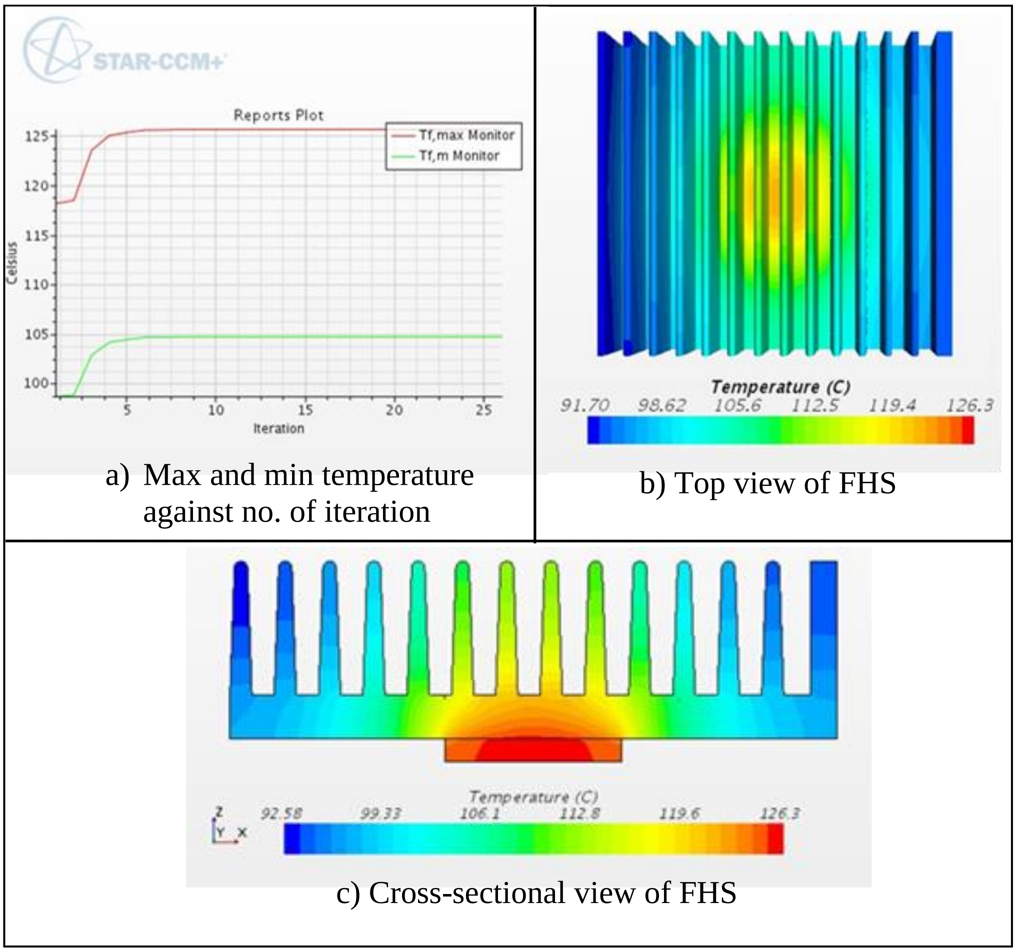

a) Max and min temperature against no. of iteration

b) Top view of FHS

c) Cross-sectional view of FHS

Figure 3.4 Typical simulation output with P_{EH} = 100W and h_a = 10 W/m^2 K.

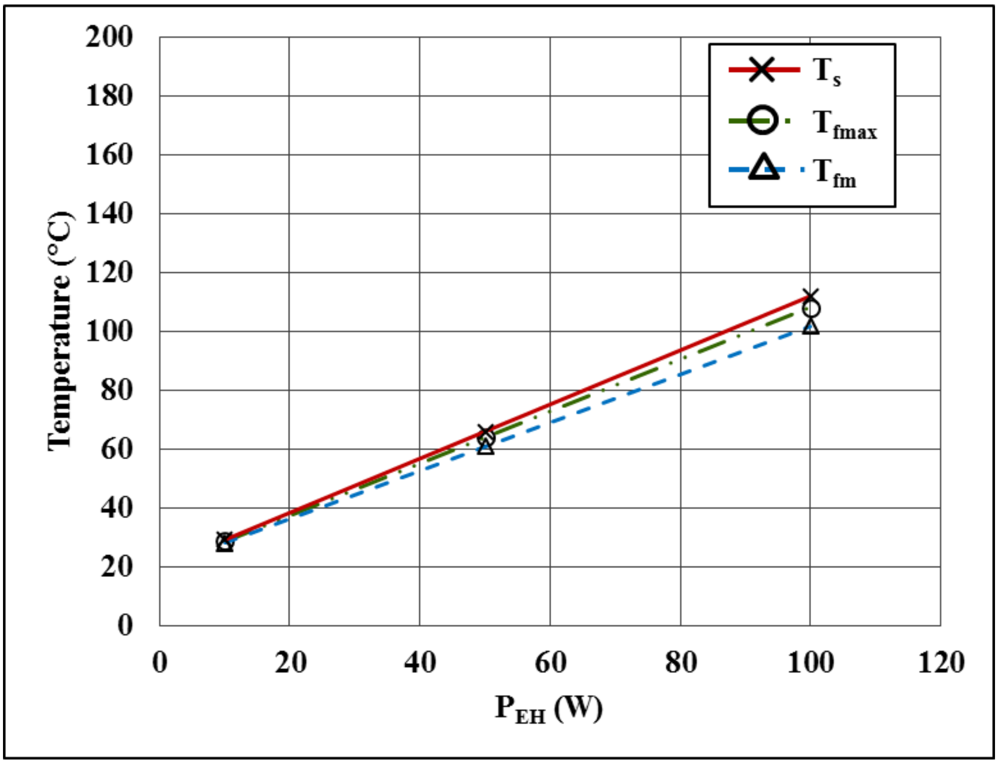

Figure 3.5 CFD simulation showing effect of heat input (P_{EH}) with h_a = 10 W/m^2 K, ε = 0.09 and k_{FHS} = 220 W/m K.

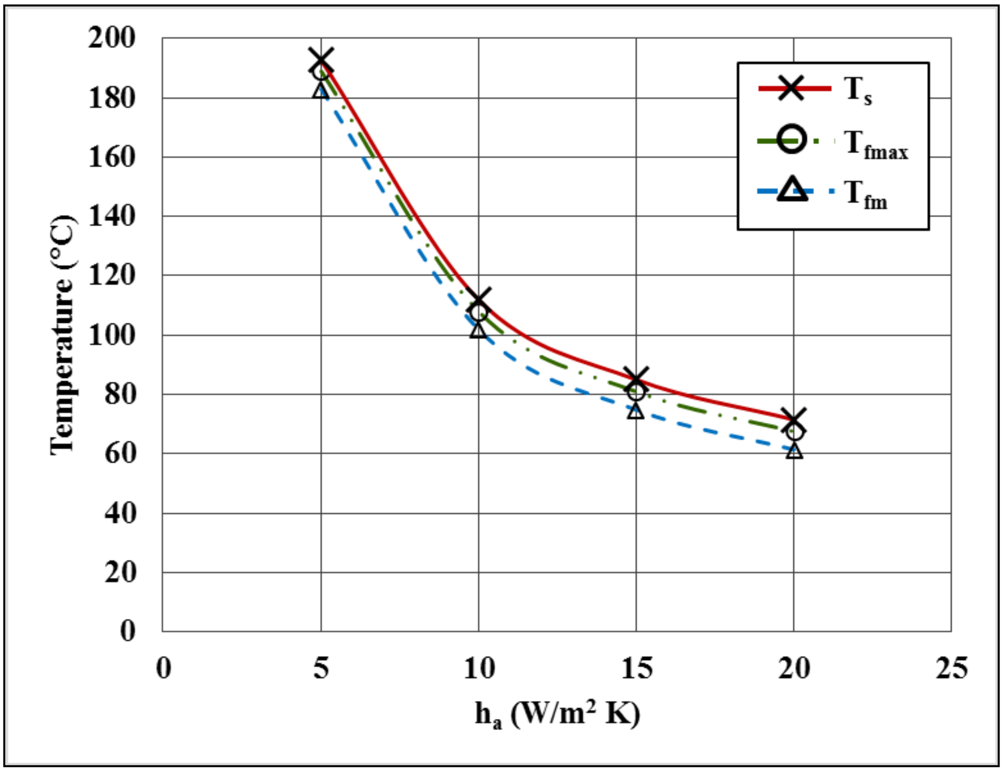

Figure 3.6 CFD simulation showing effect of heat transfer coefficient h_a with P_{EH} = 100 W, ε = 0.09 and k_{FHS} = 220 W/m K.

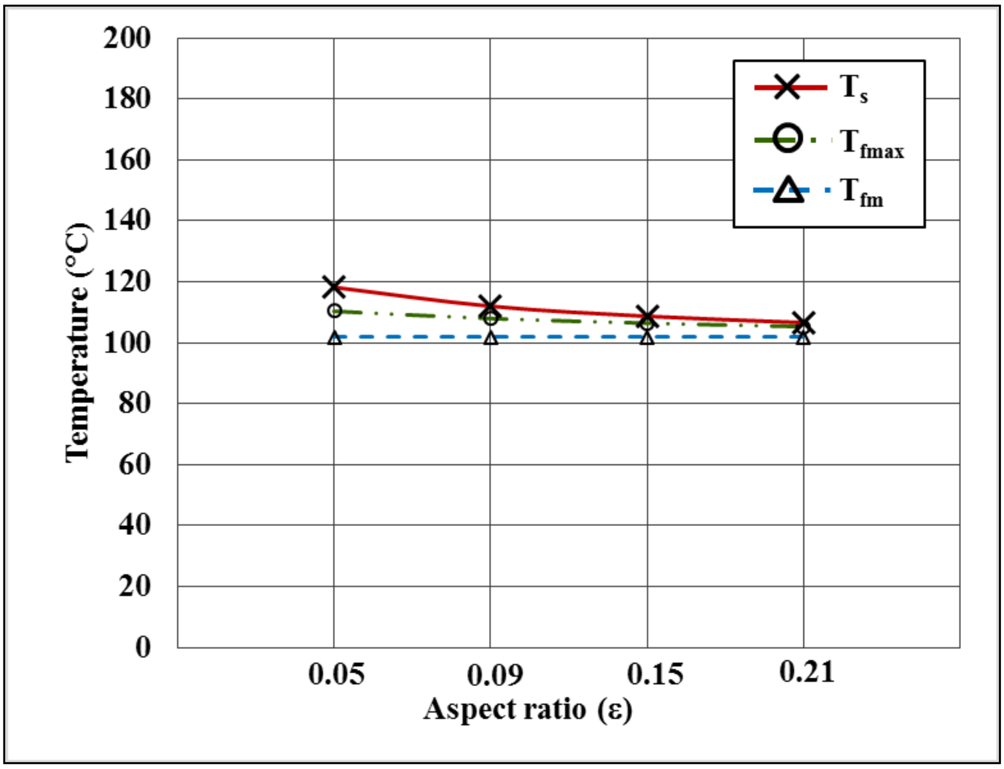

Figure 3.7 CFD simulation showing effect of aspect ratio ε with P_{EH} = 100W, h_a = 10 W/m^2 K and k_{FHS} = 220 W/m K.

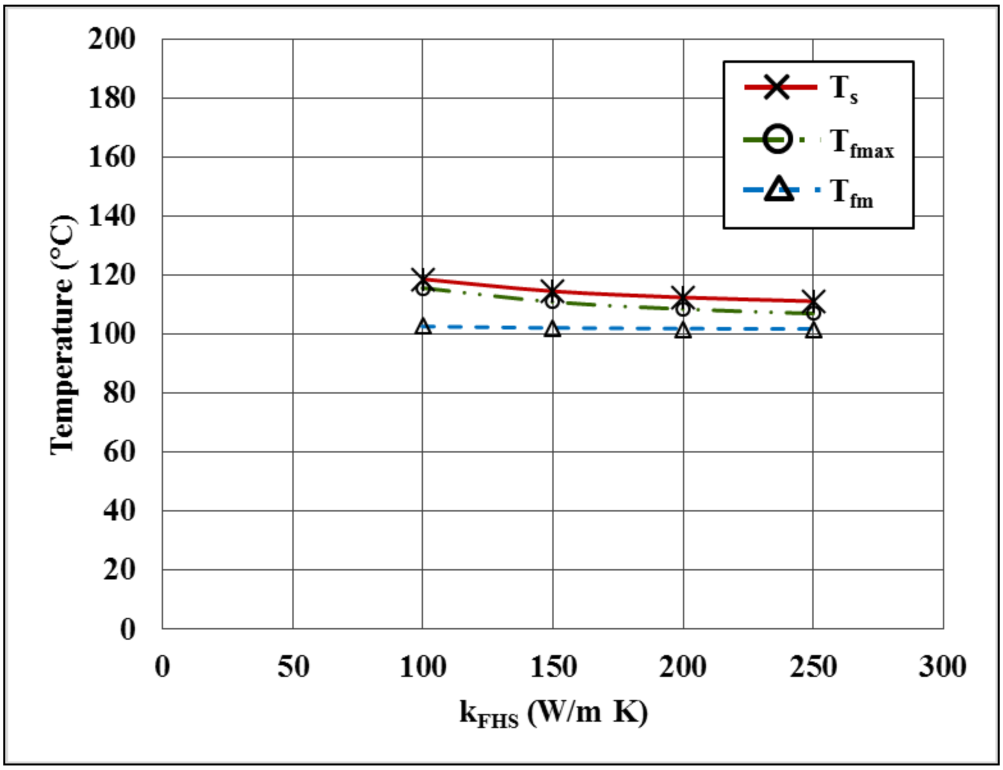

Figure 3.8 CFD simulation showing effect of thermal conductivity k_{FHS} with P_{EH} = 100W, ε = 0.09, h_a = 10 W/m^2 K and k_{FHS} = 220 W/m K.

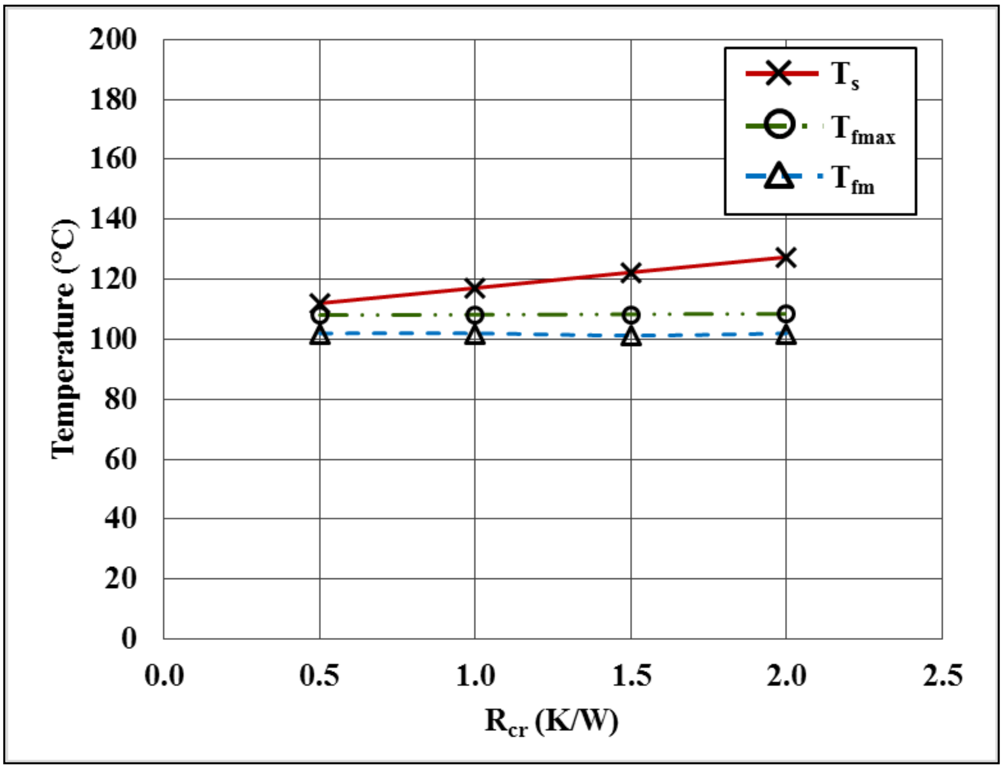

Figure 3.9 CFD simulation showing effect of contact resistance R_{cr} with P_{EH} = 100 W, ε = 0.09, h_a = 10 W/m^2 K and k_{FHS} = 220 W/m K.

3.3.2 Thermal resistance

The thermal resistance network model for the set up in the above typical simulation is shown in Figure 2.1. Thermal heat spreading resistance (R_{srf}) and fin resistance (R_{f1D}) are calculated from the simulated temperature results using Equation (2.4) and (2.5), respectively. The effects of input power, heat transfer coefficient, aspect ratio, thermal conductivity and contact resistance are shown in Figures 3.10 – 3.14, respectively. Figure 3.10 shows that fin resistance (R_{f1D}) and spreading resistance (R_{srf}) are not affected by input power. Spreading resistance is small, about 10% that of fin resistance. The effect of NC and FC air circulation rates is shown in Figure 3.11. FC with higher heat transfer coefficient results in lower resistances compared to NC. Better cooling rates are expected with high air circulation rates in the case of FC. Figure 3.12 shows that low aspect ratio results in increased spreading resistance, as expected because of non-uniform heat distribution. The use of higher thermal conductivity materials results in lower fin and heat spreading resistances. This is shown in Figure 3.13. Figure 3.14 shows that higher thermal contact resistance results in higher total fin resistance.

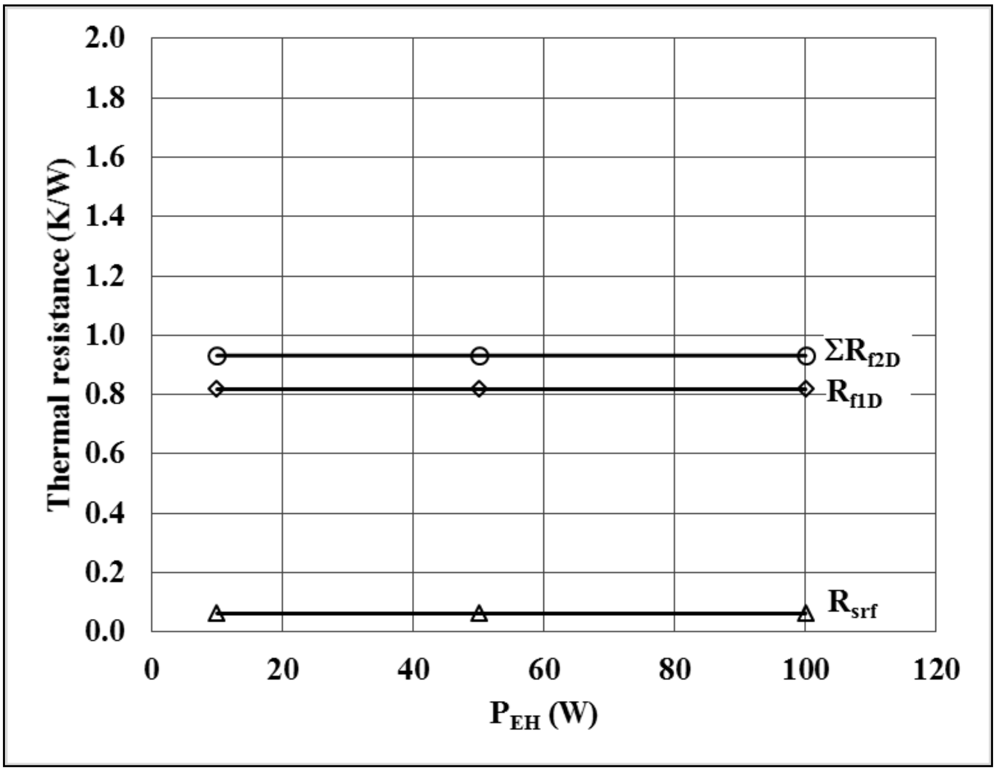

Figure 3.10 CFD thermal resistance simulation showing effect of input power P_{EH} with h_a = 10 W/m^2 K, ε = 0.09 and k_{FHS} = 220. W/m K.

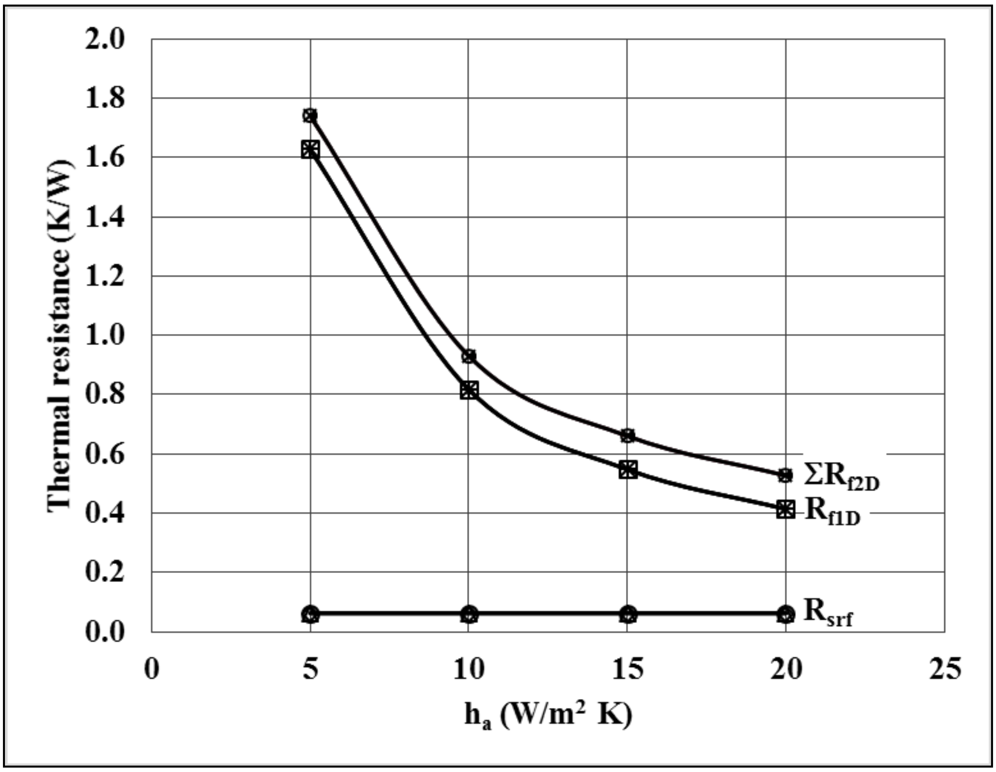

Figure 3.11 CFD thermal resistance simulation showing effect of heat transfer coefficient h_a with P_{EH} = 10 W, ε = 0.09 and k_{FHS} = 220 W/m K.

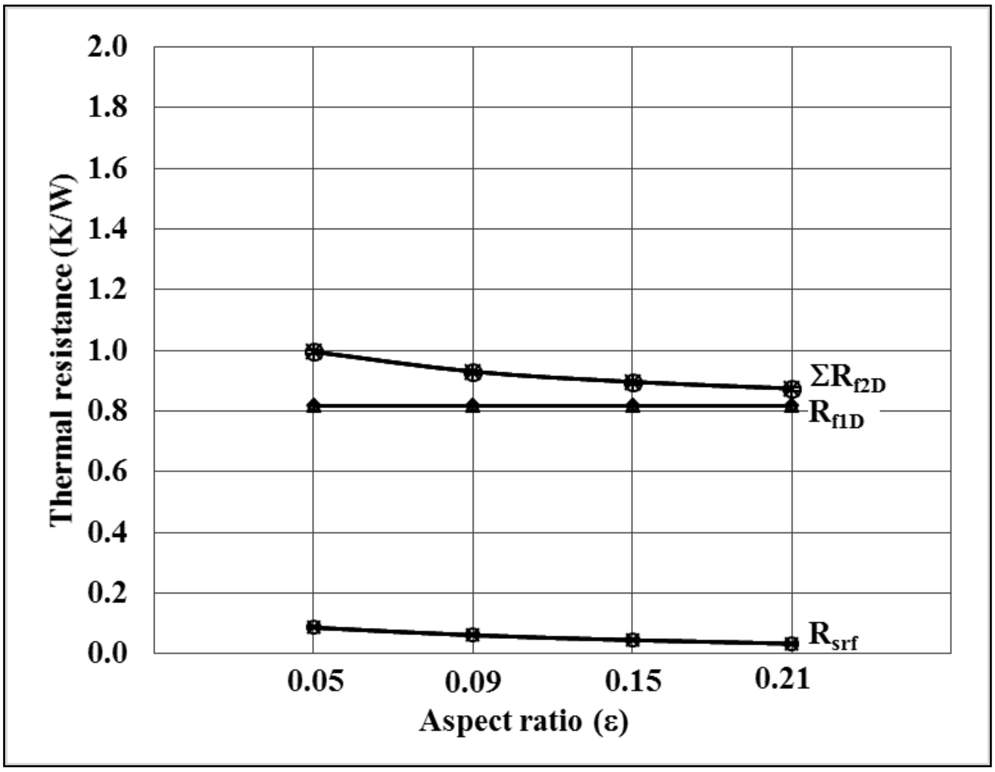

Figure 3.12 CFD simulation showing effect of aspect ratio ε with P_{EH} = 100 W, h_a = 10 W/m^2 K and k_{FHS} = 220 W/m K.

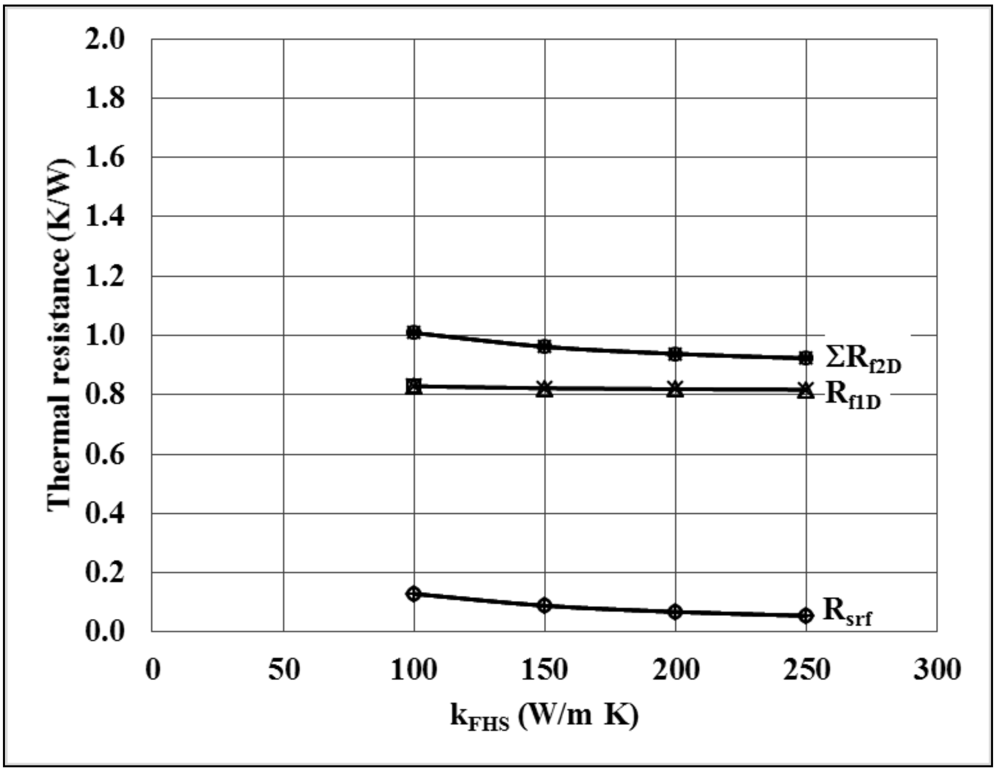

Figure 3.13 CFD simulation showing effect of thermal conductivity k_{FHS} with P_{EH} = 100 W, ε = 0.09 and h_a = 10 W/m^2 K.

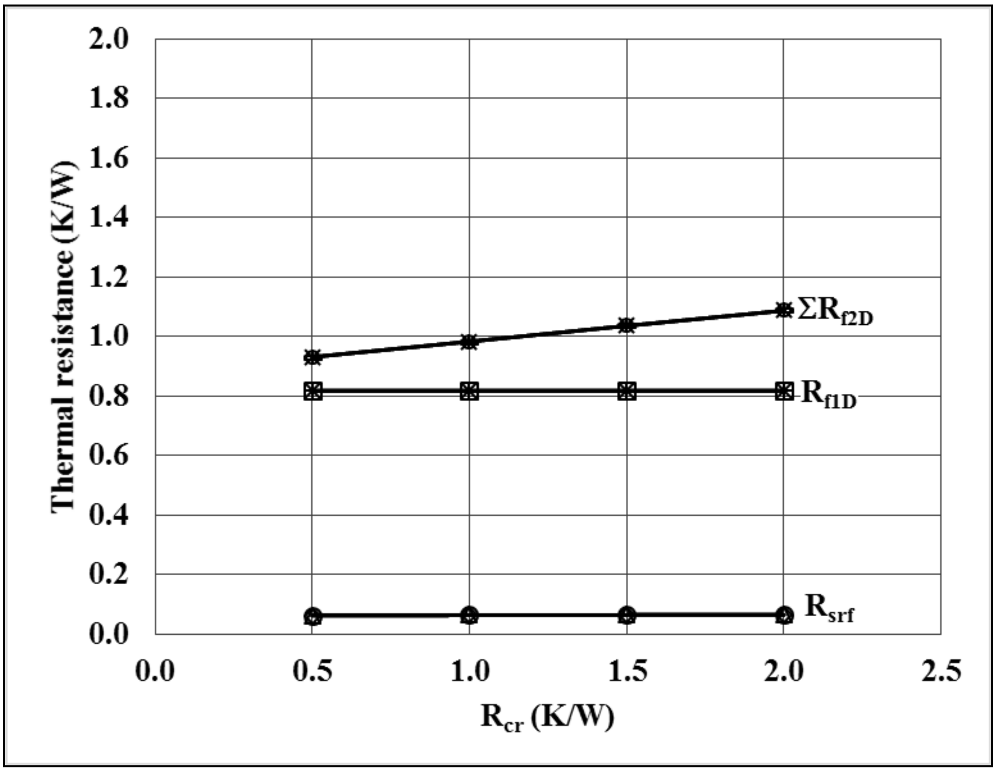

Figure 3.14 CFD simulation showing effect of contact resistance R_{cr} with P_{EH} = 100 W, ε = 0.09, h_a = 10 W/m^2 K and k_{FHS} = 220 W/m K.

3.4 Comparison between experimental and CFD simulated temperature results

A CFD simulation was performed in order to obtain simulated results for the mean base (T_{fm}) and max (T_{fmax}) temperatures and to compare them against the experimental results obtained from Runs B1 to B3 for FHS#2 under NC. Since the experimental heat loss was found to be less than 1%, it was assumed negligible in the CFD simulation. Experimental values of ambient temperature (T_a) and heat transfer coefficient (h_a) values from Equation (2.20) were input into the CFD software package to obtain simulation temperatures for FHS#2. The CFD simulated and experimental temperatures for FHS#2 under NC are tabulated in Table 3 and compared in Figure 3.15. In general, temperatures T_{fmax} and T_{fm} increase with input heat power. A comparison of the experimental temperature values with the CFD simulated results shows that agreement was not good. Predicted temperatures were about half that obtained experimentally. A possible explanation could be found from the assumed value of the heat transfer coefficient. Table 3 shows 2 sets of simulated temperature results. The first set was obtained by inputting the values of h_a previously derived from Equation 2.20 (see Figure 2.13) obtained from FHS#1 under NC. The second set was obtained by reducing the values of h_a as input into the CFD program. A comparison of this set of simulated results show very good agreement was obtained between experimental and simulated results, Figure 3.16. Hence this brings us to the conclusion that the heat transfer coefficient for FHS#2 under NC air cooling with 2-dimensional heat spreading effect could be much smaller than the 1-dimensional heat transfer coefficients obtained without heat spreading effect. Further investigations would need to be conducted to verify this.

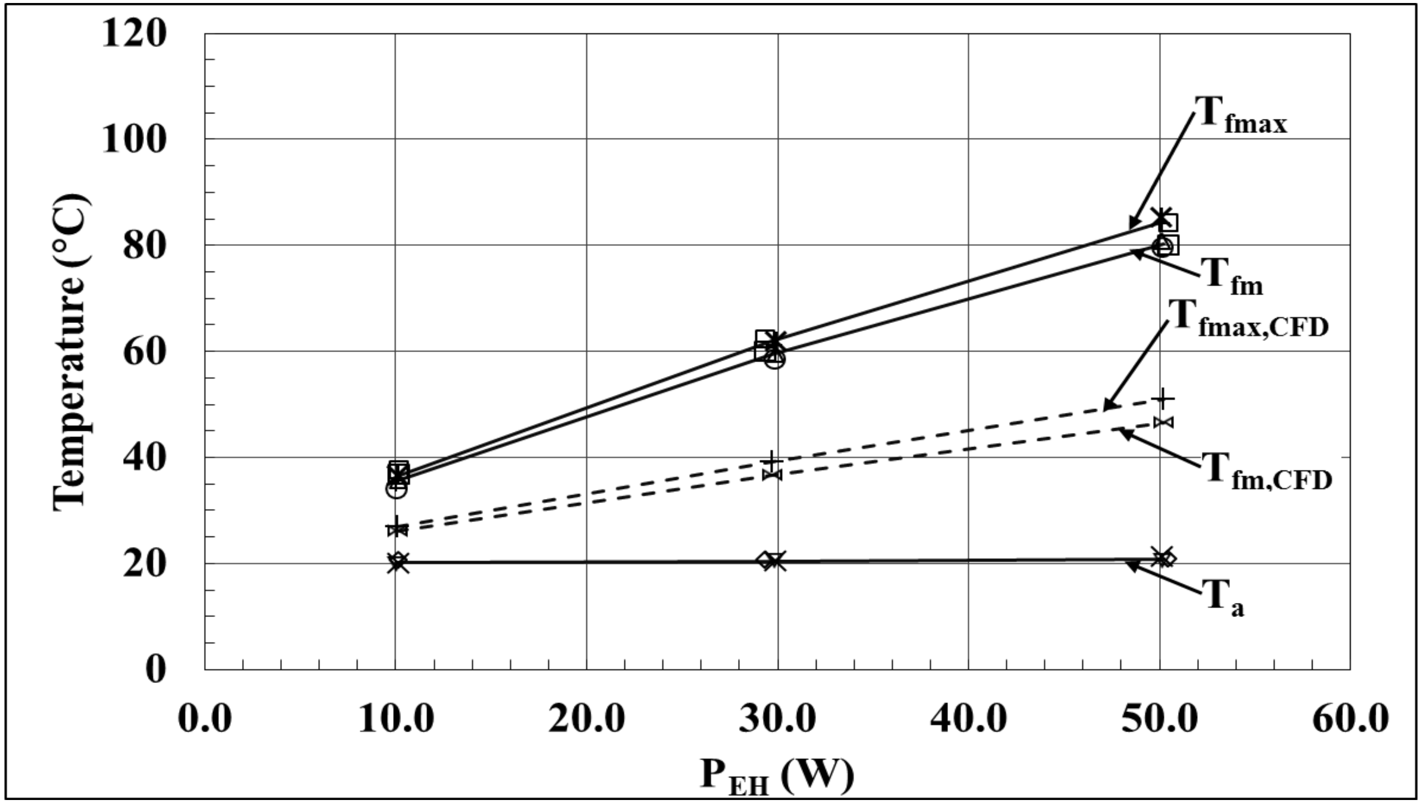

Figure 3.15 Comparison of experimental and CFD simulation temperatures for FHS#2 (Runs B1-B3).

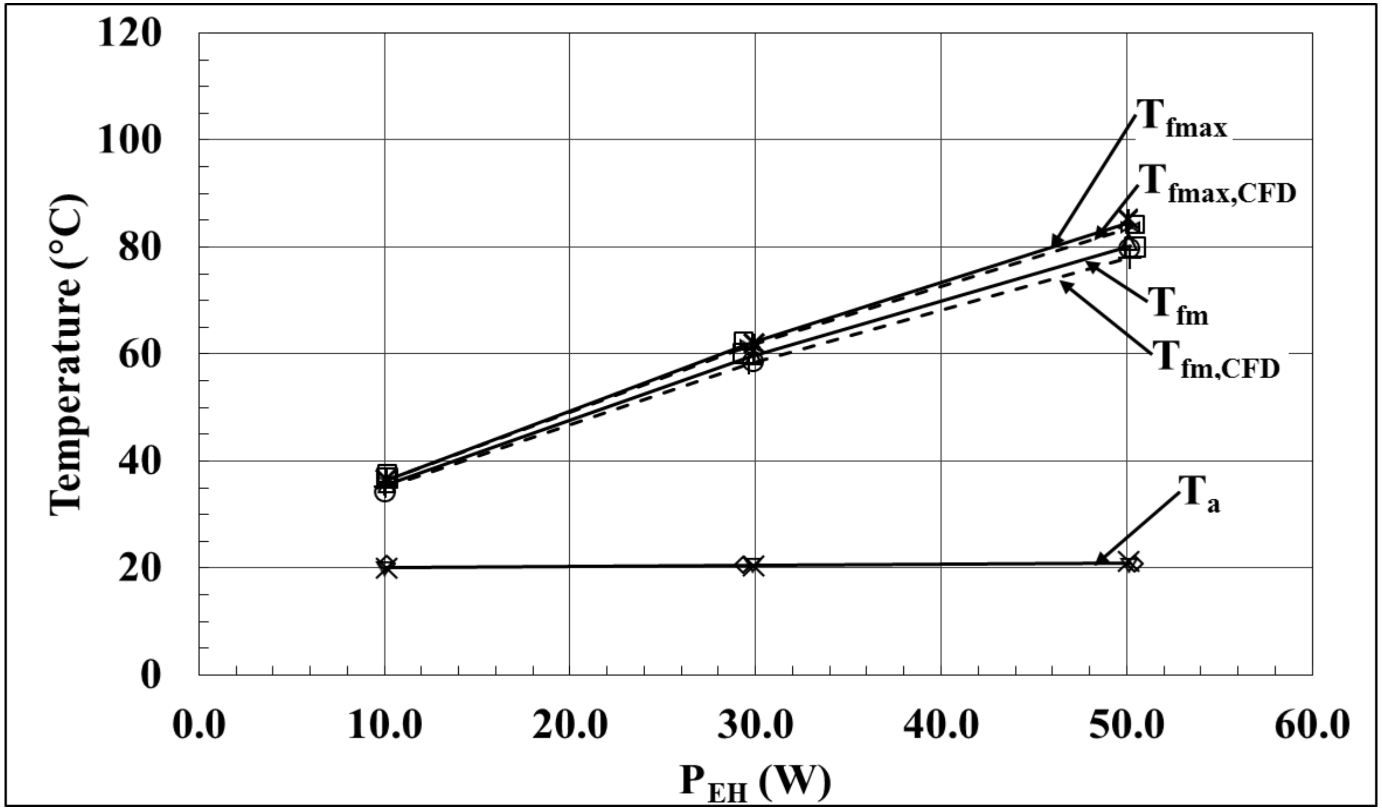

Figure 3.16 Comparison of experimental and CFD simulation temperatures for FHS#2 (Runs B1-B3) with modified h_a.

3.5 Chapter conclusions

In this chapter, the effect of five parameters, viz., power input, thermal conductivity, aspect ratio, heat transfer coefficient and thermal contact resistance on the performance of the FHS were simulated using a CFD software package. Thermal heat spreading and contact resistances were small compared to the thermal resistance of the FHS itself. The temperature at the base of the FHS and the maximum temperature obtained experimentally were compared to simulated values. The results showed that the heat transfer coefficient under 2-D heat flow was lower due to thermal heat spreading. Further investigations would need to be conducted to determine actual values.

CHAPTER 4

FIN HEAT SINK – VAPOUR CHAMBER ASSEMBLY

4.1 Literature survey

Attia and EI-Assal (2012) investigated the thermal performance of a VC with 50 mm inner diameter and 2 mm thick. Various working fluids with fill ratios of 0.1 to 0.6 were used. The working fluids were water, methyl alcohol, mixture of water +15% propylene glycol and mixture of water + 50% propylene glycol. A 50 mm diameter and 2.5 mm thick electric heater was used to provide a heat source up to 150 W. The results showed water as working fluid is more efficient than methyl alcohol. Charge ratio of 0.3 was considered best for the working fluids tested.

Chen et al. (2008) presented a numerical simulation of thermal performance of VC using isotropic and orthotropic approaches. The VC measured 86 mm × 71 mm with thickness of 5 mm. The results showed thermal spreading resistance at the interface between VC and heat source contributed most to the overall thermal resistance of the VC. They suggested that the orthotropic approach was a better way to calculate the heat transfer characteristics.

Chen et al. (2006) proposed a model to estimate the thermal performance of a VC without having to solve complex two-phase flow. In their calculations, the convection thermal resistance of the working fluid was assumed negligible. The thermal resistance from the theoretical model was 8.6% lower than the average experimental results.

Connors and Zunner (2009) studied the applications of VC and heat pipe for cooling military embedded electronic devices. They evaluated cooling performances of aluminium and copper heat pipe embedded frames on electronic devices. Their results also showed that the VC had the lowest thermal resistance. The aluminium plate had the highest thermal resistance amongst four tested samples.

Lin et al. (2011) investigated the thermal performance of VC with 1 W to 5 W power input under natural convection and up to 40 W under forced convection. The VC measured 50 mm × 50 mm and 3.5 mm thick. Their results showed that the thermal resistance of the VC increased with thickness of chamber.

Peng et al. (2013) studied the thermal performance of an aluminium VC measuring 80 mm × 75 mm × 15 mm with a fin heat sink mounted on the top. The VC was filled with distilled water or acetone as working fluid with fill ratio from 0.1 – 0.5. The system was heated up to 100 W. They concluded that the maximum surface temperature of the heater was lower than 60 °C at 100 W power input. They also showed acetone performed better than water as working fluid.

Tsai et al. (2013) presented experimental studies of heat spreading thermal resistance of a VC measuring 90 mm × 90 mm × 3.5 mm. A water-cooled copper jacket was used to remove the heat. They evaluated the thermal performance of the VC at several inclinations and showed that thermal resistance decreased as power input increased. They also found that the greatest thermal resistance was 0.89^{o}C/W at 50 W with the VC inclined at 90$^{o.}$

Luo et al. (2010) determined the cooling performance of a FHS-VC assembly. They used a 20 W LED module as heat source and a copper VC with 120 mm outer radius. The VC was filled with acetone liquid as working fluid. Copper screen mesh was used as wick structure. The results showed that the temperature at the bottom of the VC was uniform to within 0.16^{o}C indicating the heat spreading effectiveness of the assembly.

Huang et al. (2012) carried out an experiment on the effect of vapour space height in a VC measuring 110 mm × 50 mm. Several thicknesses of VC were tested from 0.4 mm to 1.2 mm with increment of 0.2 mm. The VC was heated up to 240 W and cooled with a water jacket. They found that the height of vapour space in the vapour chamber had a significant effect - temperature and thermal resistance decreased with larger space.

Chen et al. (2013) investigated the effect of a wick structure in a VC. Two similar sized VCs measuring 58 mm × 58 mm × 6 mm were fabricated and tested. The VCs were made of aluminium and filled with acetone as working fluid. Radial grooved and sintered power wick structures were provided in the VCs. Experiments were conducted with various fill ratios from 0.25 – 0.70 and power inputs from 20 W to 80 W. The results showed that the VC with sintered power wick resulted in lower temperature than radial grooved wick at all tested power input. Besides, more temperature uniformity was obtained with the sintered power wick VC compared to the radial grooved wick. They concluded that cost and performance are the main criteria for selecting wick design. Radial grooved wick is easier and cheaper to fabricate. On the other hand, sintered wick performed better.

Wang (2011) compared the thermal performances of solid copper and aluminium heat spreaders with a VC. They found that the aluminium heat spreader had the highest thermal resistance at all power inputs. The VC performed best with power input above 5 W. The copper heat spreader performed better than the VC at power input less than 5 W.

Boukhanouf et al. (2006) studied the thermal performance of a VC using a thermal imaging camera. The water-filled copper VC measured 250 mm × 200 mm × 5 mm thick. The inner wall of the VC had a sintered copper wick structure. An aluminium FHS was placed on top of the VC for heat dissipation. An IR image camera mounted on a tripod stand captured the thermal image. The results showed that a solid copper block and defective VC exhibited large temperature gradients but a fully functioning VC showed excellent heat spreading. They concluded that the IR camera imaging technique could be used to evaluate VC performance.

Zhang et al. (2009) investigated the effect of heat flux, fill ratio and gravity on a VC with grooved wick structure. A grooved 85 mm diameter and 9 mm thick VC filled with water was tested. The results showed that the optimal fill ratio was 0.4 when heat flux was 3.05×10^5 W/m^2. They also showed that the VC improved the thermal heat spreading performance compared to that of a copper plate with the same dimensions.

4.2 Theoretical model and thermal resistance network

A thermal resistance model of a FHS–VC assembly is shown in Figure 4.1(a). A simple thermal resistance network is presented in Figure 4.1(b). An aluminium block is located in between the heating element and the FHS. It is to ensure that the heat transfer from the heating element is distributed evenly. Thermal contact resistances (R_{cr2} and R_{cr3}) are assumed to be present at the indicated interfaces. The surface temperature (T_{vctop}) at the top of the VC is assumed uniform. Thermal heat spreading occurs at the interface between the bottom of the VC and the top of the aluminium block. Hence, maximum temperature (T_{vcmax}) and mean temperature (T_{vcbot}) appear at the bottom surface of the VC. The following are the equations used in this section for evaluating the performance of the FHS-VC assembly.

The thermal contact resistances are given by

$$R_{cr2} = \frac{(T_{alm} - T_{vcmax})}{P_{EH}} \tag{4.1}$$

and

$$R_{cr3} = \frac{(T_{vctop} - T_{fm})}{P_{EH}} \tag{4.2}$$

The thermal heat spreading resistance of the VC is determined from

$$R_{srvc} = \frac{(T_{vcmax} - T_{vcm})}{P_{EH}} \tag{4.3}$$

and the thermal resistance of the VC itself is

$$R_{vc} = \frac{(T_{vcbot} - T_{vctop})}{P_{EH}} \tag{4.4}$$

The overall thermal resistance of the FHS-VC assembly can be expressed as

$$\Sigma R_{fvc} = R_{cr2} + R_{srvc} + R_{vc} + R_{cr3} + R_{f1D} \tag{4.5}$$

or

$$\Sigma R_{fvc} = \frac{(T_{alm} - T_{a})}{P_{EH}} \tag{4.6}$$

A cross-sectional view of a VC with a wick structure over the internal wall is shown in Figure 4.2(a) and the equivalent thermal resistance network shown in Figure 4.2(b). The theoretical thermal resistance of VC is calculated individually as equations below, Thermal resistance of the wall of VC

$$R_{wall} = \frac{\Delta x_{vc}}{k_{wall}\ A_{vc}} \qquad (4.7)$$

Thermal resistance of wick of VC

$$R_{wick} = \frac{\Delta x_{wick}}{k_{wick}\ A_{vc}} \qquad (4.8)$$

Thermal resistance of VC at evaporator

$$R_{evap} = \frac{1}{h_{evap}\ A_{vc}} \qquad (4.9)$$

Thermal resistance of VC at condenser

$$R_{cond} = \frac{1}{h_{cond}\ A_{vc}} \qquad (4.10)$$

The theoretical total thermal resistance of the VC is given by

$$R_{vc} = 2\,R_{wall} + R_{wick} + R_{evap} + R_{cond} \qquad (4.11)$$

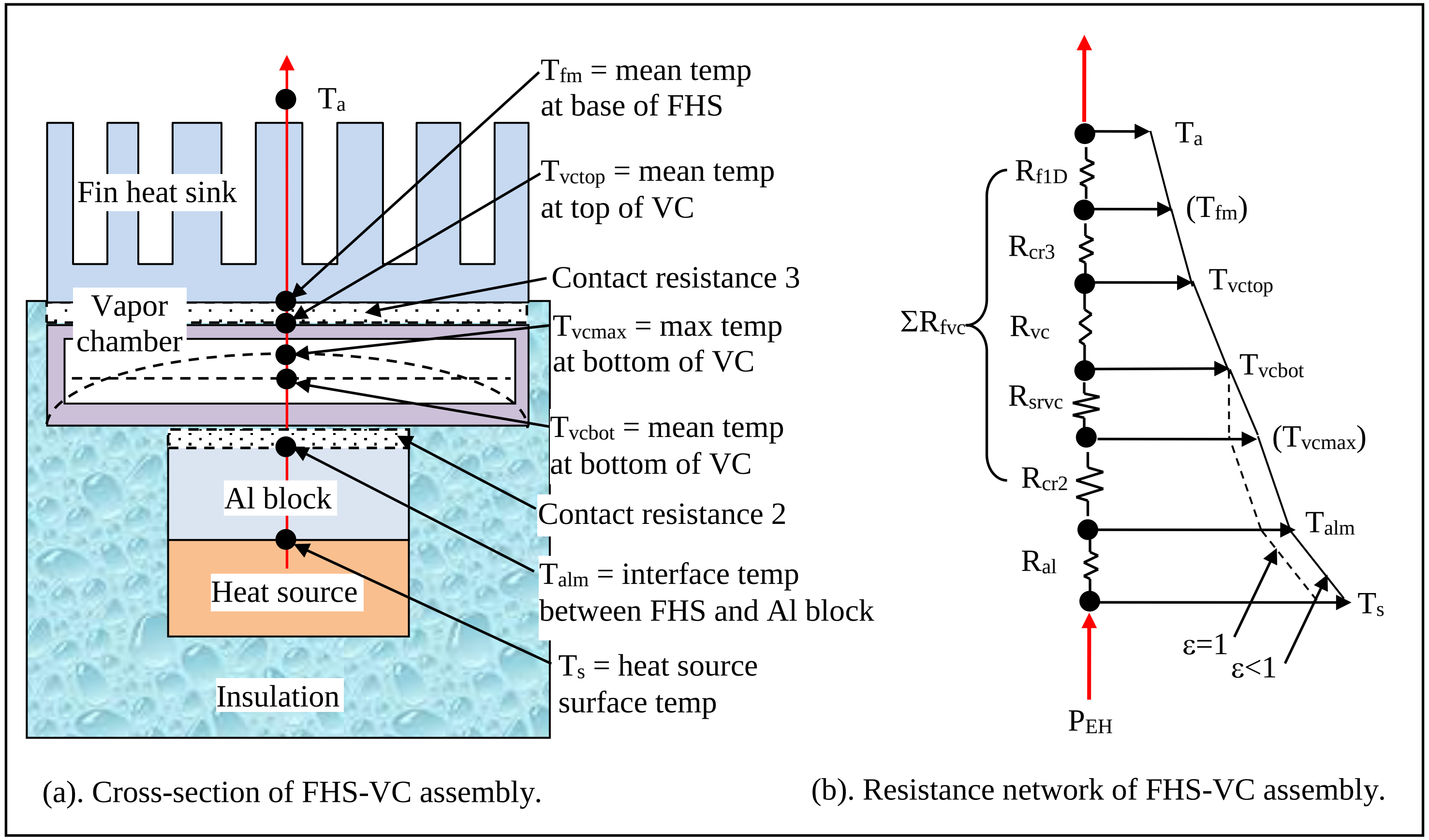

Figure 4.1 Thermal resistance network of FHS-VC assembly.

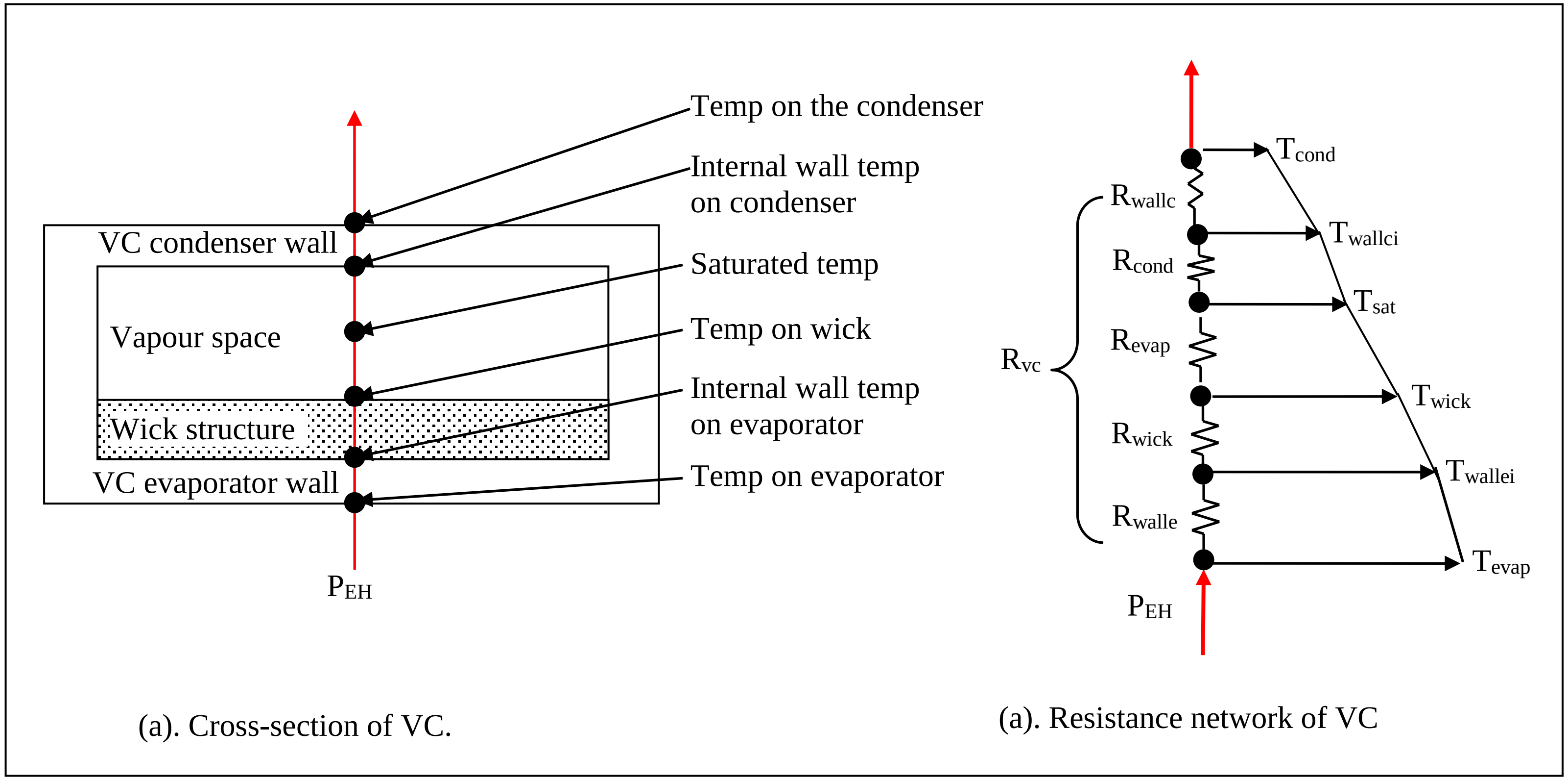

Figure 4.2 Thermal resistance network of VC.

4.3 Experimental investigation

4.3.1 Experimental apparatus

An experimental investigation was carried out to determine the thermal performance of a FHS-VC assembly. The experimental setup is shown in Figure 4.3. The copper VC measured 137 mm × 123 mm with thickness of 3 mm. It was supplied by Fujikura of Japan and contained a sintered wick internally. The thickness of the wick is about 0.4 mm. The VC is filled with water at fill ratio of 20%. The wall of the VC is 0.8 mm thick. The FHS employed here is the FHS#2 previously used. Figure 4.4 shows a photograph of the VC. An aluminium block and an ac-powered electric heating element were located in between the VC and the heating element. The heating element measured 30 mm × 30 mm × 4 mm thick and the aluminium block measured 30 mm × 30 mm × 22 mm thick. Power input to the heating element (P_{EH}) was determined from ac voltmeter and ammeter connected to the ac power supply from a variable ac voltage regulator. The aspect ratio of size of heating element/size of VC (ε) was 0.053. Thermal heat spreading effect is expected at the bottom of the VC. Type T copper-constantan thermocouples were used to measure temperatures. Twenty one thermocouples (T_{f1} – T_{f21}) were inserted into the FHS#2 through holes drilled into it. The locations of these the thermocouples are as shown in Figure 2.6. The mean surface temperature on the top of the VC (T_{vctop}) was calculated from the arithmetic average of these twenty one thermocouples. The mean surface temperature of the top surface of the aluminium block (T_{alm}) was determined from the arithmetic mean of four thermocouples (T_{al1} – T_{al4}). These four thermocouples were inserted into grooves machined on the top surface of the aluminium block. Fifteen thermocouples (T_{vc1} – T_{vc15}) were inserted through the bottom of the thermal insulation to measure the temperatures at the bottom surface of the VC. Location of the probe points of these thermocouples on the bottom surface of the VC is shown in Figure 4.5. The maximum temperature at the bottom of the VC (T_{vcmax}) was assumed to be equal to T_{alm}. Ambient temperature (T_a) and insulation temperature (T_{ins}) were measured by other thermocouples. The thermocouples were data logged every minute.

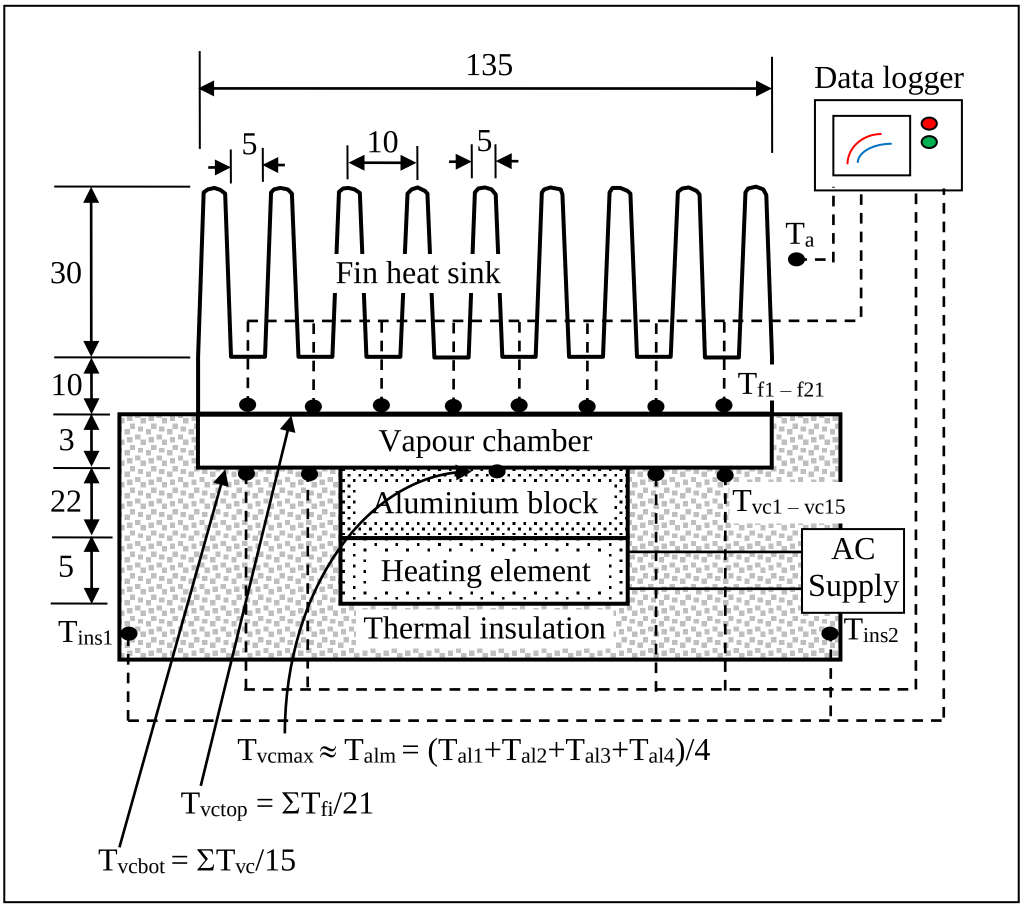

Figure 4.3 Experimental set-up to determine thermal performance of the FHS-VC assembly.

Figure 4.4 Photograph of VC.

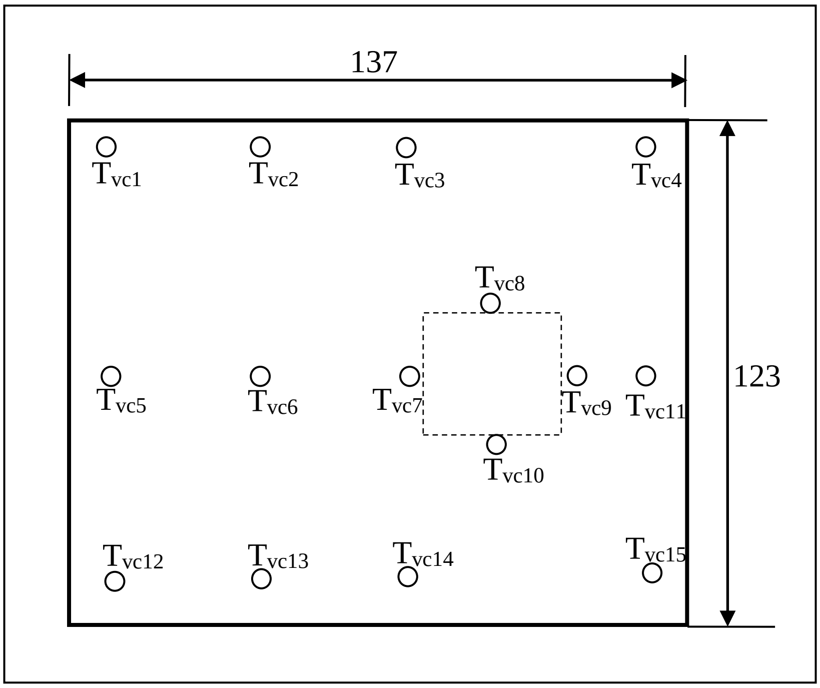

Figure 4.5 Locations of thermocouples on bottom surface of VC.

4.3.2 Experimental procedure

The thermal performance of the FHS-VC assembly under NC air cooling was determined at various power inputs (P_{EH}) to the heating element from 10 W, 30 W and 50 W. The experiment was repeated three times at each setting to determine the experimental repeatability. Each run was conducted over six hours in order to obtain steady state. Thermal resistances (R_{f1D} + R_{cr3}), R_{vc}, (R_{cr2} + R_{srvc}) and the overall thermal resistance of the FHS-VC assembly (ΣR_{fvc}) are calculated and tabulated in Table 4. (Runs C1 – C3).

4.3.3 Experimental results

Figure 4.6 shows transient temperatures for the FHS-VC assembly (Runs C1 to C3). The temperature distribution along the centreline of FHS-VC assembly is shown in Figure 4.7. The temperatures and thermal resistances are plotted against power input in Figures 4.8 and 4.9, respectively. Figure 4.10 compares the experimental results of the FHS#2 with and without the VC.

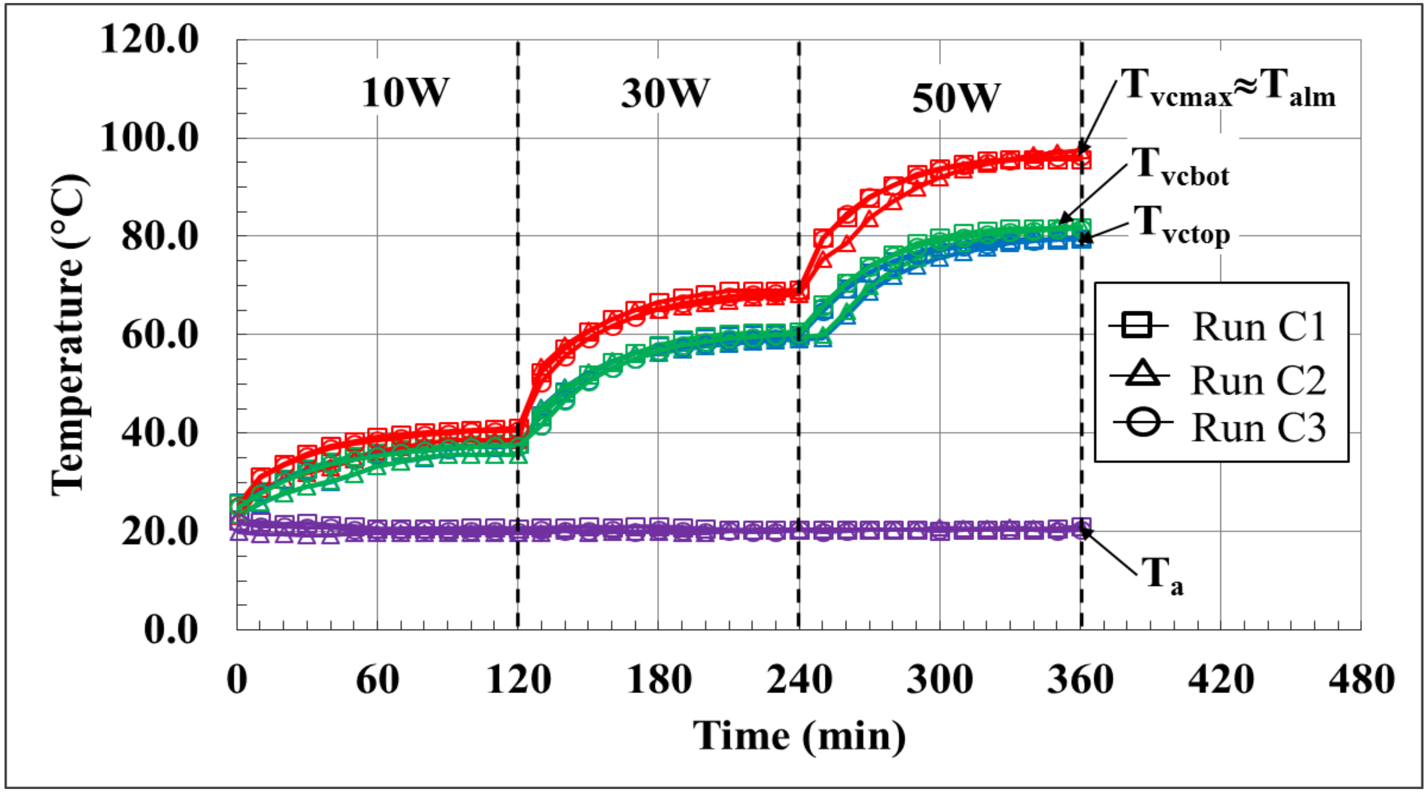

Figure 4.6 Transient temperatures for FHS-VC assembly (Runs C1 – C3).

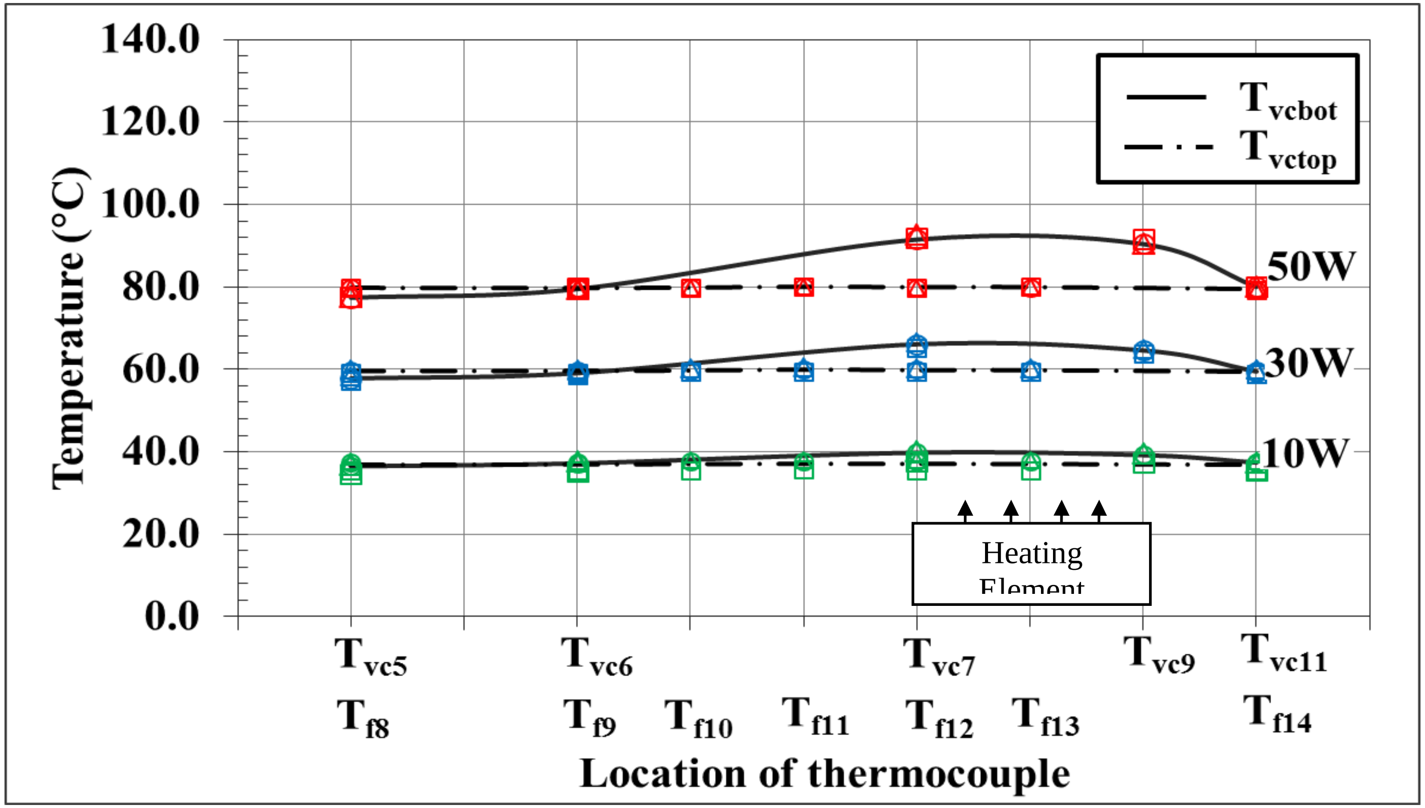

Figure 4.7 Temperature distribution along centreline of FHS-VC assembly (Runs C1 – C3).

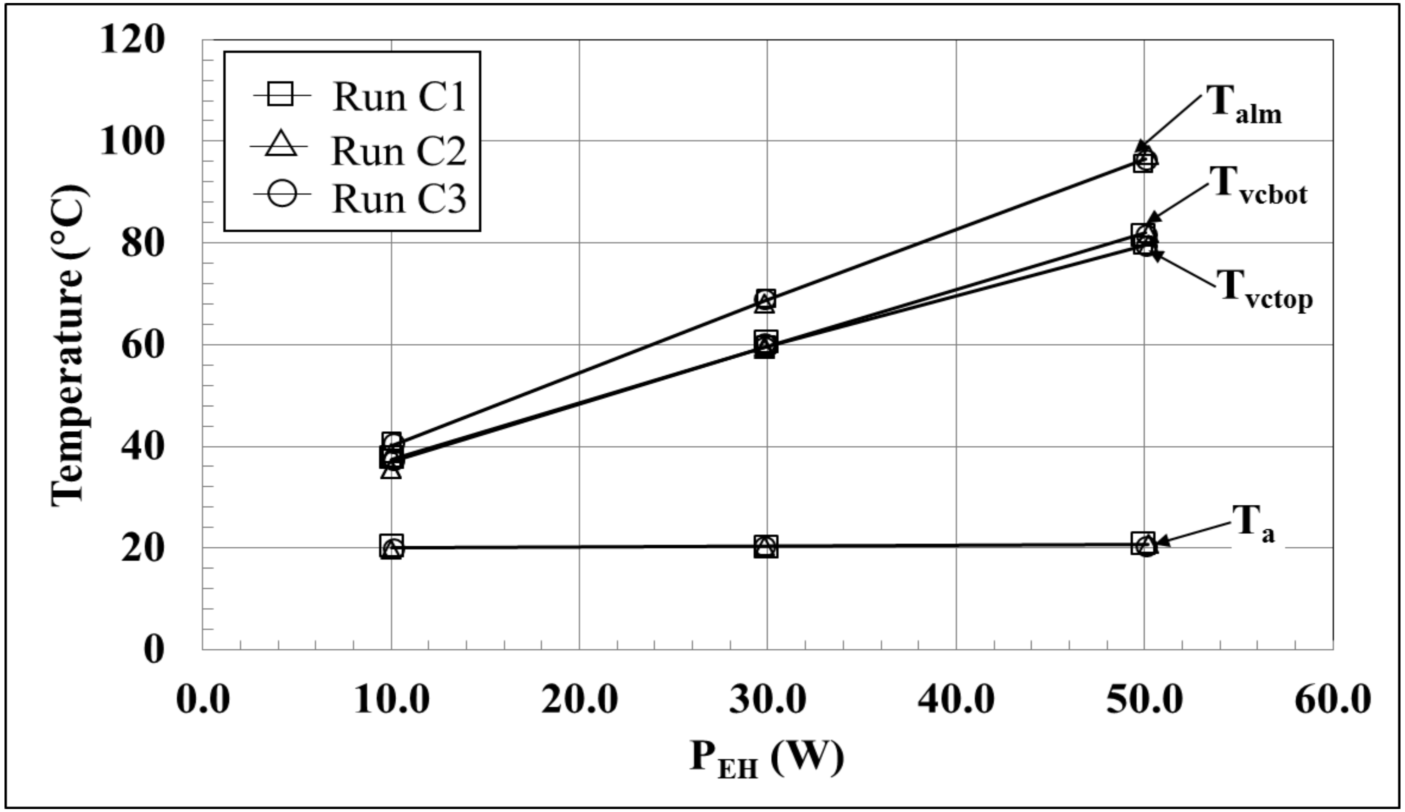

Figure 4.8 Temperature variation with power input (Runs C1-C3).

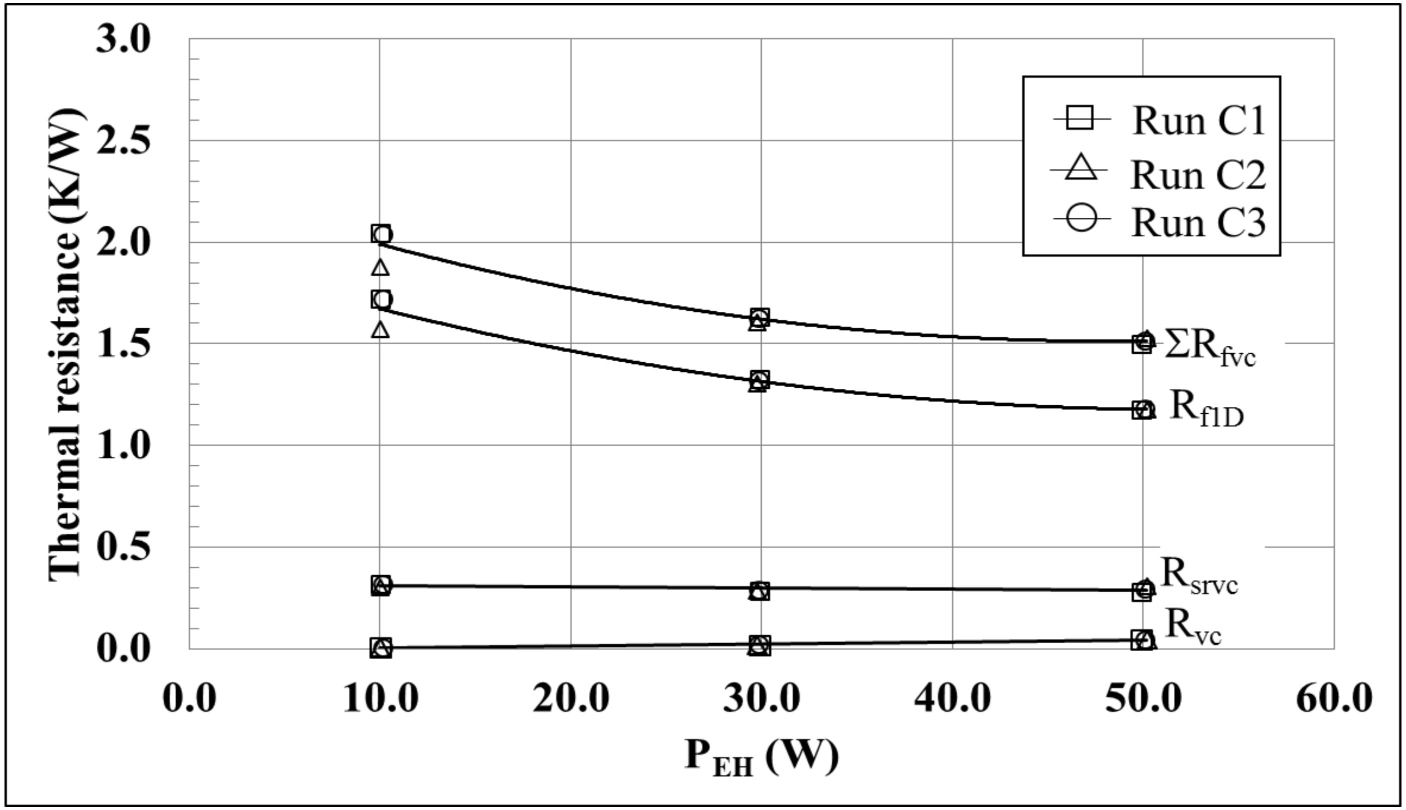

Figure 4.9 Thermal resistance variation with power input (Runs C1-C3).

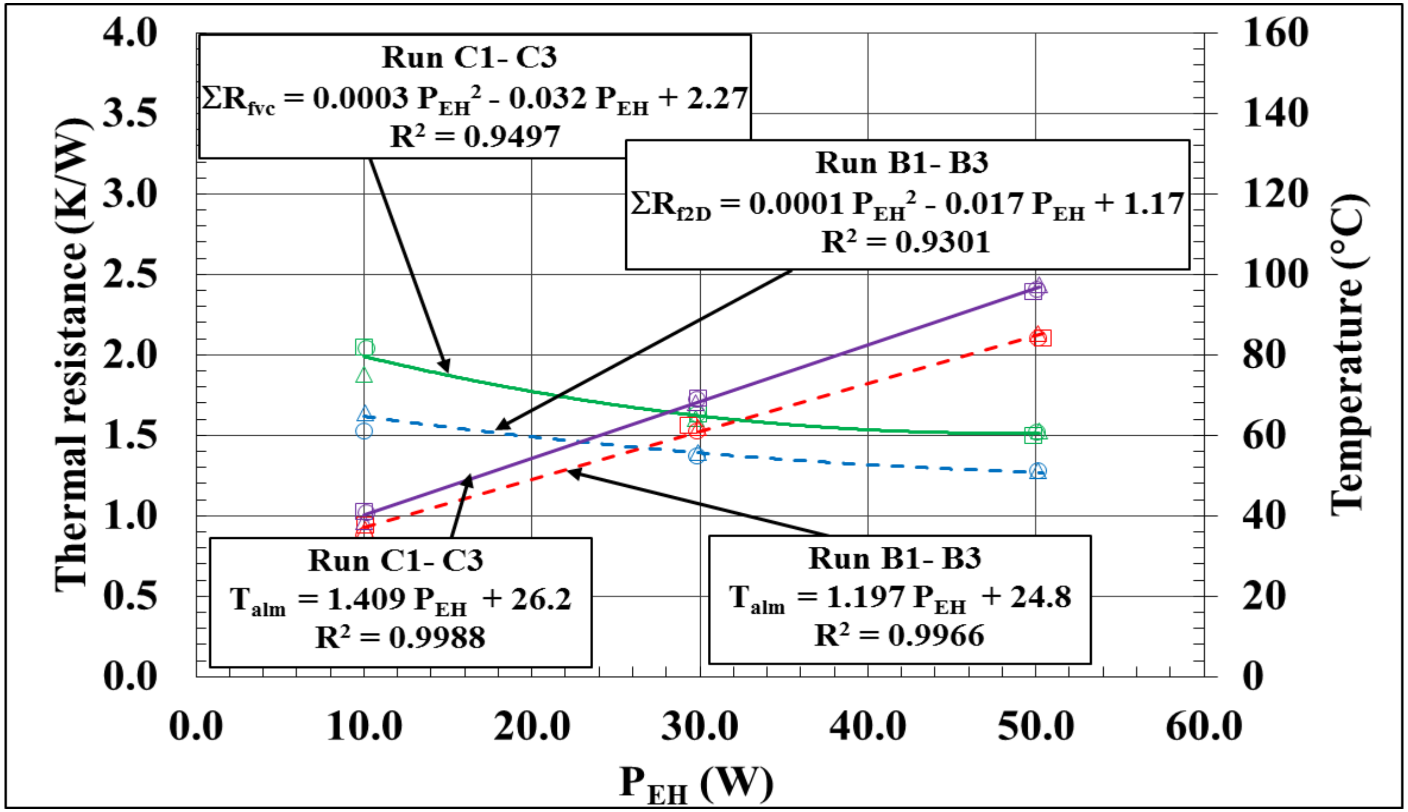

Figure 4.10 Comparison of experimental results between FHS#2 with and without VC.

4.4 Discussion of results

4.4.1 Repeatability of experiment

Mean temperatures of top (T_{vctop}), bottom (T_{vcbot}) and maximum at the bottom of the VC (T_{vcmax}) for the FHS-VC assembly plotted in Figure 4.6 for Runs C1 to Run C3 show that steady state was achieved after about 120 min. Ambient temperature was not controlled and varied from 19.8°C to 21.0°C. From the insulation temperature results, heat loss from the sides accounted for about 2% at the low power input to less than 0.2% at the higher power input. Overall, the results were repeatable to within 3°C.

4.4.2 Temperature distribution

The heating element was not located in the middle of the VC. It was slightly displaced towards one side due to the pre-made pedestal on the VC by the manufacturer as seen in Figure 4.5. The centreline temperature distribution at both top and bottom surfaces of the VC assembly are shown in Figure 4.7 for all three power inputs. The temperatures obtained at the various input power heat fluxes are shown in Figure 4.8. The following results can be seen:

- Figure 4.7 shows that surface temperature at the top of VC (T_{vctop}) was quite uniform, varying by less than 1°C with power input ranging from

10 W – 50 W showing the effectiveness of the VC to spread the heat evenly.

- Figure 4.7 shows that the temperature at the bottom of the VC (T_{vcbot}) was not uniform, showing the effect of thermal heat spreading effect.
- Thermal heat spreading increased with power input, with temperature varying from 2^{o}C at low power to 9^{o}C at high power.
- Figure 4.8 shows that both top and bottom surface temperatures increase with power input.

4.4.3 Thermal resistance

Experimental thermal heat spreading (R_{srvc}) and other thermal heat resistances (R_{vc}, R_{f1D} and ΣR_{fvc}) are tabulated in Table 4. The effect of power input (P_{EH}) on these thermal heat resistances is shown in Figure 4.9. The thermal heat spreading resistance at the bottom of the VC including the thermal contact resistance (R_{srvc} + R_{cr2}) is near uniform and small, about 0.3 - 0.4 K/W. The thermal resistance of the VC (R_{vc}) is also near uniform and very small, about 0.01 – 0.04 K/W. One-dimensional fin and thermal contact resistance (R_{f1D} + R_{cr3}) decrease with power input and varies from 1.17 – 1.72 K/W. Total thermal heat resistance of the FHS-VC assembly (ΣR_{fvc}) decrease with power input and varies from 1.50 - 2.05 K/W. This shows that thermal fin resistance (R_{f1D}) was very much higher than the VC (R_{vc}) and heat spreading (R_{srvc}) resistances. It should be pointed out here that the experimental temperature difference between top and bottom surfaces of the VC is very small, of the order of 0.1 – 2.2ºC. Hence the thermal resistance (R_{vc}) is not very accurate especially at low power. A theoretical value was calculated using evaporator (h_{evap}) and condensing heat (h_{cond}) transfer coefficients equal to 600 and 8000 W/m^2 K, respectively obtained from Christopher Lim (2014). The theoretical thermal resistance of the VC calculated from Equation (4.7) to (4.11) is about 0.11 K/W. A comparison with the experimental value of 0.01 K/W would seem to indicate poor agreement. However, the experimental value is not very accurate, as mentioned. The fin resistance (R_{f1D}) is seen to be much greater than the VC thermal resistance (R_{vc}).

4.4.4 Comparison of performance of FHS with and without the VC

Experimental results obtained with the FHS#2 alone (Runs B1 to B3) and with the VC (Runs C1 to C3) are compared in Figure 4.10. The surface temperature of the aluminium block (T_{alm}) and total thermal resistance of the system (ΣR_{f2D}) are plotted against input power from 10 W to 50 W. The surface temperature increased with power input while the total resistance decreased. The results show that both surface temperature and total thermal resistance obtained the FHS-VC assembly were higher than those obtained by FHS alone. This shows that the incorporation of the VC with the FHS#2 performed worse than using the FHS#2 alone. Hence in this instance, there is no advantage to use the VC for heat spreading. A possible explanation is that the additional thermal resistances created by the additional contact surfaces and the VC itself were greater than the heat spreading resistance.

4.5 Chapter conclusions

The thermal performance of a FHS–VC assembly was investigated. The results showed that thermal heat spreading occurred at the bottom surface of the VC. The heat spreading effect increased with power input. The temperature distribution at the top surface of the VC was uniform. The cooling performance of the present FHS-VC assembly was not as good as that obtained using the FHS alone. This was attributed to the additional thermal contact resistances between the VC and the aluminium block and between the VC and the FHS. An improved design with hollow finned vapour chamber is recommended for future studies.

CHAPTER 5

FIN HEAT SINK – THERMOELETRIC ASSEMBLY

5.1 Literature survey

Hasan and Toh (2007) investigated a system consisting of thermoelectric cooler (TEC) with a fan cooled heat sink. They presented a method to characterize the TEC and compared the cooling performance of the FHS-TE assembly with a FHS only system. Under specific conditions, the FHS-TE cooling system performed better than FHS only system in terms of heat source temperature.

Chein and Huang (2004) presented a method to calculate the maximum cooling capacity of TEC. They showed that the cooling capacity increased when cold side temperature of TEC increased and temperature difference between hot and cold side of TEC was reduced. They suggested using water-cooled micro-channel heat sinks with the TE modules.

Bierschenk and Johnson (2004) outlined a design procedure to determine the optimum performance of TEC. The designed TECs allowed the use of smaller sized heat sinks for dissipating the same amount of heat and allowing more heat dissipation for same sized heat sinks when the temperature difference between the base of the heat sink and ambient was maintained below 25 °C.

Taylor and Solbrekken (2006) compared the performance of an optimally configured TEC enhanced system with heat sink only system. They found the TEC enhanced system produced lower junction temperatures only at low heat loads. Two current optimization equations and geometry equations were thus deduced. The results demonstrated that the system performance was heavily dependent on TE design and operation conditions.

Chang et al. (2009) studied the thermoelectric cooling device applied to the cooling of electronic devices. Their results showed that the thermal performance of thermoelectric cooler reduced the heat from the devices at low power heat load. Wang et al. (2015) presented a novel cooling model and evaluated its thermal performance for headlamp applications. They found that the optimal TEC input current of the TEC system with air cooling and liquid cooling were 3.0 A and 5.0 A, respectively, when the LED worked at a nominal current (1000mA). The junction temperature was calculated as 59.5°C.

Zhang (2010) presented a concise and simple practical design to evaluate and optimize TEC. He developed a new method to strengthen the analysis approach, and examined the optimization of device temperature for microprocessors under TEC enhanced air cooling and liquid cooling conditions. Zhong et al. (2010) investigated three different TEC systems and determined the optimal current of TEC at different heat source power ranging from 10W to 50W.

Chein and Chen (2005) employed microchannel heat sinks fabricated with etched silicon wafers on the hot side of TEC to dissipate heat. They showed the thermal resistance of heat sink played an important role to reduce the temperature of heat source when current input to TEC increased. High electric current input to TEC resulted in no cooling effect when a high thermal resistance heat sink was used.

Wang et al. (2009) investigated thermal management of LED packaging with TEC system under natural convection. They managed to reduce the junction temperature of the LED to about 40°C when LED power was below 8W and confirmed that TEC performed better with heat sink.

Kaushik et al. (2015) investigated the TEC system through exergy analysis. They provided a complete detail~~s~~ about exergy efficiency and irreversibility in TEC system. They showed the exergy efficiency of TEC increases with increased with temperature on hot side.

Qian and Ren (2016) studied the cooling performance of transverse TEC. A transverse TEC is used to obtain a transverse heat flow from a longitudinal electrical current as Peltier effect. They examined the cooling performance of transverse TEC by using finite element analysis. Their results showed temperature variation in the cooling region is affected by thickness of material layer.

Wang et al. (2013) developed a theoretical model to optimize configuration of a TEC system based on entropy generation analysis method. The analysis indicated an optimum thermal conductance allocation ratio when the TEC system operated at maximum COP condition. They also showed the total thermal conductance had significant influences to the COP at highest cooling capacity condition (Q_{cmax}).

Zebarjadi (2015) mentioned that new TE materials are required to provide better cooling solutions than regular heat sinks. They proposed adding thermoelectric elements as fins attached to copper heat sink to significantly enhance the cooling performance.

5.2 Theoretical model and thermal resistance network

A theoretical model of a TE module incorporated with a FHS is shown in Figure 5.1(a). The associated thermal resistance network for the model is shown in Figure 5.1(b). Heat transfer across all the interface temperature are assumed to be uniform due to one-dimensional heat transfer assumed. The theoretical model is assumed to be perfectly insulated around the sides of the heating element and the TE module. Hence there is no heat loss from the system. The junction between the TE module and the heat source is designated as the cold side of the FHS-TE assembly. The junction between the TE module and the FHS is designated the hot side. Heat transfer rate at the cold side ($\dot{q}_c$) is assumed to be equal to the heat generated at the heating element (P_{EH}). Voltage (V_{te}) and current (I_{te}) supplied to the TE module creates a temperature difference (ΔT_{te}) between the top and bottom surfaces of the TE. Heat from the heat source cold side is dissipated to the ambient via the FHS.

The heat transfer rate at the cold side of the TE module is given by

$$\dot{q}_c = \alpha_{te}\ I_{te}\ T_c - \frac{I_{te}^2 R_{te}}{2} - K_{te}\ \Delta T_{te} \qquad (5.1)$$

and at the hot side by

$$\dot{q}_h = \alpha_{te}\ I_{te}\ T_h + \frac{I_{te}^2\ R_{te}}{2} - K_{te}\ \Delta T_{te} \qquad (5.2)$$

The temperature difference across the TE module is

$$\Delta T_{te} = T_h - T_c \qquad (5.3)$$

An energy balance gives the power to be supplied to the TE module

$$P_{te} = \dot{q}_h - \dot{q}_c = \alpha_{te}\ I_{te} \Delta T_{te} + I_{te}^2\ R_{te} \qquad (5.4)$$

The applied TE voltage is

$$V_{te} = \alpha_{te}\ \Delta T_{te} + I_{te}\ R_{te} \qquad (5.5)$$

From the resistance network

$$\dot{q}_h = \frac{T_h - T_a}{R_{f1D} + R_{cr5}} \tag{5.6}$$

and

$$\dot{q}_c = \frac{T_s - T_c}{R_{al} + R_{cr4}} \tag{5.7}$$

The cooling coefficient of performance of the TE is

$$COP_c = \frac{\dot{q}_c}{P_{te}} \tag{5.8}$$

Usually, the thermal contact resistance R_{cr4} and R_{cr5} are small and calculated by Equation. 2.8. Hence, it could be neglected.

TE properties are obtained from the manufacturer. The internal electrical resistance of the TE module is a function of TE mean temperature (T_{mte}) and could be represented by

$$R_{te} = a + bT_{mte} \tag{5.9}$$

where mean TE temperature

$$T_{mte} = \frac{(T_h + T_c)}{2} \tag{5.10}$$

From the above it can be shown that

$$T_h = \frac{R_{f1D}\,(-b\,I_{te}^2\,T_c - 2\,a\,I_{te}^2 - 4\,K_{te}\,T_c) - 4\,T_a}{R_{f1D}\,(b\,I_{te}^2 + 4\,\alpha_{te}\,I_{te} - 4\,K_{te}) - 4} \qquad (5.11)$$

With specified values of cold surface temperature (T_c) and ambient temperature (T_a) together with the characteristics of the TE module, the hot side temperature ($T_{h,theory}$) could be predicted for a given TE current (I_{te}).

Figure 5.2 presents a procedure to calculate the TE hot side temperature ($T_{h,theory}$) from Equation. 5.11. As is presented in the flow chart, the first step of the process is to initialize the specified conditions of TE module such as ambient (T_a) and cold side temperatures and current applied (I_{te}). The characteristics of the TE module such as Seebeck coefficient (α_{te}), thermal conductance (K_{te}), internal electrical resistance (R_{te}), constants a and b for resistance are obtained from manufacturer's datasheet. These are given as α_{te} = 0.053 V/K, K_{te} = 0.66 W/K, R_{te} = 0.016 T_{mte} – 2.36, respectively. The procedure involves an iteration process. First, an approximate or guessed value of T_h. In this thesis, the guessed value is taken as equal to the measured experimental value to save time. Iterations are stopped if the difference between the predicted and assumed values are less than 1%. The thermal resistance R_{f1D} under NC and FC shown below were found in the previous experiments:

Air cooling	**Thermal resistance of FHS#1 (R_{f1D})**
NC	-0.0122 T_h + 5.06
FC	-0.0022 T_h + 1.02

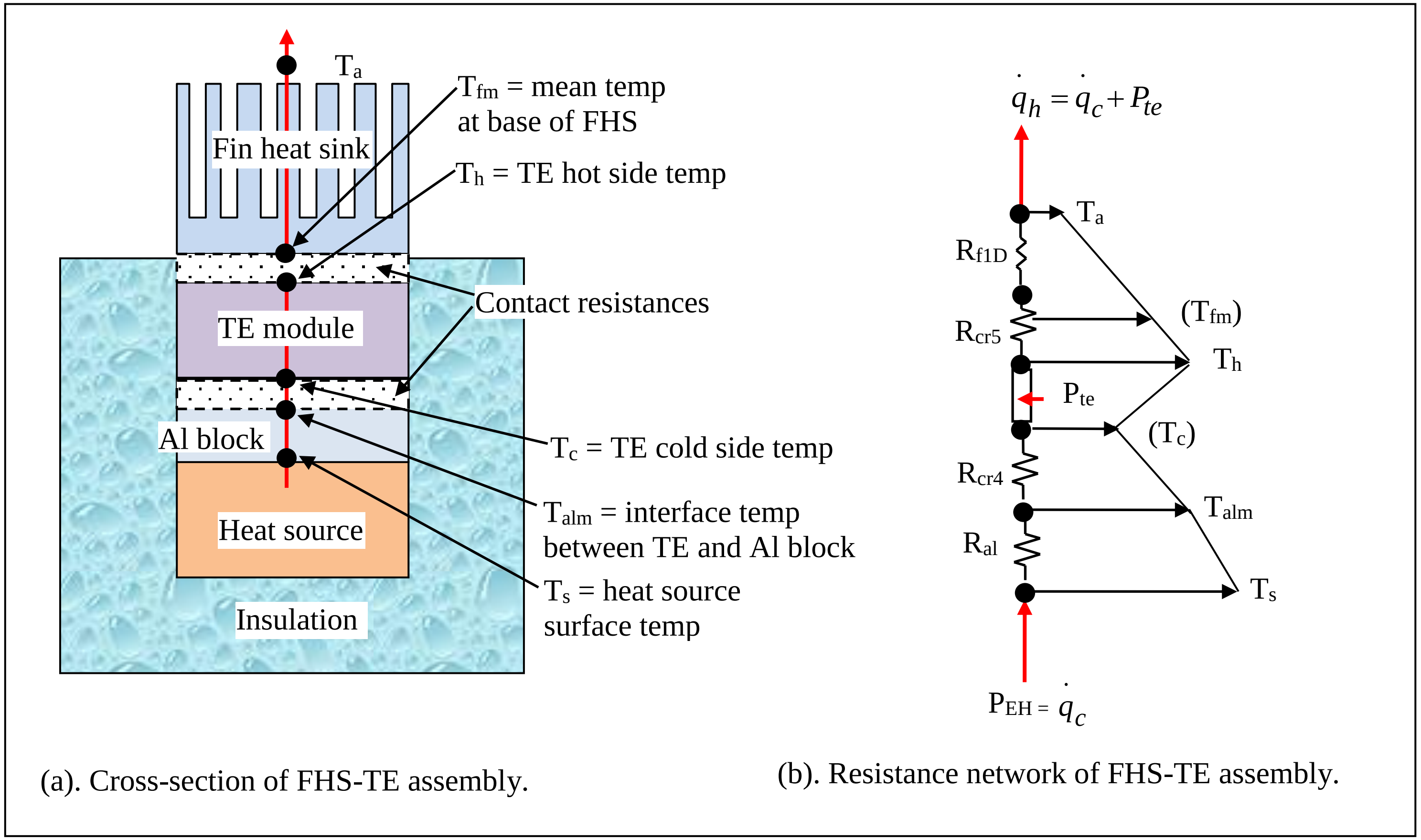

Figure 5.1 Theoretical model and thermal resistance network of FHS-TE assembly.

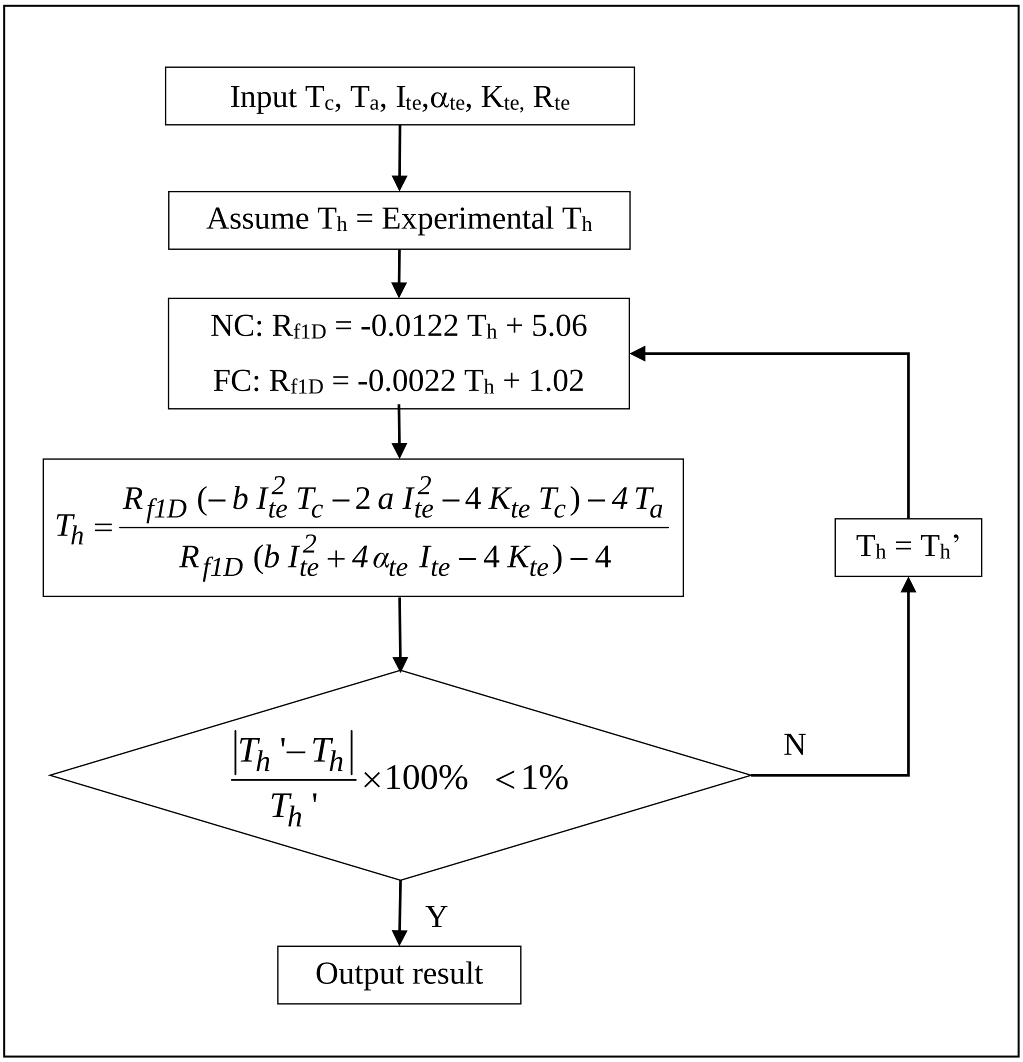

Figure 5.2 Flow chart for prediction of TE hot side (T_h) temperature.

5.3 Experimental investigation

5.3.1 Experimental apparatus

The thermal performance of FHS with TE assembly (FHS-TE) under natural convection (NC) and force convection (FC) air cooling was determined. The experimental setup is shown in Figure 5.3. The assembly consists of an electric heating element, aluminium block, TE module and FHS#1. The TE module used was HT8,12,F2,4040 manufactured by Laird Technologies. It measured 40 mm × 40 mm. with 4 mm thick. The electric heating element, Al block and FHS#1 described in the previous section were used. Heat flow was considered as one-dimensional. Heating power input was provided with an ac supply. An ac voltmeter and an ammeter were connected to measure the voltage (V_{EH}) and current (I_{EH}) supplied to the heating element. Thermal insulation was provided at the bottom and sides of the assembly up to and including the TE module to minimize heat loss to the surroundings. Power input to the TE was supplied with a dc supply. A dc voltmeter and an ammeter were connected to measure the voltage (V_{te}) and current (I_{te}) supplied to the TE module. A circulating fan was employed to provide force air circulation in the FC case. Air speed was not measured. Type-T (copper constantan) thermocouples were employed for temperature measurement. Four thermocouples (T_{f1} – T_{f4}) were inserted into holes drilled in a row through the base of FHS#1 to measure the interface temperature between the base of the FHS#1 and the TE module. Hot side temperature (T_h) of the TE module was obtained from arithmetic mean of the four thermocouples. Two thermocouples were centrally located in 1.5 mm deep grooves machined on the top and bottom surfaces of the 5 mm thick aluminium block to measure the mean surface temperature of the top of the aluminium block (T_{alm}) and the heat source (T_s). Cold side TE temperature (T_c) was assumed equal to T_{alm}. The mean operating temperature (T_{mte}) of the TE module was calculated by taking the arithmetic mean of hot (T_h) and cold side (T_c) temperatures. Additional thermocouples were employed to measure the external surface temperature of the insulation (T_{ins}) to determine heat loss and ambient temperature (T_a) to determine heat dissipation to the ambient. Temperatures were logged every minute using a data-logger.

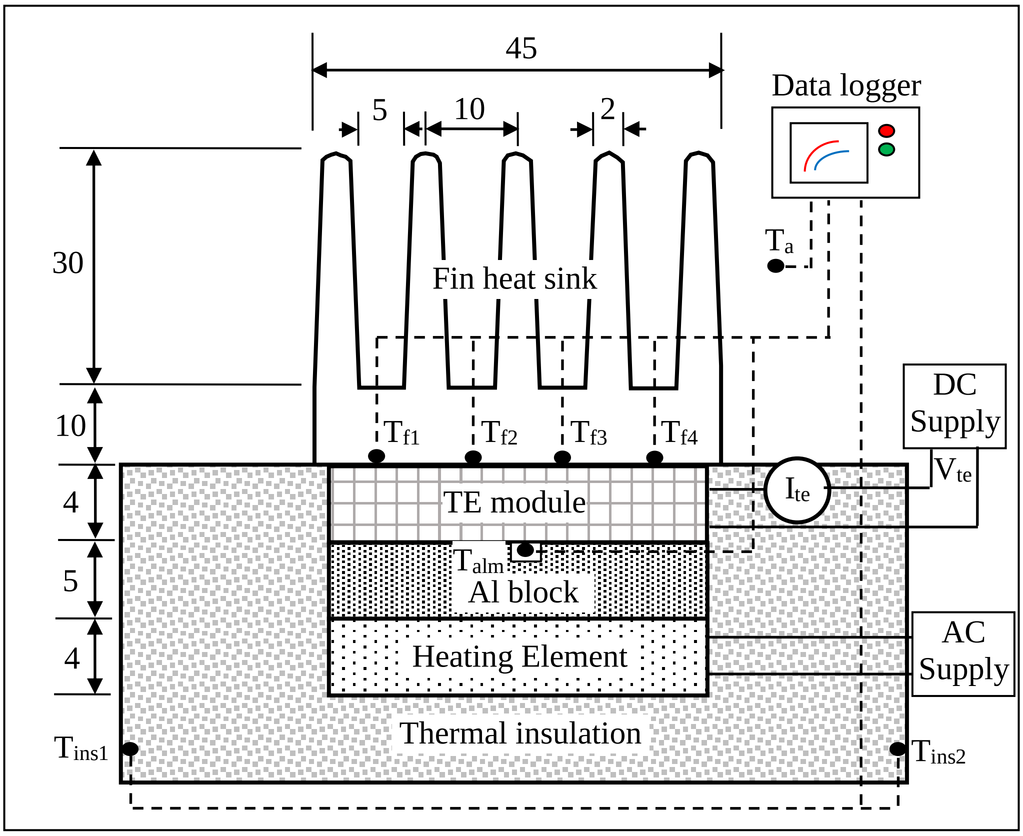

Figure 5.3 Experimental set up to determine thermal performance of FHS-TE assembly.

5.3.2 Experimental procedure

Experimental runs were performed at power inputs (P_{EH}) of 10 W and 20 W. Voltage supplied to the TE (V_{te}) varied from 1 – 6 V. Before the start of each experimental run, the voltages to the electric heating element and TE module were adjusted to produce the required power inputs. Power was then switched on. In the FC case, the fan was also switched on. Temperatures are recorded and each experimental run was carried on for at least 60 minutes at each setting in order to achieve steady state. The experimental results are tabulated in Table 5 as Runs D1 and D2 for NC and as Runs D3 and D4 for FC.

5.3.3 Experimental results

Figures 5.4 to 5.7 show the transient temperatures recorded for the FHS–TE assembly under NC and FC for all the experimental Runs D1 to D4. Comparisons of the hot side (T_h), cold side (T_c), heat source (T_s) and ambient (T_a) temperatures are shown in Figures 5.8 and 5.9. Comparisons of experimental (T_h) and predicted hot side ($T_{h,theory}$) temperatures are made in Figure 5.10. The coefficient of cooling performance (COP_c) and temperature difference.between hot and cold sides (ΔT_{te}) of the TE are shown in Figure 5.11. A comparison of FHS#1 with and without the TE modules is shown in Figure 5.12.

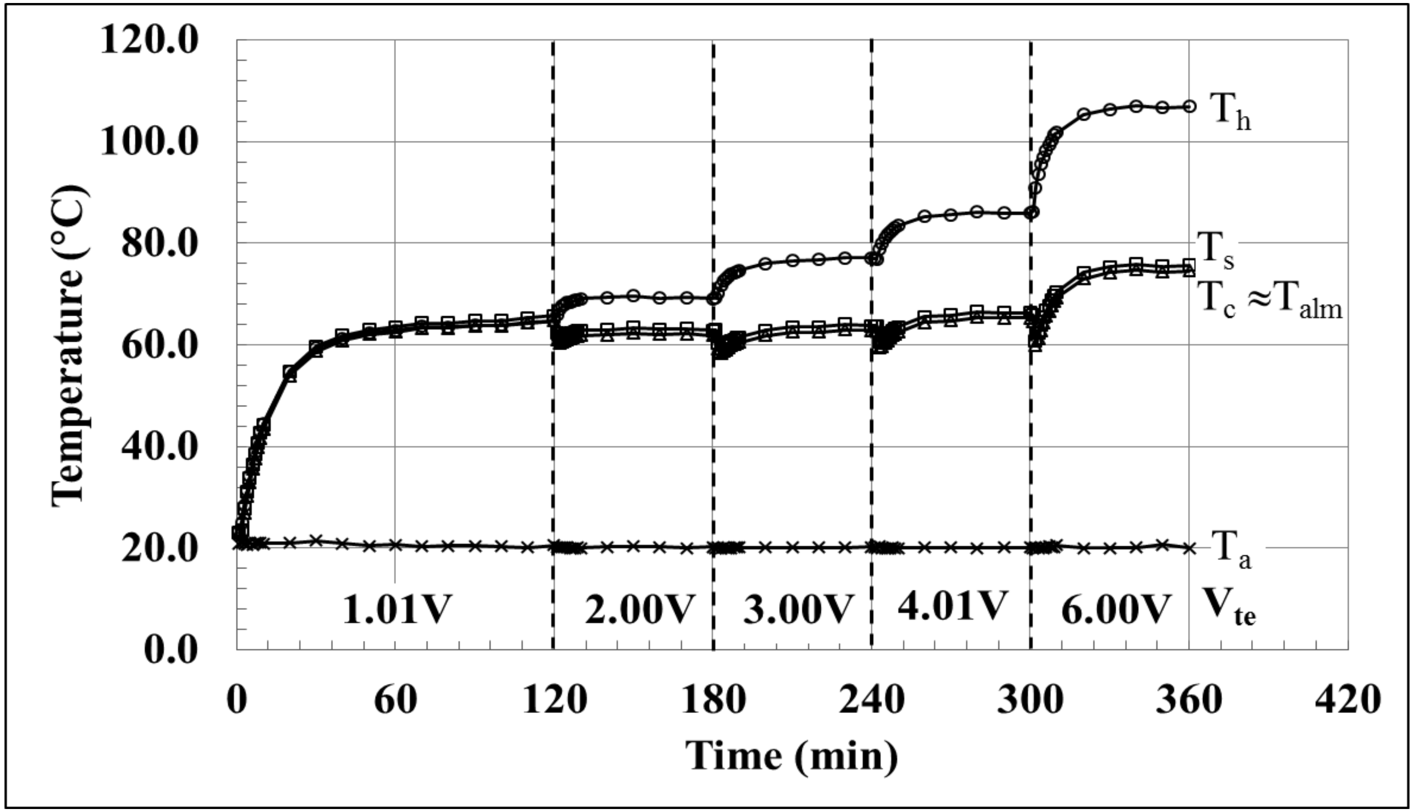

Figure 5.4 Transient temperatures for FHS-TE assembly (NC, P_{EH} = 10 W - Run D1).

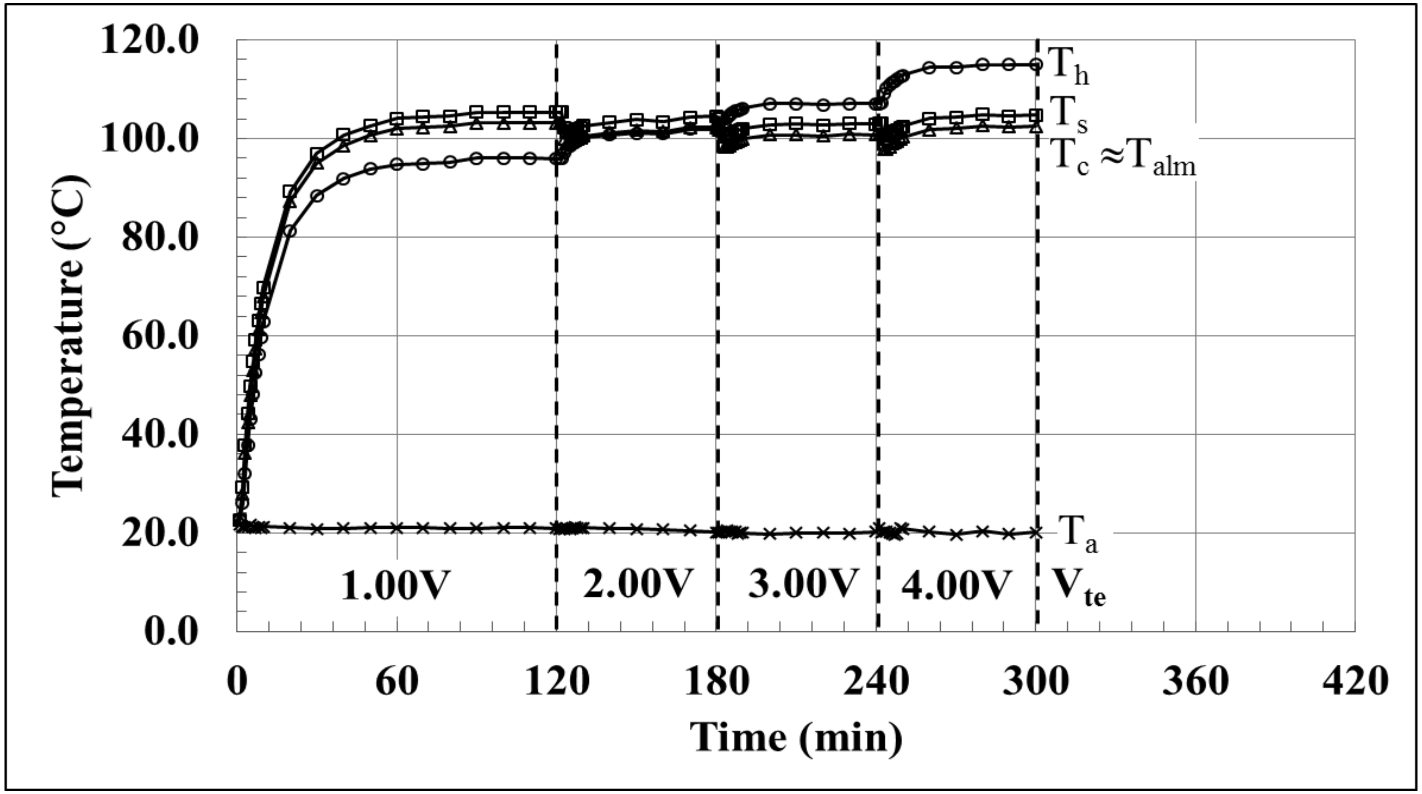

Figure 5.5 Transient temperatures for FHS-TE assembly (NC, P_{EH} = 20 W - Run D2).

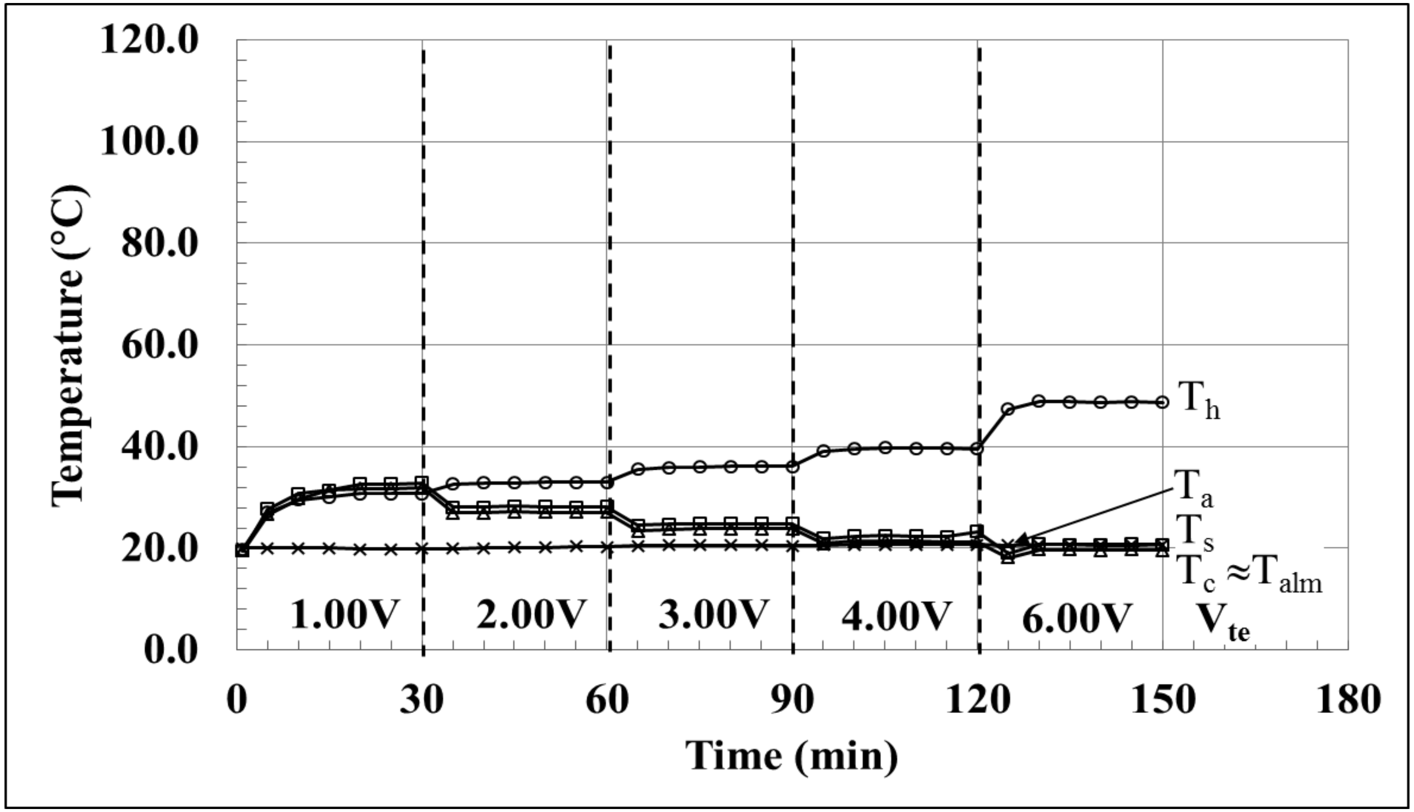

Figure 5.6 Transient temperatures for FHS-TE assembly (FC, P_{EH} = 10 W - Run D3).

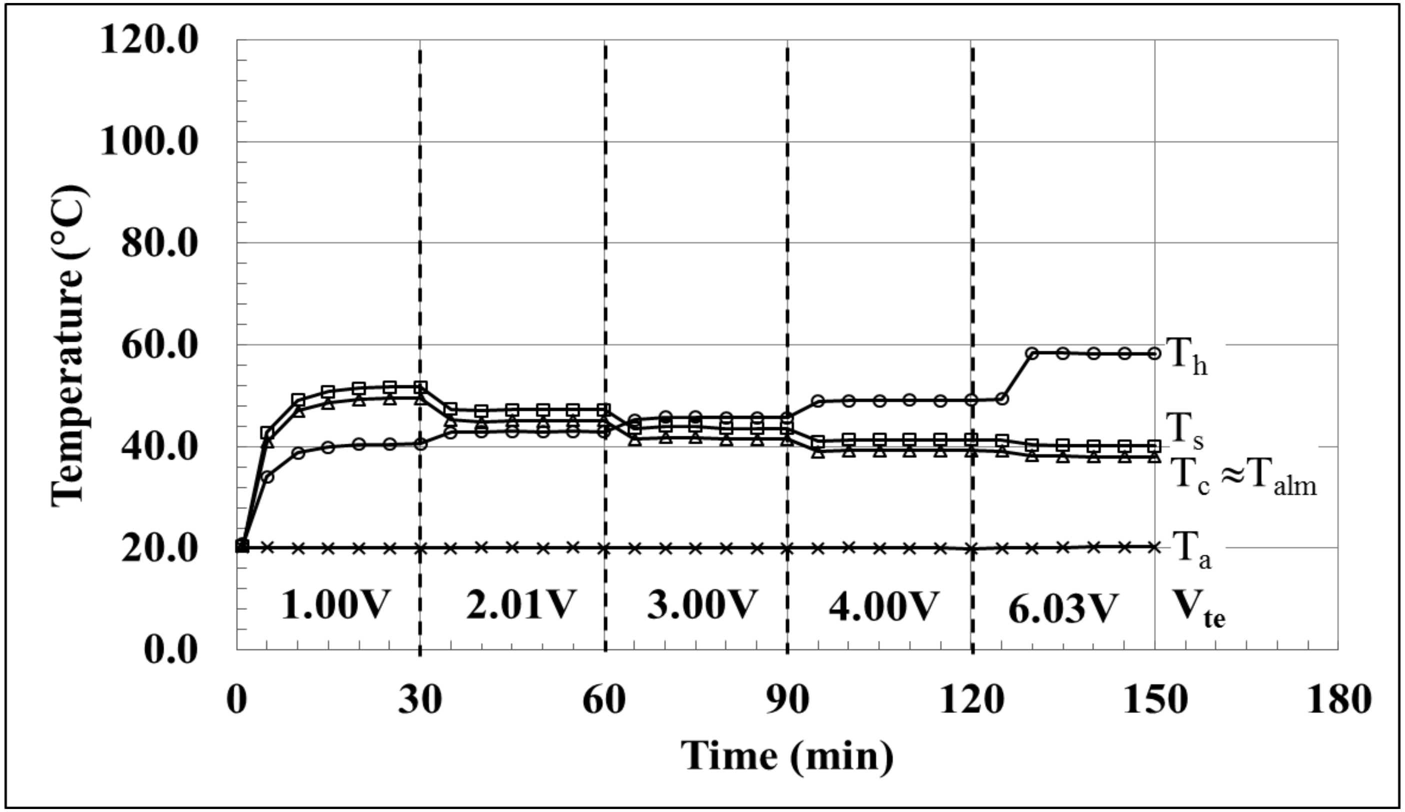

Figure 5.7 Transient temperatures for FHS-TE assembly (FC, P_{EH} = 20 W - Run D4).

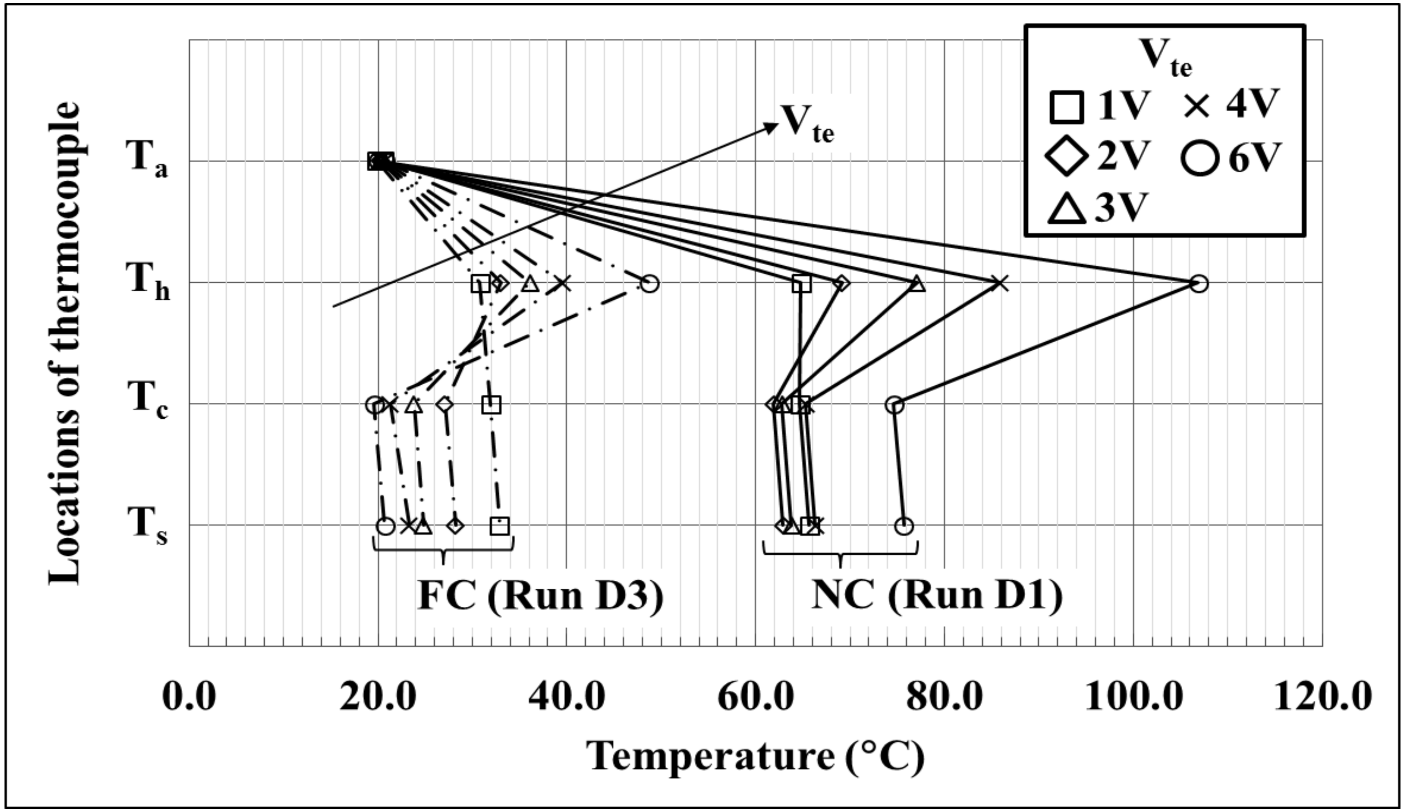

Figure 5.8 Comparison of interface temperatures for FHS-TE assembly under NC and FC (P_{EH} = 10 W - Runs D1 and D3).

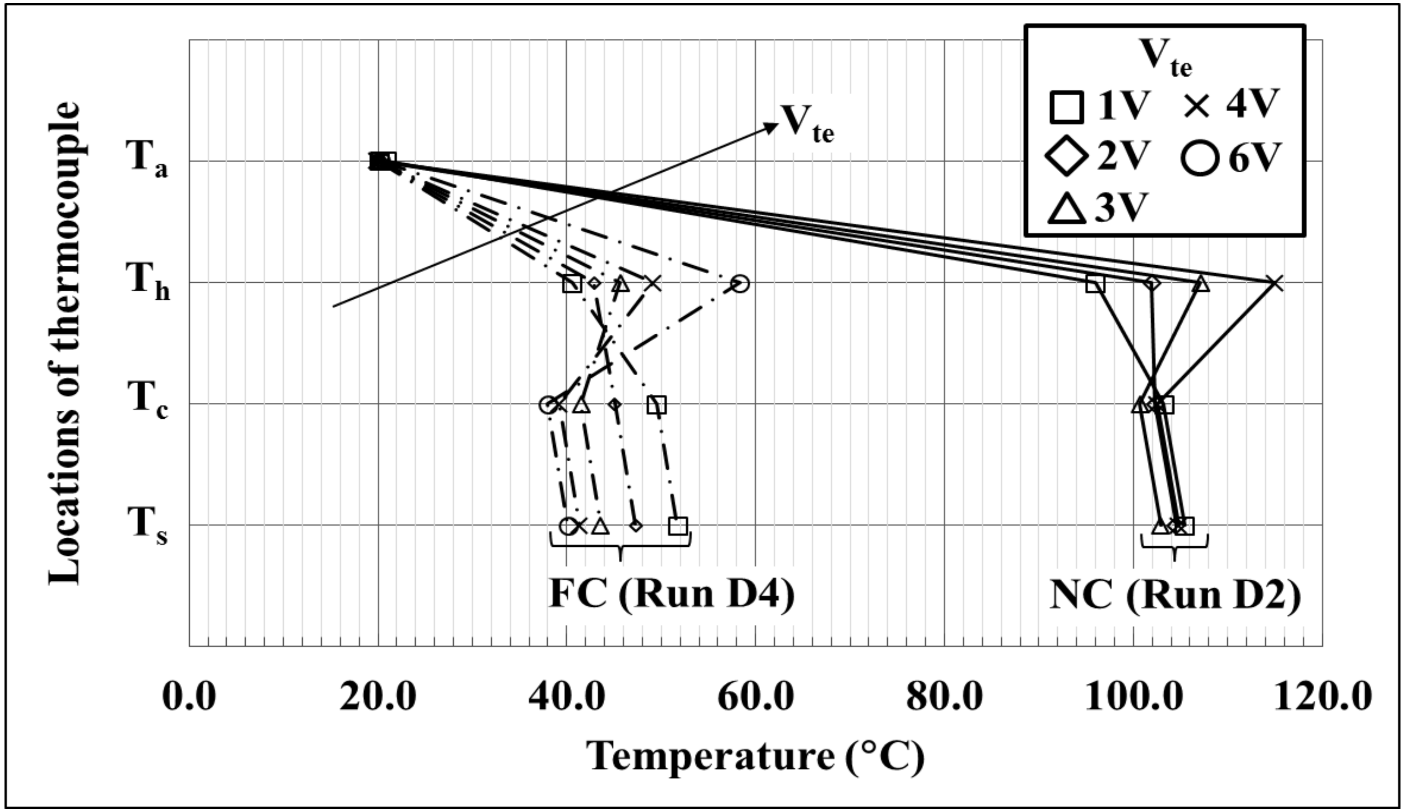

Figure 5.9 Comparison of interface temperatures for FHS-TE assembly under NC and FC (P_{EH} = 20 W - Runs D2 and D4).

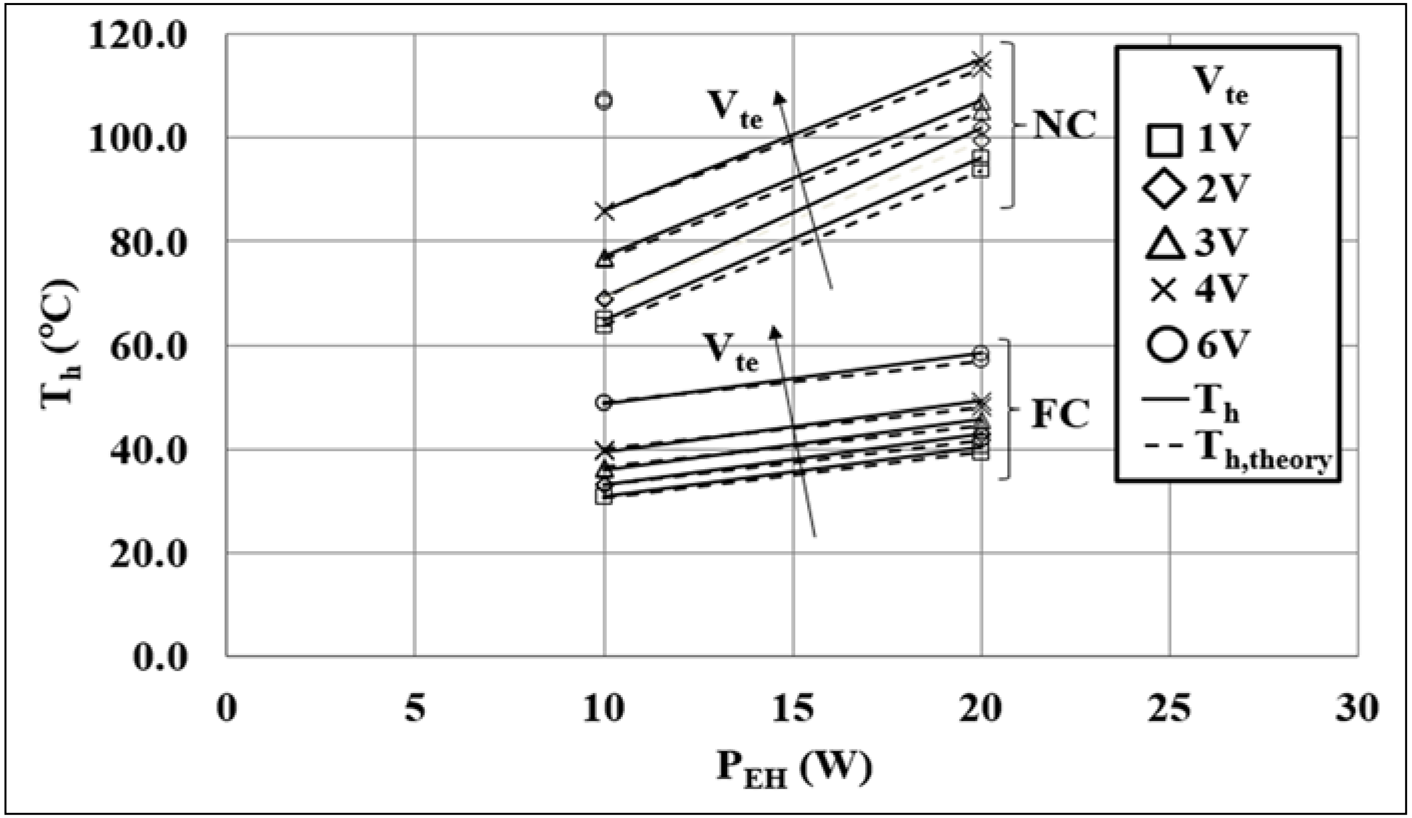

Figure 5.10 Comparison of experimental and predicted T_h for FHS-TE assembly (Runs D1-D4).

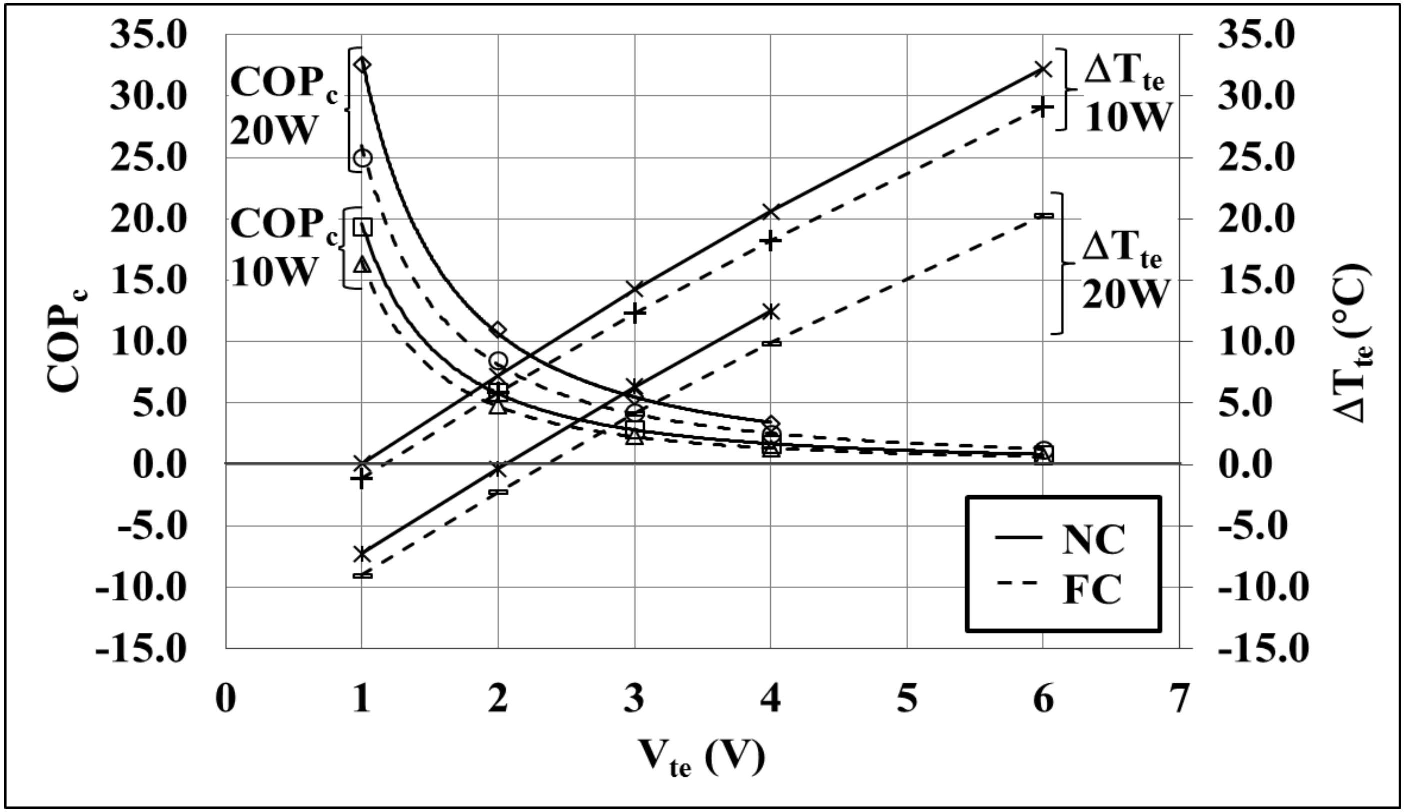

Figure 5.11 Coefficient of cooling performance (COP_c and temperature difference ΔT_{te}).

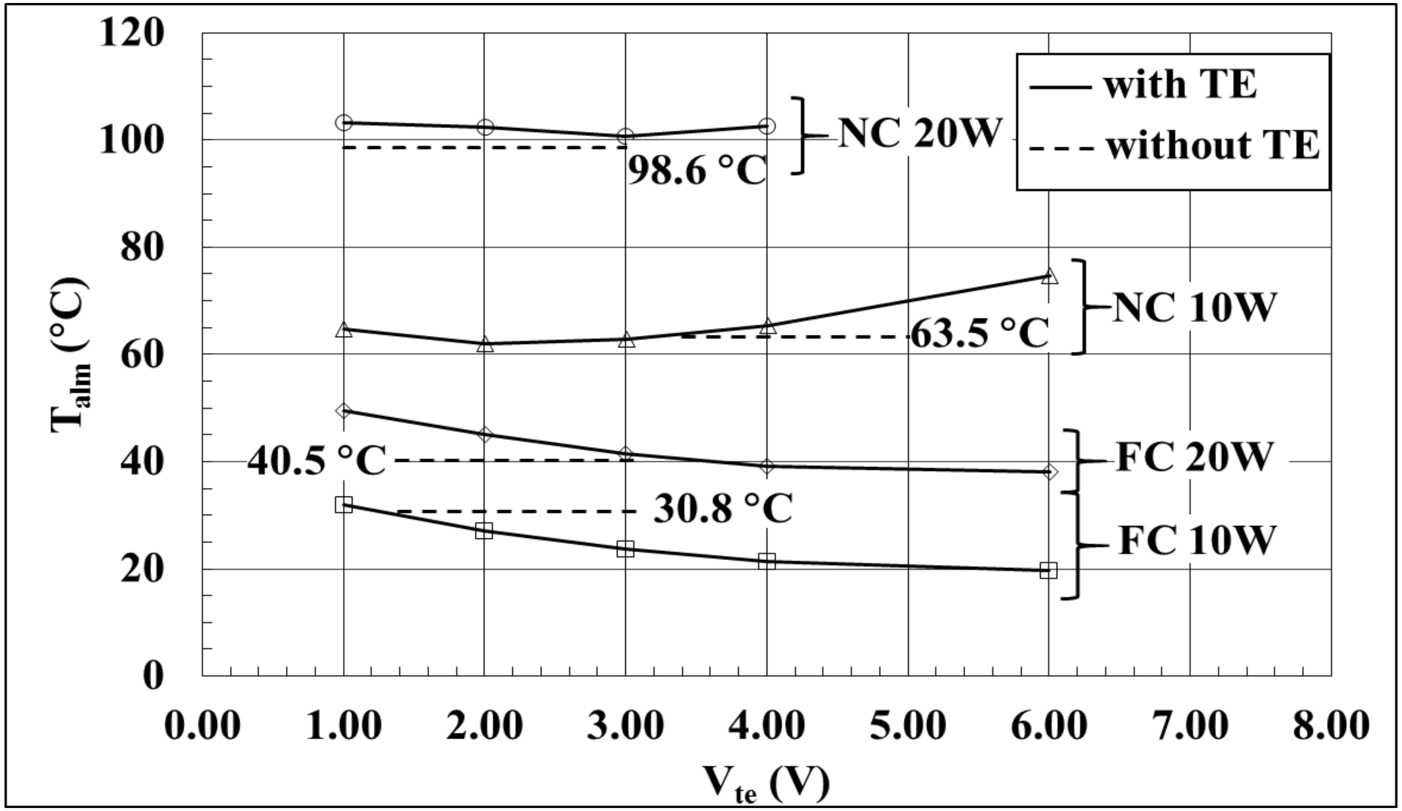

Figure 5.12 Comparison of surface temperature of aluminium block (T_{alm}) with and without TE.

5.4 Discussion of results

5.4.1 Heat source, TE hot and cold side temperatures

The transient temperatures in Figures 5.4 – 5.7 show that steady state can be said to be achieved after about 60 minutes of powering up the electrical heater. The following results can be seen:

- At a particular input power, all temperatures increase as power supplied to the TE increase as expected.
- Temperature across the aluminum block is about 1^{o}C as confirmed by steady state heat conduction calculations.
- FC results in lower temperatures than NC because of higher heat transfer coefficent.

The effect of power supply to the TE (P_{te}) are compared under NC (Run D1) and FC (Run D3) at 10 W electrical power input (P_{EH}) in Figure 5.8 and at 20 W in Figure 5.9 for Runs D2 and D4. The following results can be seen:

- All temperatures increase as heating power increase.
- FC results in lower temperatures than NC because of higher heat transfer rate.
- Hot side temperature (T_h) is generally higher than cold side (T_c).

- However, for the case of 10 W heat input, the hot side temperature becomes lower than the cold side at the low TE voltage (V_{te}) input of 1V or about TE power (P_{te}) of 0.5 W. This is because of insufficient TE power supply to operate the TE. At 20 W, the required TE voltage input is greater than 2 V. This indicates that greater TE power input is required to dissipate more heat from the heat source as expected. Hence the design of the FHS-TE asembly must be carefully calculated for the TE to operate efficiently.

A comparison of experimental and predicted TE hot side temperature (T_h) for FHS-TE assembly is shown in Figure 5.10. Hot side temperature increase with power input. It is also higher under NC. Predicted values are higher than experimental values by about 5 – 10%.

5.4.2 Coefficient of cooling performance

Experimental coefficient of cooling performance (COP_c) and temperature difference across the TE surface (ΔT_{te}) under NC and FC air cooling are compared in Figure 5.11 for both NC (Runs D1 – D4). The following results can be seen:

- Temperature difference is higher under NC. Hot side temperature is lower than cold side at the low TE voltage (V_{te}) input of 1 V at 10 W and about 2 V at the higher power input of 20 W indicating insufficient TE power supply to generate sufficient temperature differential to enable the TE to function.

5.4.3 Comparison of performance of FHS with and without the TE

Figure 5.12 compares the experimental results obtained for the temperature of the surface of the aluminium block (T_{alm}) with and without the TE module under NC and FC conditions and under 10 and 20 W power inputs. The values shown in dashed lines represents the temperature (T_{alm}) obtained previously without the TE while the solid lines show the results obtained with the TE. The results show that under NC, the surface temperature of the aluminium block is lower without the use of the TE at both power inputs. However, under FC at 10 W, T_{alm} was lower with the FHS-TE assembly when applied voltage to the TE (V_{te}) was greater than 1 V. At 20 W power input, the FHS-TE assembly performed better when the TE was powered up above 3 V. This shows that the TE have to be properly and adequately matched with the FHS at the design stage.

5.5 Chapter conclusions

The thermal performances of the FHS–TE assembly under FC and NC air cooling were evaluated. Temperatures obtained with FC air cooling were lower than NC air cooling. A method to predict the hot side temperature of the TE was presented. Comparisons between theoretical and experimental results were made. The results showed that the experimental values were about 5–10% higher than theoretical. A proper FHS design to match TE heat dissipation was shown to be critical for effective operation.

CHAPTER 6

SUGGESTIONS FOR FUTURE STUDIES

The following are recommended for future studies:

FHS

1. Ambient temperature and air flow rate need to be varied and controlled.
2. Air flow rate affects the heat transfer coefficient and needs to be measured.
3. Determine the heat transfer coefficient with heat spreading present.
4. Investigate other types of FHSs such as the pin, radial and flared types.

FHS-VC assembly

1. Use a smaller heating element and higher power inputs to simulate greater thermal heat spreading effects.
2. Investigate the VC with hollow fins and fully integrated directly onto it to eliminate thermal contact and casing thermal resistances.

FHS-TE assembly

1. Use a lower thermal resistance FHS to further examine the performance of the TE module.
2. Investigate the performance of the TE with water-cooled FHS.
3. Investigate the performance of the TE with a pulse width modulation (PWM) controller.

CHAPTER 7

OVERALL CONCLUSIONS

The performances of fin heat sinks, vapour chamber and thermoelectric cooling of hot surfaces such as that present in semiconductors were evaluated. Heat transfer coefficient for force convection was higher than for natural convection. Thermal heat spreading resulting in 2-dimensional heat flow through the fin heat sink reduces the heat transfer coefficient. Further studies are recommended to determine actual values.

The temperature distribution at the top surface of the vapour chamber was uniform while the bottom surface was not, showing the effectiveness of the vapour chamber to eliminate thermal heat spreading. The total thermal resistance of the vapour chamber was found to be equal to 1.50 – 2.05 K/W. The results of the present FHS-VC assembly show that the addition of the VC did not improve the cooling performance because of the thermal contact resistances between the surfaces of contact with the fin heat sink and the heating element.

A program to predict the hot side temperature of the thermoelectric module was presented. Comparisons between theoretical and experimental results showed that experimental values were about 5 – 10% higher. Proper matching between thermoelectric heat dissipation and heat sink design was shown to be very important and critical for it to operate well.

Overall, the study could be said to be successfully completed.

REFERENCES

Ahmed A.A. Attia, B. T. E.-A., 2012. Experimental investigation of vapor chamber with different working fluids at different charge ratios. *Ain Shams Engineering Journal*, 3(3), pp. 289-297.

Bergman, T. L., Incropera, F. P., Dewitt, D. P. & Lavine, A. S., 2011. *Fundamentals of heat and mass transfer.* 7th edition ed. Wiley.

Bierschenk, J. & Johnson, D., 2004. *Extending the limits of air cooling with thermoelectrically enhanced heat sinks*, Inter Society Conference on Thermal Phenomena.

Boukhanouf, R., Haddad, A., North, M. & Buffone, C., 2006. Experimental investigation of a flat plate heat pipe performance using IR thermal imaging camera. *Applied Thermal Engineering*, 26(17-18), pp. 2148-2156.

Chang, Y.-W., Chang, C.-C., Ke, M.-T. & Chen, S.-L., 2009. Thermoelectric air-cooling module for electronic devices. *Applied Thermal Engineering*, 29(13), pp. 2731-2737.

Chein, R. & Chen, Y., 2005. Performances of thermoelectric cooler integrated with microchannel heat sinks. *International Journal of Refrigeration*, 28(6), pp. 828–839.

Chein, R. & Huang, G., 2004. Thermoelectric cooler application in electronic cooling. *Applied Thermal Engineering,* 24(14-15), pp. 2207-2217.

Chen, H.-T., Lai, S.-T. & Haung, L.-Y., 2013. Investigation of heat transfer characteristics in plate-fin heat sink. *Applied Thermal Engineering,* Volume 50, pp. 352-360.

Chen, Y.-S.et al., 2009. Numerical simulation of a heat sink embedded with a vapor chamber and calculation of effective thermal conductivity of a vapor chamber. *Applied Thermal Engineering,* 29(17-18), pp. 2655–2664.

Chen, Y.-S., Chien, K.-H. & Wang, C.-C., 2006. A simplified transient three-dimensional model for estimating the thermal performance of the vapor chambers. *Applied Thermal Engineering,* Volume 26, pp. 2087–2094.

Chen, Y.-T., Kang, S.-W., Hung, Y.-H. & Huang, C.-H., 2013. Feasibility study of an aluminum vapor chamber with radial grooved and sintered powders wick structures. *Applied Thermal Engineering,* 51(1-2), pp. 864-870.

Connors, M. J., 2009. *The Use of vapor chambers and heat pipes for cooling military embedded electronic devices.* Boston, MA, IEEE Military Communications Conference.

Ellison, G. N., 2003. Maximum Thermal Spreading Resistance for Rectangular Sources and Plates With Nonunity Aspect Ratios. *IEEE Transactions on Components and Packaging Technologies*, 26(2), pp. 439 - 454.

Hasan, M. H. & Toh, K. C., 2007. *Optimization of a Thermoelectric Cooler-Heat Sink Combination for Active Processor Cooling.* Singapore, Electronics Packaging Technology Conference, 2007. EPTC 2007. 9th.

Huang, C.-K., Su, C.-Y. & Lee, K.-Y., 2012. The Effects of Vapor Space Height on the Vapor Chamber Performance. *Experimental Heat Transfer: A Journal of Thermal Energy Generation, Transport, Storage, and Conversion,* 25(1), pp. 1-11.

Kaushik, S., Manikandan, S. & Hans, R., 2015. Energy and exergy analysis of thermoelectric heat pump system. *International Journal of Heat and Mass Transfer,* Volume 86, pp. 843–852.

Kim, D.-K., 2012. Thermal optimization of plate-fin heat sinks with fins of variable thickness under natural convection. *International Journal of Heat and Mass Transfer,* Volume 55, pp. 752-761.

Kim, H., Kim, K. J. & Lee, Y., 2012. *Thermal Performance of Smart Heat Sinks for Cooling High Power LED Modules,* 13th IEEE ITHERM Conference.

Li, B., Jeon, S. & Byon, C., 2016. Investigation of natural convection heat transfer around a radial heat sink with a perforated ring. *International Journal of Heat and Mass Transfer,* Volume 97, pp. 705-711.

Lim, C. Y. J., 2014. *Comparative performance tests on thermosyphons and application as heat pipe heat exchanger cooler operating between 30 - 100 C,* Universiti Tunku Abdul Rahman.

Lin, W.-K.et al., 2011. *The Development of the Performance Measuring System for the Phase Change Heat Transport Device-- Heat pipe, Vapor Chamber and Defrost Plate.* Taipei, 6th International Microsystems, Packaging, Assembly and Circuits Technology Conference.

Luo, X. et al., 2010. *Low Thermal Resistance LED Light Source with Vapor Chamber Coupled Fin Heat Sink.* Las Vegas, NV, USA, Electronic Components and Technology Conference.

Peng, H., Li, J. & Ling, X., 2013. Study on heat transfer performance of an aluminum flat plate heat pipe with fins in vapor chamber. *Energy Conversion and Management,* Volume 74, pp. 44–50.

Qian, B. & Ren, F., 2016. Cooling performance of transverse thermoelectric devices. *International Journal of Heat and Mass Transfer,* Volume 95, pp. 787–794.

Rahmani, Y., Ganji, D. D. & Bandpy, M. G., 2016. Analytical study of thermal spreading resistance in curved-edge heat spreader. *Applied Thermal Engineering,* Volume 104, pp. 527 - 533.

Rao, R. & Waghmare, G., 2015. Multi-objective design optimization of a plate-fin heat sink using a teaching-learning-based optimization algorithm. *Applied Thermal Engineering,* Volume 76, pp. 521-529.

Razavi, M., Muzychka, Y. & Kocabiyik, S., 2016. Review of Advances in Thermal Spreading Resistance Problems. *Journal of thermophysics and heat transfer,* 0(0).

Shaeri, M. & Yaghoubi, M., 2009. Thermal enhancement from heat sinks by using perforated fins. *Energy Conversion and Management,* Volume 50, pp. 1264-1270.

Taylor, R. A. & Solbrekken, G. L., 2006. *Optimization of Thermoelectric Cooling for Microelectronics.* San Diego, CA, Thermal and Thermomechanical Proceedings 10th Intersociety Conference on Phenomena in Electronics Systems.

Tsai, M.-C., Kang, S.-W. & Paiva, K. V., 2013. Experimental studies of thermal resistance in a vapor chamber heat spreader. *Applied Thermal Engineering,* 56(1-2), pp. 38 - 44.

Wang, J.-C., 2011. Thermal investigations on LED vapor chamber-based plates. *International Communications in Heat and Mass Transfer,* 38(9), pp. 1206–1212.

Wang, J. et al., 2015. Experimental study on the thermal management of high-power LED headlight cooling device integrated with thermoelectric cooler package. *Energy Conversion and Management,* Volume 101, pp. 532-540.

Wang, N., Wang, C.-h., Lei, J.-x. & Zhu, D.-s., 2009. *Numerical Study on Thermal Management of LED Packaging by Using Thermoelectric Cooling.* s.l., International Conference on Electronic Packaging Technology & High Density Packaging.

Wang, X., Yu, J. & Ma, M., 2013. Optimization of heat sink configuration for thermoelectric cooling system based on entropy generation analysis. *International Journal of Heat and Mass Transfer,* Volume 63, pp. 361-365.

Yang, K.-S.et al., 2014. Thermal spreading resistance characteristics of a high power light emitting diode module. *Applied Thermal Engineering,* Volume 70, pp. 361-368.

Zebarjad, M., 2015. Electronic cooling using thermoelectric devices. *Applied Physics Letters,* Volume 106.

Zhang, H., 2010. A general approach in evaluating and optimizing thermoelectric coolers. *International Journal of Refrigeration*, 33(6), pp. 1187-1196.

Zhang, M., Liu, Z. & Ma, G., 2009. The experimental and numerical investigation of a grooved vapor chamber. *Applied Thermal Engineering*, 29(2-3), pp. 422-430.

Zhong, D., Qin, H., Wang, C. & Xiao, Z., 2010. *Thermal Performance of Heatsink and Thermoelectric Cooler Packaging Designs in LED.* Xi'an, 11th International Conference on Electronic Packaging Technology & High Density Packaging.

APPENDICES

APPENDIX A: Tables

Table 1 Experimental results for FHS#1 under natural convection (NC) and force convection (FC) (ε = 0.79).

Heat sink dimensions (mm x mm)	NC /FC	Run #	P_{EH} (W)	P_{loss} (W)	T_a (°C)	T_{insm} (°C)	T_{alm} (°C)	ΣR_{f2D} (K/W) Eqn. 2.7	$R_{f1D} = \Sigma R_{f2D} - R_{cr1}$ (K/W) (R_{cr1}= 0.05 K/W) Eqn. 2.6	h_a (W/m^{2}K) Eqns. 2.9-2.19
45 x 45	FC	A1	10.0	0.01	21.0	21.9	31.5±0.1	1.05	1.00	69.0
			20.0	0.02	21.1	21.8	41.2±0.1	1.00	0.95	73.0
			30.0	0.03	20.9	21.8	50.5±0.1	0.98	0.93	74.1
		A2	9.9	0.01	20.7	21.4	30.4±0.1	0.98	0.93	74.1
			20.0	0.03	20.7	21.8	40.2±0.1	0.97	0.92	74.9
			30.0	0.04	21.0	22.0	50.1±0.1	0.97	0.92	74.9
		A3	9.9	0.01	20.6	21.8	30.5±0.1	1.00	0.95	73.0
			20.0	0.03	20.9	21.8	40.2±0.1	0.95	0.90	75.8
			30.0	0.04	21.0	22.1	49.7±0.1	0.95	0.90	75.8
							Average	0.98	0.93	73.8
45 x 45	NC	A4	10.0	0.05	20.2	22.8	63.8±0.0	4.36	4.31	15.2
			15.0	0.07	20.3	23.5	82.1±0.0	4.11	4.06	16.1
			20.1	0.09	20.3	24.0	98.9±0.1	3.92	3.87	16.9
		A5	9.9	0.05	20.3	23.0	63.1±0.1	4.32	4.27	15.3
			15.2	0.07	20.4	23.3	82.7±0.1	4.09	4.04	16.2
			20.0	0.09	20.2	23.7	98.4±0.1	3.91	3.86	17.0
		A6	9.9	0.05	20.7	23.1	63.6±0.1	4.33	4.28	15.3
			15.1	0.07	19.7	23.1	81.6±0.1	4.11	4.06	16.1
			20.1	0.09	20.1	23.6	98.5±0.0	3.90	3.85	17.0
							Average	4.12	4.07	16.1

Table 2 Experimental results for FHS#2 under NC (ε = 0.053).

Heat sink dimensions (mm x mm)	Run #	P_{EH} (W)	P_{loss} (W)	T_a (°C)	T_{insm} (°C)	$T_{fmax} \approx T_{alm}$ (°C)	T_{fm} (°C)	$R_{cr1} + R_{srf}$ (K/W) Eqn. 2.4	R_{f1D} (K/W) Eqn. 2.5	ΣR_{f2D} (K/W) Eqn. 2.6	h_a (W/m²K) Eqn. 2.20
135 x 123	B1	10.1	0.02	20.8	21.7	37.8±0.3	36.9±1.0	0.09	1.59	1.68	14.0
		29.3	0.05	20.7	22.1	62.5±0.6	60.1±2.6	0.08	1.34	1.42	15.1
		50.4	0.08	20.9	22.7	84.3±1.2	80.1±4.3	0.08	1.17	1.25	16.0
	B2	10.1	0.02	20.0	20.9	36.6±0.2	35.7±1.0	0.09	1.55	1.64	13.9
		29.9	0.05	20.4	21.7	62.0±0.7	59.5±2.6	0.08	1.31	1.39	15.1
		50.1	0.08	21.3	22.2	85.3±1.2	80.9±4.6	0.09	1.19	1.28	16.1
	B3	10.0	0.02	19.8	20.3	35.1±0.3	34.3±1.0	0.08	1.45	1.53	13.8
		29.8	0.05	20.4	21.1	61.2±0.6	58.7±2.6	0.08	1.29	1.37	15.0
		50.1	0.08	20.4	21.5	84.1±1.2	79.8±4.6	0.09	1.19	1.28	16.0
							Average	0.08	1.34	1.43	14.9

Table 3 Comparison of experimental and simulation results with different values of h_a.

Run #	P_{EH} (W)	Experimental			h_a from (2.20).			Modified h_a		
		h_a (W/ m^2 K) Eqn. 2.20	$T_{fmax} \approx T_{alm}$ (°C)	T_{fm} (°C)	h_a (W/ m^2 K) Eqn. 2.20.	$T_{fmax,CFD}$ (°C)	$T_{fm,CFD}$ (ºC)	h_a (W/ m^2 K) (modified)	$T_{fmax,CFD}$ (°C)	$T_{fm,CFD}$ (ºC)
B1	10.1	14.0	37.8±0.3	36.9±1.0	14.0	27.6	26.7	5.3	37.2	36.4
	29.3	15.1	62.5±0.6	60.1±2.6	15.1	39.2	36.7	6.3	61.2	58.6
	50.4	16.0	84.3±1.2	80.1±4.3	16.0	51.2	46.8	7.3	81.6	77.2
B2	10.1	13.9	36.6±0.2	35.7±1.0	13.9	26.8	26.0	5.4	36.1	35.2
	29.9	15.1	62.0±0.7	59.5±2.6	15.1	39.3	36.7	6.4	61.1	58.5
	50.1	16.1	85.3±1.2	80.9±4.6	16.1	51.3	46.9	7.1	83.2	78.9
B3	10.0	13.8	35.1±0.3	34.3±1.0	13.8	26.6	25.8	5.8	34.8	33.9
	29.8	15.0	61.2±0.6	58.7±2.6	15.0	39.3	36.7	6.5	60.4	57.8
	50.1	16.0	84.1±1.2	79.8±4.6	16.0	50.5	46.2	7.1	82.3	78.0

Table 4 Experimental results for FHS-VC assembly.

Heat sink dimensions (mm x mm)	NC/ FC	Run #	P_{EH} (W)	P_{loss} (W)	T_a (ºC)	T_{insm} (°C)	$T_{vcmax} \approx T_{alm}$ (ºC)	T_{vcbot} (ºC)	T_{vctop} (ºC)	$R_{f1D}+R_{cr3}$ (K/W) Eqn. 2.5	R_{vc} (K/W) Eqn. 4.4	$R_{cr2}+R_{srvc}$ (K/W) Eqn. 4.1-4.3	ΣR_{fvc} (K/W) Eqn. 4.6
123	NC	C1	10.0	0.02	20.6	22.0	41.1±0.3	37.9±2.1	37.8±0.4	1.72	0.01	0.32	2.05
			29.9	0.06	20.5	22.5	69.2±0.7	60.7±5.5	60.1±0.6	1.32	0.02	0.28	1.63
			49.9	0.09	21.0	23.3	95.7±0.9	81.8±9.3	79.6±0.8	1.17	0.04	0.28	1.50
		C2	10.0	0.02	19.8	20.7	38.6±0.3	35.6±2.1	35.5±0.4	1.57	0.01	0.30	1.88
			29.8	0.06	20.3	22.1	68.2±0.7	59.6±5.5	59.1±0.6	1.30	0.02	0.29	1.61
			50.2	0.09	20.8	23.4	97.4±1.0	82.0±9.8	79.8±1.0	1.18	0.04	0.31	1.53
		C3	10.1	0.02	20.0	21.4	40.7±0.3	37.5±2.2	37.4±0.5	1.72	0.01	0.32	2.05
			29.8	0.06	20.3	22.3	68.9±0.6	60.2±5.5	59.6±0.6	1.32	0.02	0.29	1.63
			50.1	0.09	20.4	23.0	96.4±0.9	81.6±9.4	79.5±0.9	1.18	0.04	0.30	1.52

Table 5 Experimental results for FHS-TE assembly under NC and FC.

NC/FC	Run #	P_{EH} (W)	P_{loss} (W)	V_{te} (V)	I_{te} (A)	P_{te} (W)	T_a (°C)	T_{ins} (°C)	T_s (°C)	$T_c \approx T_{alm}$ (°C)	T_h (°C)	ΔT_{te} (°C) Eqn. 5.3	T_{mte} (°C) Eqn. 5.10	COP_c Eqn. 5.8	$T_{h,theory}$ (°C) Eqn. 5.11
NC	D1	10.1	0.05	1.01	0.52	0.52	20.6	23.6	65.7	64.7	64.8	0.1	64.8	19.34	63.8
		10.0	0.05	2.00	0.85	1.69	20.3	23.6	62.9	61.9	69.2	7.2	65.5	5.89	68.8
		10.0	0.05	3.00	1.16	3.50	20.3	23.5	63.8	62.8	77.1	14.3	69.9	2.86	76.6
		10.0	0.05	4.01	1.47	5.88	20.2	23.6	66.3	65.3	85.9	20.6	75.6	1.70	85.9
		10.0	0.06	6.00	2.02	12.13	20.0	23.9	75.7	74.6	106.9	32.3	90.7	0.82	107.5
	D2	19.9	0.09	1.00	0.61	0.61	20.9	25.8	105.4	103.2	96.0	-7.2	99.6	32.57	93.6
		19.8	0.09	2.00	0.90	1.81	20.1	25.1	104.5	102.3	102.0	-0.4	102.1	10.97	99.3
		19.8	0.09	3.00	1.19	3.57	20.2	25.3	102.9	100.7	107.1	6.4	103.9	5.55	105.1
		19.8	0.09	4.00	1.47	5.88	20.1	25.0	104.8	102.5	115.0	12.5	108.8	3.37	113.3
		-	-	6.00	-	-	-	-	-	-	-	-	-	-	-
FC	D3	10.3	0.01	1.00	0.63	0.63	19.9	20.9	32.9	31.9	30.8	-1.1	31.4	16.36	30.6
		10.0	0.01	2.00	1.04	2.08	20.3	21.3	28.2	27.1	33.0	5.9	30.0	4.80	33.2
		9.9	0.00	3.00	1.45	4.36	20.5	21.5	24.8	23.8	36.1	12.3	30.0	2.28	36.5
		10.0	0.00	4.00	1.84	7.37	20.7	21.5	23.3	21.3	39.6	18.3	30.4	1.36	40.0
		10.0	0.00	6.00	2.62	15.7	20.7	21.5	20.7	19.6	48.8	29.2	34.2	0.63	48.9
	D4	20.1	0.04	1.00	0.80	0.80	20.1	22.0	51.7	49.5	40.5	-9.0	45.0	25.00	39.3
		20.3	0.03	2.01	1.19	2.38	20.1	22.1	47.3	45.1	42.9	-2.2	44.0	8.50	41.7
		20.0	0.03	3.00	1.57	4.72	20.1	22.1	43.6	41.5	45.7	4.2	43.6	4.25	44.5
		20.0	0.02	4.00	1.96	7.84	19.9	21.9	41.3	39.2	49.1	9.9	44.2	2.55	48.0
		20.3	0.02	6.00	2.70	16.2	20.3	21.9	40.1	38.0	58.3	20.3	48.2	1.25	57.0